ABSTRACT

Title of Dissertation: MELANOPSIN AND PACAP IN INTRINSICALLY PHOTOSENSITIVE RETINAL GANGLION CELLS REGULATE THE DEVELOPMENT OF RETINOFUGAL PROJECTIONS IN MICE

César Javier Hernández
Doctor of Philosophy, 2025

Dissertation Directed by: Associate Professor Colenso M. Speer
Department of Biology

In the retina, a small subset of retinal ganglion cells are intrinsically photosensitive (ipRGCs) and express the photopigment melanopsin and the neuropeptide pituitary adenylate cyclase-activating polypeptide (PACAP). These cells project to brain nuclei to mediate a variety of visual behaviors involved in both non-image and image-forming functions, such as circadian photoentrainment and conscious visual perception. ipRGCs have been implicated in a number of developmental processes such as cone photoreceptor development, patterning of retinal vasculature, and synapse formation and maturation. However, whether or not these molecules are involved in development of retinofugal projections to the suprachiasmatic nucleus (SCN) and refinement of eye-specific segregation in the dorsal lateral geniculate nucleus (dLGN) have not been extensively determined. To answer these questions, I used tract tracing with eye injections and mesoscale imaging to assess ipRGC projections to the SCN and dLGN of both juvenile melanopsin ($Opn4^{cre/cre}$) and

conditional ipRGC-specific PACAP ($Opn4^{Cre/+}$ / $Adcyap1^{fl/fl}$) knockout mice. I found that in melanopsin knockout mice, axonal projections to the SCN were altered, and eye-specific segregation in the dLGN was impaired. In PACAP knockout mice, axonal projections to the SCN are unaltered, but eye-specific segregation in the dLGN is impaired. These results suggest that melanopsin and PACAP play differential roles in the proper development of retinofugal projections in mice. In parallel, I applied volumetric super-resolution fluorescence imaging using Expansion Microscopy (ExM) to study synaptic connectivity of ipRGCs in the mouse retina. This strategy utilizes hydrogel chemistry to physically expand brain and retina samples, enabling nanoscale analysis of synaptic properties. I report an experimental approach for studying ipRGC synaptic connectivity in the mouse retina that combines immunohistochemical synaptic protein staining, cellular labeling of RGCs, and ExM imaging to achieve an ∼4x isotropic increase in spatial resolution, and describe the challenges that I encountered.

MELANOPSIN AND PACAP IN INTRINSICALLY PHOTOSENSITIVE RETINAL GANGLION CELLS REGULATE THE DEVELOPMENT OF RETINOFUGAL PROJECTIONS IN MICE

by

César Javier Hernández

Dissertation submitted to the Faculty of the Graduate School of the
University of Maryland, College Park in partial fulfillment
of the requirements for the degree of
Doctor of Philosophy
2025

Advisory Committee:
Associate Professor Colenso M. Speer, Chair
Professor Ricardo C. Araneda
Professor Joshua H. Singer
Professor Jason W. Triplett
Associate Professor Sougata Roy, Dean's Representative

Dedication

To Ellie, my lovely partner, my best friend, my greatest supporter.

"All that I am or ever hope to be, I owe to my angel mother."

Abraham Lincoln (1809 - 1865)

"I grew up with a younger brother, so I can get pretty rowdy."

Sarah Wynter

"Darkness cannot drive out darkness; only light can do that."

Martin Luther King Jr. (1929 - 1968)

Acknowledgments

I owe my sincere gratitude to all those who have made this thesis possible and who supported, advised, guided and encouraged me along my doctoral journey.

First and foremost, I would like to express my profund gratitud to my advisor, Professor Colenso M. Speer, for providing me with the invaluable opportunity to work on challenging and intellectually stimulating projects over the past five years. Thank you for your guidance, empathy, and never giving up on me. Your encouragement eased my worries, and your collaborative nature made me feel welcome in your laboratory. I have learned so much from you, both academically and personally, and I will remain deeply grateful for your mentorship.

I would like to thank the members of my examining committee, Dr. Joshua Singer, Dr. Ricardo Araneda, Dr. Jason Triplett and Dr. Sougata Roy for sharing your knowledge and support. Your expertise and insight helped me refine and improve my research. I would like to express my sincere gratitude to Professor Ricardo Araneda, who generously welcomed me into his laboratory when I arrived at the University of Maryland. His support and trust at the outset of my my doctoral training were invaluable, and his mentorship substantially enriched my intellectual development by teaching me physiology and affording me the opportunity to teach it at the Marine Biological Laboratory. Similarly, I would like to thank Professor

Joshua Singer, who afforded me the opportunity to learn retinal physiology during my raotation in his laboratory and who has provided unwavering support ever since.

I am grateful to all my lab mates, whose own research, collaboration, and support greatly aided me throughout this journey: Jaqueline Minehart, Dr. Chenghang Zhang, Dr. Rashmi Rashmi, and Dr. Tarlan Vatan. As well as lab mates in the Singer lab: Katherine Pizano, and Morgan Musgrove. Special thanks to undergraduate Rebecca Pomerat, who assisted with my experiments.

I am also grateful to the administrative staff of the Biological Sciences (BISI) doctoral program and to the staff members in the Department of Biology for their professionalism, assitance, and continuous support. I further thank the Imaging Core Facility in the Department of Cell Biology and Molecular Genetics at the University of Maryland, College Park, for providing access to the Leica Stellaris 8 and Zeiss LSM 980 microscopes, which were essential for this work.

And last, but certainly not least, I owe my deepest gratitude to my family –my espouse, Ellie Klerlein, and my brother, Jorge Ignacio Villa Hernández– whose their immense love and comforting support sustined me throughout this journey. I would not have been able to complete this degree without you both.

It is impossible to acknowledge everyone by name, and I apologize to anyone I have inadvertently omitted.

Table of Contents

List of Figures

List of Abbreviations

α	alpha
$\sim$	approximately
°C	degree Celsius
$>$	greater than
$<$	less than
% (v/v)	volume/volume percentage
% (w/v)	weight/volume percentage
cm	centimeter
g	grams
h	hours
mL	mililiters
mM	milimolar
M	molar
nm	nanometer
min	minutes
RT	room temperature
µg	micrograms
µL	microliters
µm	micrometer
µM	micromolar
µs	microseconds

AA	Acrylamide
AC	Adenylate cyclase
ADAM	A disintegrin and metalloproteinase
Akt	Protein kinase B
AMPAR	α-amino-3-hydroxy-5-methyl-4-isoxazolepropionic acid receptor
APS	Ammonium persulfate
AVP	Arginine vasopressin
BDNF	Brain-derived neurotrophic factor
BIS	N-N'-methylenebisacrylamide

Brn3b	Brain-specific homeobox 3b
CAMK	Ca^{2+}/calmodulin-dependent protein kinase
cAMP	Cyclic adenosine monophosphate
CG	Coverglass
Cnga3	Cyclid GMP-gated channel A-subunit 3
CREB	cAMP response element-binding protein
CTB	Cholera toxin subunit B
DAC	Dopaminergic amacrine cell
DAG	Diacylglycerol
DDCS	Dendro-dendritic chemical synapses
DI	Deionized
dLGN	Dorsal lateral geniculate nucleus
DTA	Diphtheria toxin
EDTA	Ethylenediaminetetraacetic acid
EGFP	Enhanced green fluorescent protein
EFGR	Epidermal growth factor receptor
EM	Electron microscopy
EPSC	Excitatory postsynaptic current
ERK	Extracellular signal-regulated kinase
ExFISH	Expansion microscopy of Fluorescent in situ hybridization
ExM	Expansion microscopy
ExR	Expansion retrieval
FAK	Focal adhesion kinase
FISH	Fluorescent in situ hybridization
GABA	Gamma-aminobutyric acid
GCL	Ganglion cell layer
GFP	Green fluorescent protein
GFAB	Glial fibrillary acidic protein
GHT	Geniculohypothalamic tract
GLAST	GLutamate aspartate transporter
GLT-1	Glutamate transporter 1
GPCR	G-protein-coupled receptor
GRP	Gastrin-releasing peptide
Gnat1	Guanine nucleotide-binding proten α-transducin 1

HCl	Chloride
iExM	Iterative expansion microscopy
IGL	Intergeniculate leaflet
IPL	Inner plexiform layer
ipRGC	Intrintic photosensitive retinal ganglion cell
jDCV	Joint Deconvolution
LTP	Long-term potentiation
MA-NHS	Methacrylic acid N-hydroxysuccinimidyl ester
MAPK	Mitogen-activated protein kinase
MEK	Mitogen-activated protein kinase kinase
MMP	Matrix metalloproteinase
MORF	Mononucleotide repeat frameshift
mTOR	Mammalian target of rapamycin
NaCl	Sodium chloride
NHS	N-Hydroxysucinimide
NMDAR	N-Methyl-D-aspartic acid receptor
OPN	Olivary pretectal nucleus
Opn4	Opsin 4 / melanopsin
PACAP	Pituitary adenylate cyclase-activating polypeptide
PAC1R	PACAP type 1 receptor
PBS	Phosphate buffered saline
PDK-1	Pyruvate dehydrogenase kinase 1
Per1	Period circadian protein homolog 1
Per2	Period circadian protein homolog 2
PFA	Paraformaldehyde
PI	Phosphatidylinositol
PI_3	Phosphatidylinositol trisphosphate
PI3K	Phosphoinositide 3-kinase
PKA	Protein kainase A
PKC	Protein kainase C
PLC	Phospholipase C
ProExM	Protein retention expansion microscopy
PYK2	Pyruvate kinase 2

RFP	Red fluorescent protein
RGC	Retinal ganglion cell
RHT	Retinohypothalamic tract
RMS	Root mean square
RNA	Ribonucleic acid
SA	Sodium acrylate
SC	Superior colliculus
SCN	Suprachiasmatic nucleus
SDS	Sodium dodecyl sulfate
SON	Supraoptic nucleus
tdTomato	Tandem dimer red fluorescent protein
TEMED	Tetramethylethylenediamine
TEMPO	4-hydroxy-2,2,6,6-tetramethylpiperidin-1-oxyl
TGF_{α}	Transforming growth factor alpha
TREx	Ten-fold robust expansion microscopy
TRIS	Trishydroxymethylaminomethane
Triton-X	2-[4-(2,4,4-trimethylpentan-2-yl)phenoxy]ethanol
TrkB	Tropomyosin receptor kinase B
TRPC	Transient receptor potential channels
vGAT	Vesicular GABA transporter
VIP	Vasoactive intestinal peptide
VPAC1R	VIP/PACAP receptor type 1
VPAC2R	VIP/PACAP receptor type 2
WD	Working distance
WGA	Wheat germ aglutinin

Introduction

In mammals, light perception occurs in the retina, which contains rod and cone photoreceptors that convert light into neural signals for image-forming vision and conscious perception. However, the retina also contains a third type of photoreceptor that regulates non-image forming visual processes. These specialized retinal ganglion cells (RGCs) express melanopsin, a distinctive photopigment that makes them photosensitive independent of rods and cones. Known as intrinsically photosensitive RGCs (ipRGCs), these cells relay light information to various brain regions that govern circadian entrainment [91], the pupillary light reflex [52], regulating sleep/arousal [79], mood [49], learning [102], and metabolism [27]. The significance of ipRGCs extends beyond these functions as their malfunction is implicated in a spectrum of human diseases including sleep disorders [24], neurodegenerative diseases [59], psychiatric conditions (schizophrenia, anxiety [69], depression [49]), autism [42], migraines [23], glaucoma [75], and seasonal affective disorder [23]. In modern society, the increase in artificial light sources and light pollution imposes new challenges for human health. Therefore, a comprehensive understanding of ipRGCs is crucial for unraveling the biological underpinnings of these ailments.

ipRGCs are intriguing not only for their melanopsin expression but also be-

cause they release a peptidergic transmitter known as pituitary adenylate cyclase-activating polypeptide (PACAP) to communicate [30]. ipRGC axons release both glutamate and PACAP in postsynaptic targets including the suprachiasmatic nucleus (SCN), intergeniculate leaflet (IGL), and olivary pretectal nucleus (OPN) [31], thereby modulating the sensitivity of these light-responsive systems [14]. PACAP not only regulates circadian rhythms [30], but it has been also been linked to contagious itch behavior [29], anxiety [72], metabolism [40], and reproductive behavior [87]. PACAP dysfunction has been linked to various psychiatric illnesses, including schizophrenia and bipolar disorder [107]. Notably, mice lacking PACAP display depression-like [35] and hyperactivity-like behaviors [96]. Understanding PACAP expression in ipRGCs reveals how light signals are not merely transmitted but modulated at the molecular level, identifying the mechanisms by which ipRGCs influence the development and functional organization of both image-forming and non-image-forming visual pathways.

During mouse development, ipRGCs can respond to light much earlier than rods and cones, suggesting that ipRGCs, through melanopsin and PACAP, may play important roles in the development of visual brain circuits [31, 94]. Despite the functional diversity of ipRGCs, the contributions of these two molecules to visual circuit development remains poorly understood. **I hypothesize that melanopsin and PACAP play essential roles in the development of visual brain circuits**. To test this hypothesis, I used tract tracing with eye injections and mesoscale imaging to assess ipRGC projections to the SCN and dorsal lateral geniculate nucleus (dLGN) of melanopsin ($Opn4^{Cre/Cre}$) and conditional ipRGC-specific PACAP

($Opn4^{Cre/+}$ / $Adcyap1^{fl/fl}$) knockout mice. I then tested and applied several approaches for super-resolution expansion microscopy (ExM) to investigate ipRGC synaptic connectivity in the retina and central visual brain areas.

This dissertation is organized into four chapters that examine the role of melanopsin and PACAP in ipRGC development and circuit formation. Chapter 1 describes the implementation and optimization of ExM protocols for imaging retinal tissue. I first present a standard ExM protocol for whole-mount retina, which produced a fragile gel with a low expansion factor and diminished fluorescent signal. I then describe an optimization process of using two alternative ExM protocols that successfully increased both the expansion factor and fluorescent signal intensity, yielding a robust gel with five-fold expansion and enhanced fluorescence. Chapter 2 examines ipRGC projections to the SCN and dLGN in melanopsin knockout mice. The results show that melanopsin regulates the development of ipRGC projections to the SCN, controlling the bilateral innervation of this nucleus and promoting eye-specific segregation in the dLGN. Chapter 3 investigates the role of PACAP in ipRGC projection development to the SCN. Interestingly, PACAP is also necessary for the normal eye-specific segregation in the dLGN. Chapter 4 proposes a general framework for understanding how melanopsin and PACAP in ipRGCs may regulate their own axonal development to the SCN while contributing to segregation in the dLGN. The chapter concludes with future directions and proposed experiments to identify the mechanisms underlying these developmental processes.

Chapter 1: Imaging Intrinsically Photosensitive Retinal Ganglion Cell Synaptic Connectivity Using Expansion Microscopy

1.1 Introduction

Imaging the synaptic organization of retinal ganglion cells (RGCs) requires super-resolution techniques that surpass the diffraction limit of conventional light microscopy. Retinal synapses are often < 200 nm in their maximal dimension, which is below the diffraction limit of light ($\sim$250 nm). This makes visualization of their structural and spatial organization accessible only through electron microscopy (EM). However, preparing samples for EM is labor intensive, the field of view is restricted to small areas, and the technique is incompatible with fluorescent labeling of synaptic proteins. Therefore, a method to study RGC synaptic organization at the nanoscale that is compatible with immunostaining and fluorescent reporter lines would be highly valuable.

Expansion microscopy (ExM) is a super-resolution imaging technique that overcomes these limitations. Instead of using of specialized microscopes and computational analysis [41, 48], ExM circumvents the diffraction limit by physically expanding the specimen using a chemical process. The technique synthesizes a

swellable hydrogel within a biological sample, which pulls biomolecules and labels apart in all directions with equal magnitude. This isotropic expansion physically magnifies the sample effectively increasing the apparent resolution of conventional microscopes [10, 13, 98]. The first ExM protocol, published in 2015 by Chen et al. [10] in the Boyden laboratory, demonstrated that samples could be expanded four-fold, to achieve a resolution of ∼70 nm. The ExM protocol follows a multistep process: a polyacrylate hydrogel is polymerized within the sample, biomolecules are anchored to the hydrogel, the tissue is mechanically relaxed, and finally the gel is expanded in water.

Since then, different laboratories have developed many variations of ExM to customize the technique for different sample types and labeling needs. Protein retention (proExM) allows the use of standard antibodies [13, 98], while ExFISH enables fluorescent in situ hybridization (FISH) visualization of RNA [11]. Iterative (iExM) [9] and ten-fold robust ExM (TREx) [16, 17] achieve higher expansion factors, and expansion revealing (ExR) [89] improves signal intensity. Each ExM variant modifies one or more of the five core steps common to all ExM protocols: labeling, anchoring, gelation, homogenization, and expansion (Fig.1.1).

However, despite this wide range of customized protocols, ExM methods have not been systematically optimized for the thin, fragile, multilayered tissue of whole-mount mouse retina. Several critical challenges prevent straightforward optimization of ExM protocols for retinal experiments. The layered organization of the retina must remain intact for proper structural analysis. Additionally, retinal cells are small, and many cellular processes are prone to distortion or uneven swelling.

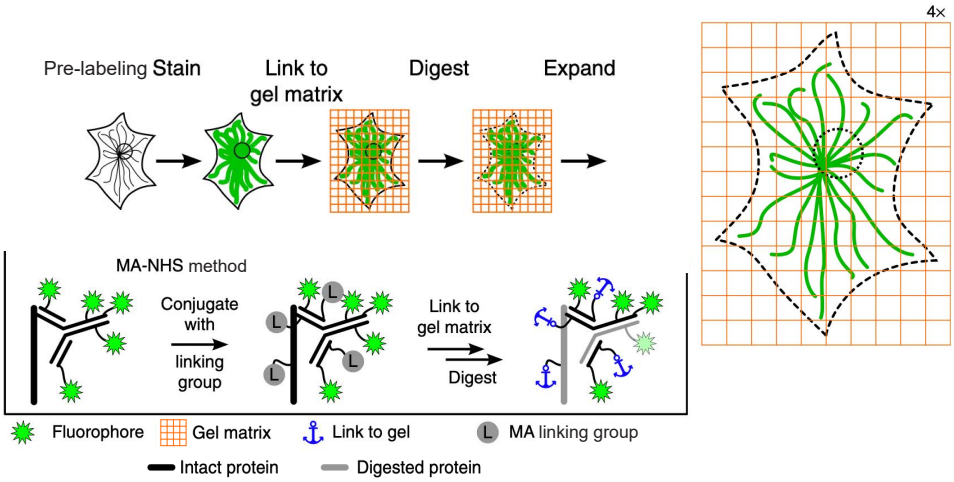

Figure 1.1: Diagram of proExM steps and label retention method. proExM consists of the following steps: labeling, anchoring, digestion, and expansion. The linker-group retention method uses Methacrylic acid (MA) to anchor the entire sample with polymer-linking groups after fluorescence histology with fluorophore-labeled antibodies. Fluorescent proteins of reporter animals are also anchored using the linker-group. (This figure is modified from Chozinski et al. [13].)

The natural spherical curvature of the retina makes it challenging to flatten the tissue without distortion. These challenges require systematic optimization of ExM protocols specifically for retinal tissue. Understanding ipRGC synaptic organization is particularly important because these cells undergo dramatic connectivity changes during development. Their projections to brain targets like the SCN and dLGN are refined through activity-dependent mechanisms, but the synaptic-level organization of these connections remains poorly understood. ExM provides the resolution needed to visualize these synapses while allowing us to identify ipRGCs using reporter lines.

Therefore, my goal was to adapt and optimize ExM protocols for whole-mount mouse retina. I began by implementing the standard proExM protocol (originally developed for brain tissue) and then evaluated TREx and ExR variants to identify a

workflow that optimally balances expansion quality, fluorescence preservation, and tissue integrity. Each protocol introduces a different chemical recipe for the hydrogel and a different tissue handling strategy. Together, they illustrate the process of optimizing ExM for a new tissue type. In this chapter, I describe the testing procedures, protocols, and imaging strategies I developed for expanding the mouse retina.

1.2 Methods

1.2.1 Mice

All animal procedures were carried out in accordance with protocols approved by the Institutional Animal Care and Use Committee (IACUC) of the University of Maryland, College Park. All mice were provided with food and water *ad libitum* and housed in a temperature controlled (22°C) room on a 12-hour light-dark cycle. I used both male and female C57BL/6J mice (JAX, # 000664) interchangeably. I also used several transgenic reporter lines. I used *Thy1*-YFP-H line (JAX, # 003782) for sparse RGC labeling. To label ipRGCs, I crossed $Opn4^{Cre}$ knock-in/knock-out mice (JAX, # 035925) [21] with reporter lines TIGRE-MORF (JAX, # 035404), MORF3 (JAX, # 035403), and Ai9 (JAX, # 007909) to generate $Opn4^{Cre/+}/TIGRE\text{-}MORF^{+/-}$, $Opn4^{Cre/+}/MORF3^{+/-}$, and $Opn4^{Cre/+}/Ai9^{+/-}$. Mice were anesthetized with isoflurane and euthanized by decapitation before retinal dissection. Both male and female (postnatal days 14 to 60) mice were used in all experiments.

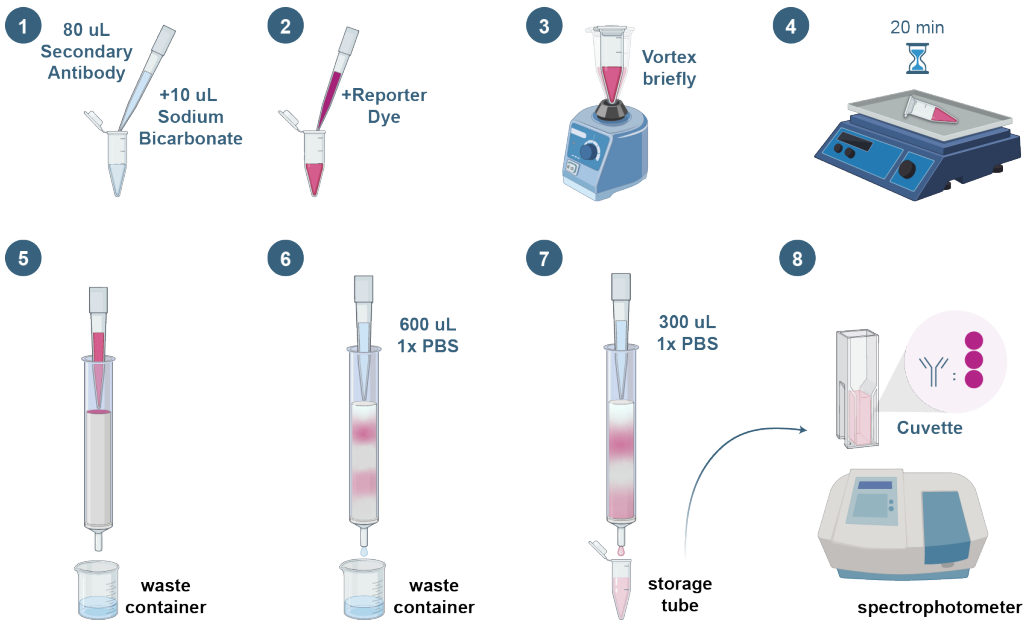

Figure 1.2: Diagram of custom secondary antibody conjugation. This approach enables fluorescent dye conjugation in higher ratios than commercially available pre-conjugated secondary antibodies, resulting in increased signal in ExM images.

1.2.2 Custom Antibody Conjugation

To increase fluorescence signal and reduce background, our laboratory produces custom secondary antibodies following Vatan et al. [103]. Briefly, 80 µL of secondary antibody [chicken anti-GFP, (Invitrogen, Cat# A10262); donkey anti-guinea pig, (Jackson ImmunoResearch, Cat# 706005148); donkey anti-mouse, (Jackson ImmunoResearch, Cat# 715005150); or donkey anti-rabbit, (Jackson ImmunoResearch, Cat# 711005152)] were mixed with 10 µL of 1 M $NaHCO_3$ (Fisher Scientific, Cat# S233) and 1.8-3.0 µL of NHS-ester dye [Atto488 NHS-ester, (ATTO-TEC GmbH, AD488-31); CF568 NHS-ester, (Biotium, Cat# 92131); or Atto647N NHS-ester, (Sigma-Aldrich, 18373 – 1MG-F)]. After a 20 min incubation, the conjugate was purified using a NAP-5 column (VWR, Cat# 95017009) equilibrated

in phosphate buffered saline (PBS), and the dye-to-protein ratio was determined spectrophotometrically (Fig.1.2).

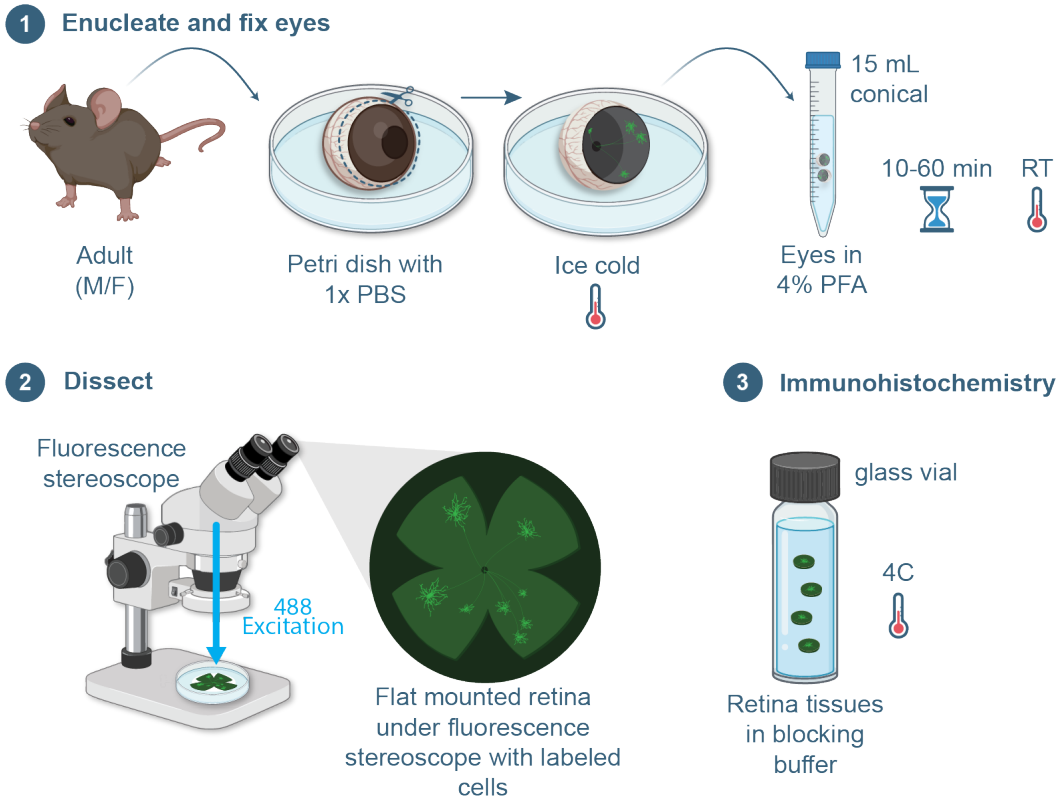

Figure 1.3: Diagram of mouse retina dissection, and fixation. After enucleation, corneas and lenses are removed and eye cups are fixed to protect retinal integrity. Fixation times are adjusted for optimal immunohistochemical labeling, and retinae are dissected and blocked.

1.2.3 Retina Dissection

Eyes were enucleated in cold PBS, and cornea and lens were removed before fixation of the eyecups in 4% paraformaldehyde (PFA, Electron Microscopy Sciences, Cat# 15710) at pH 7.4 for 10-60 min, optimized for the primary antibody staining. After three PBS washes, retinas were detached from the sclera, flattened,

and transferred to glass vials for immunostaining (Fig.1.3).

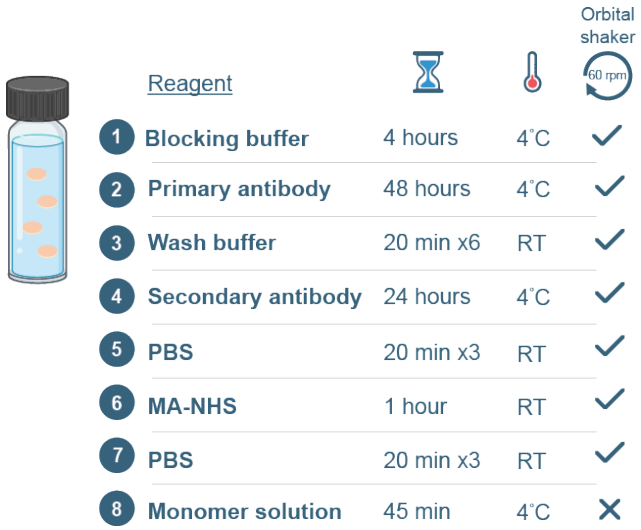

Figure 1.4: Diagram of mouse retina immunohistochemistry. After blocking and permeabilization, whole retinas are incubated with primary antibodies for 2 days and with secondary antibodies for an additional day. The ExM protocol starts with the addition of the MA-NHS linker-group and embedding of retina in the monomer solution.

1.2.4 Immunohistochemistry / Labeling

Immunostaining was performed as previously described in Vatan et al. [103]. In brief, tissues were blocked in buffer [10% donkey serum (Jackson ImmunoResearch, Cat# 017000121), 0.3% Triton X-100 (Sigma-Aldrich, X100PC) 0.02% sodium azide (Sigma-Aldrich, S2002) in PBS] at 4°C, for 4 hours, incubated with primary antibodies [chicken anti-GFP (Invitrogen, Cat# A10262), chicken anti-RFP (Synaptic Systems, Cat# 409006), mouse anti-Bassoon (Abcam, Ab82958), rabbit anti-ERC 1b/2 (Synaptic Systems, Cat# 143003), rabbit anti-Munc 13-1 (Synaptic Systems, Cat# 126103), rabbit anti-Piccolo (Synaptic Systems, Cat# 142003), mouse anti-

Gephyrin (Synaptic Systems, Cat# 147011), mouse anti-vGAT Synaptic Systems, Cat# 131011)] (dilution: 1:100) for 48 hours at 4°C, washed, and then incubated with custom secondary antibodies overnight. This protocol provided uniform labeling of retinal layers before embedding (Fig.1.4).

1.2.5 proExM Protocol

All stock and working solutions of proExM protocol [13, 98] were freshly prepared the same day of the experiment unless otherwise noted (Fig.1.5).

1.2.5.1 Anchoring

Whole retinas were incubated with 1 mM Methacrylic acid N-hydroxysuccinimidyl ester (MA-NHS, Milipore Sigma, 730300) in PBS for 1 h at room temperature followed by 3 washes with PBS.

1.2.5.2 Gelation

Retinas were then incubated in proExM monomer solution [2.5% (v/v) acrylamide (AA, Milipore Sigma, A4058), 8.625% (w/v) sodium acrylate (Milipore Sigma, 408220), 0.15% (w/v) N,N'-methylenebisacrylamide (bisacrylamide, Milipore Sigma, M1533), 2 M NaCl (Sigma-Aldrich, S9888), in 1 PBS] at 4°C for 45 min before gelation. Meanwhile, gelation chambers were built by fixing two #1 coverglasses (VWR, Cat# 48404-467) on top of a microscope slide (VWR, Cat#

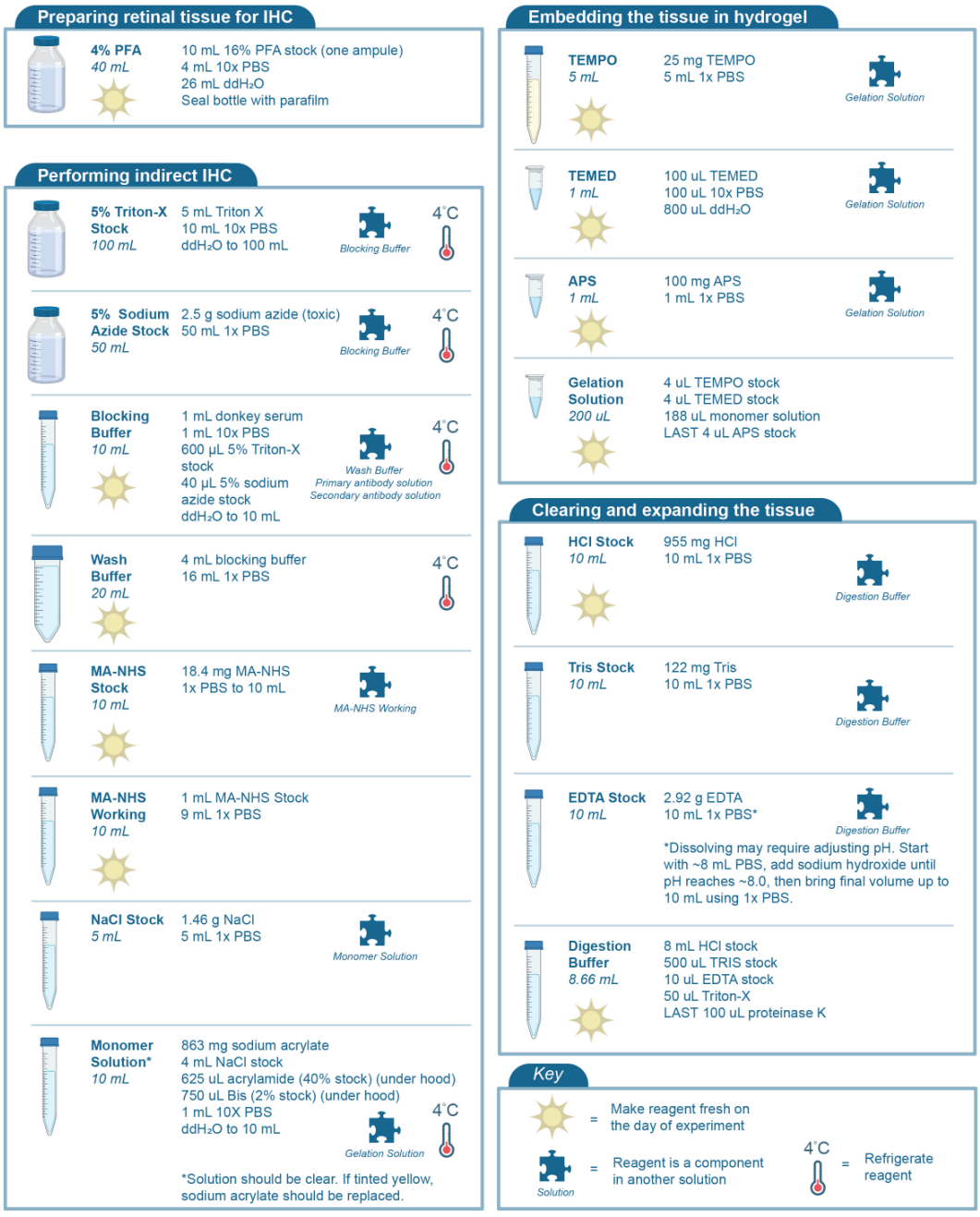

Figure 1.5: Preparation of stock and working solutions. Stock solutions of Triton X-100 and sodium azide were prepared in advance and stored for a maximum time of two months. The rest of the stock and working solutions were freshly prepared the same day of the experiment.

16004-422) with super glue to form a channel (Fig.1.6). Concentrated stocks of 10% (w/v) ammonium persulfate (APS, Milipore Sigma, A3678), 10% (v/v) N,N,N,N-Tetramethyl ethylenediamine (TEMED, Milipore Sigma T9281), and 1% (w/v) 4-hydroxy-2,2,6,6-tetramethylpiperidin-1-oxyl (TEMPO, Milipore Sigma, 176141) in PBS were diluted in monomer solution to concentrations of 0.2% (v/v), 0.2% (v/v), and 0.01% (v/v) respectively for gelation, with APS added last. The retina was placed between the coverglasses of the gelation chamber, ∼70 µL gelation solution was pipetted over the tissue and a coverglass was used to enclose the sample inside the gelation chamber. The samples were incubated for 2 h at 37°C (Fig.1.6).

1.2.5.3 Digestion and Expansion

The gelation chamber was carefully disassembled for the retina tissue/hydrogel hybrid to be punched out. Excess of hydrogel around the sample was removed, leaving a small circle of retina tissue/hydrogel hybrid that was then transferred to a 6 wellplate containing digestion buffer [0.8 M guanidine hydrochloride (HCl, Milipore Sigma, G3272), 50 mM TRIS (Sigma-Aldrich, T8524), 1 mM ethylenediaminetetraacetic acid (EDTA, Milipore Sigma, E9884), 0.5% (v/v) Triton-X, 8 units/mL Proteinase K (Milipore Sigma, P4850)] and incubated at 37°C overnight. The retina tissue/hydrogel hybrid was removed from the digestion buffer and placed in a plastic petri dish with DI water to expand. Water was exchanged 4 times every 15 min (Fig.1.7).

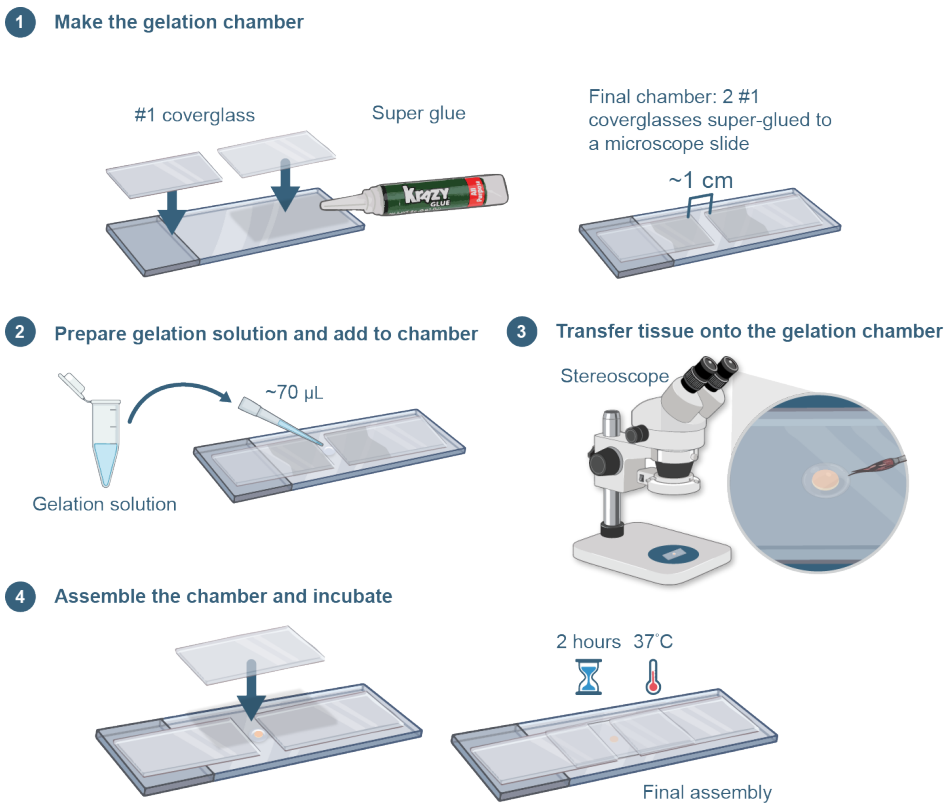

Figure 1.6: Gelation chamber assembly and retinal tissue gelation. Gelation chambers were built by super-gluing two #1 coverglasses on top of a microscope slide forming a channel of ∼1 cm width. Gelation solution is added, and the retina is carefully placed within the channel. The tissue is covered using a coverglass and polymerized at 37°C.

1.2.5.4 Mounting and Imaging

The expanded gel was removed from the petri dish using a spatula and placed in the imaging chamber. For imaging on an inverted microscope, the tissue/hydrogel hybrid was oriented with the ganglion cell layer (GCL) facing down, and placed on an imaging dish coated with poly-D-Lysine (WPI, Cat# FD35PDL100) (Fig.1.8, step 1). For imaging on an upright microscope, the tissue/hydrogel hybrid was

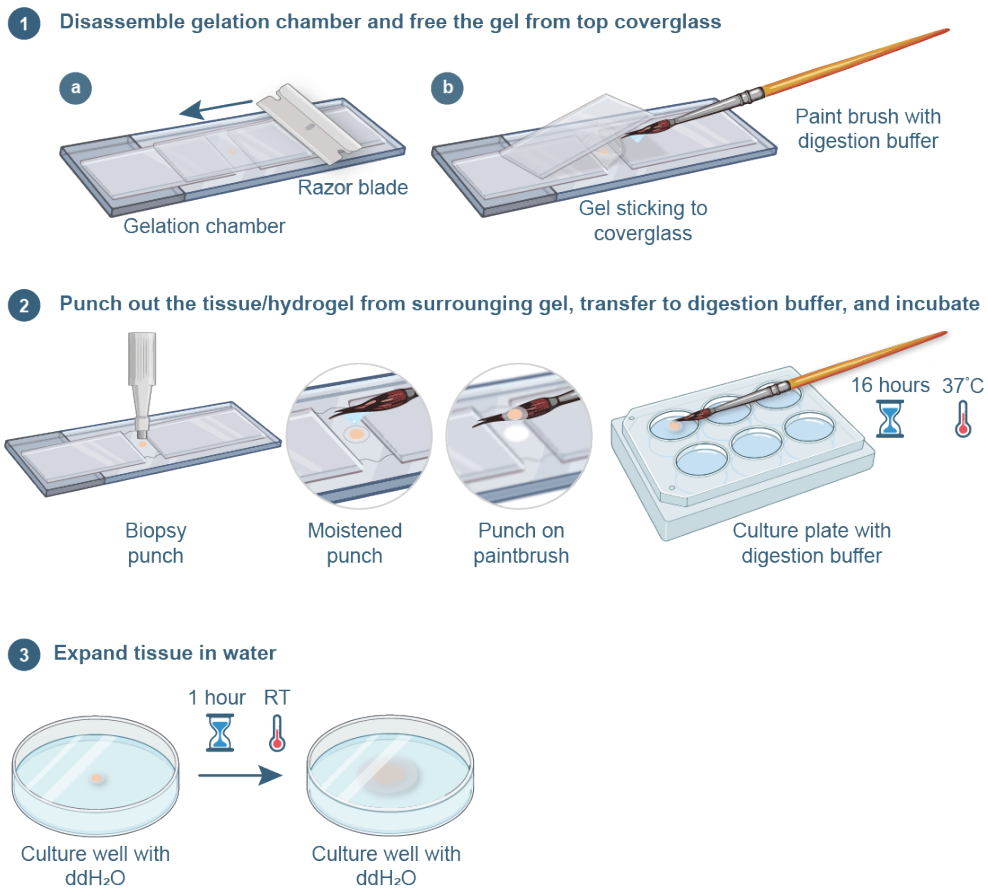

Figure 1.7: Digestion and expansion of retina. The gelation chamber was disassembled and the gelated tissue was punched out, transferred, and incubated with digestion buffer. Finally, the gelated tissue was expanded using deionized water.

oriented with the GCL facing up, and placed in a custom imaging chamber. Imaging chambers were built by gluing 2 silicone gaskets (ThermoFisher Scientific, P18174) onto the center of a microscope slide using epoxy to create a water-tight chamber. The expanded retina tissue/hydrogel hybrid was transferred to the center of the chamber, water was added until the gel was covered, a coverglass was placed on top, and the chamber was sealed using epoxy (Fig.1.8, step 2).

Confocal images were obtained using a 40x long working distance water immersion objective (LD C-Apochromat 40x/1.1 W Corr M27 (CG = 0.14-0.19 mm)

(WD = 0.62 mm at CG = 0.17 mm), UV-VIS-IR) and the Airyscan 2 with its 32-channel area detector of a Zeiss LSM 980 Airyscan 2 Laser Scanning Confocal microscope. Image stacks of 50 to 70 focal planes were collected in the Z dimension with a 0.25µm. Each focal plane was deconvoled with Airyscan Joint Deconvolution (jDCV).

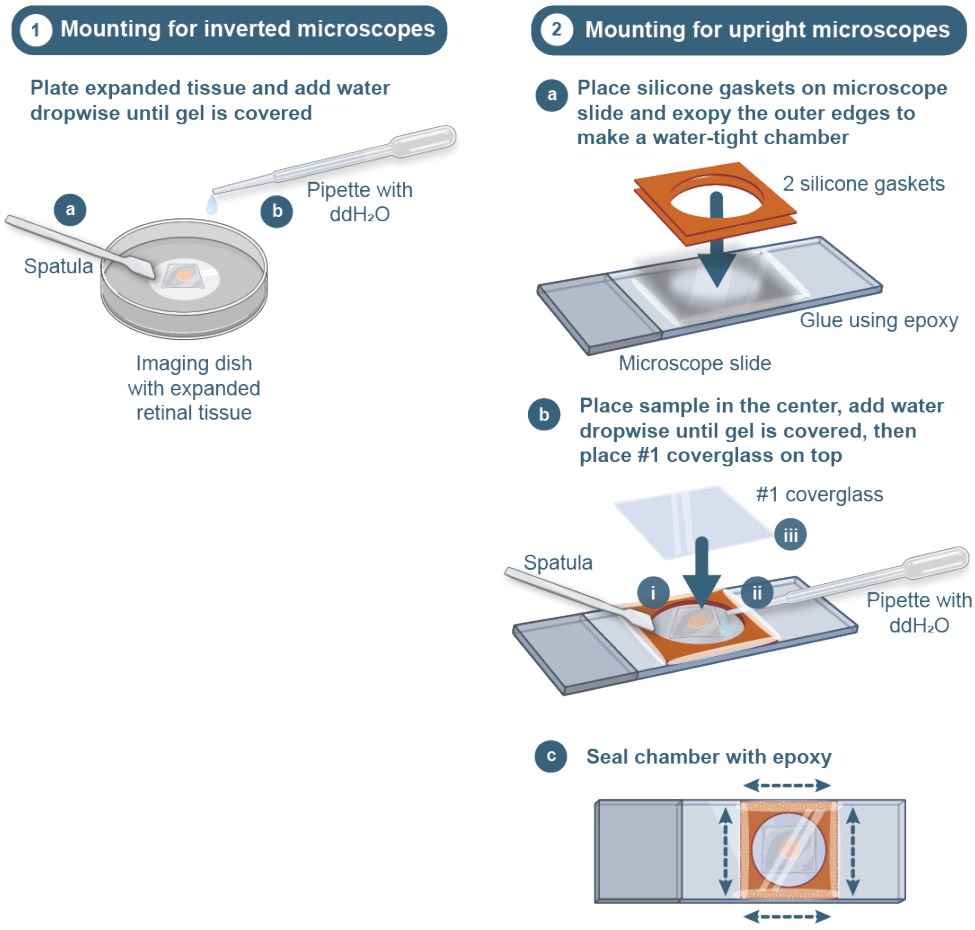

Figure 1.8: Mounting of expanded retina in imaging chambers. 1) For imaging on inverted microscopes, expanded retinae are placed in a bottom-glass petri dish treated with poly-D-lysine. 2) For imaging on upright microscopes, imaging chambers are constructed by gluing silicone gaskets to glass slides and sealing the expanded retinae inside the chamber with a coverslip.

1.2.6 TREx Protocol

The retina tissues were incubated with 1 mM MA-NHS in PBS for 1 h at room temperature followed by 3 washes with PBS. Retinas were then incubated in TREx monomer solution (14.22% (w/v) acrylamide, 10.35% (w/v) sodium acrylate, 0.03% (v/v) bisacrylamide, 2 M NaCl, in 1 PBS) at 4°C for 45 min before gelation. I built gelation chambers as described above and made the same concentration stocks of APS, TEMED, and TEMPO as in proExM. The TREx monomer solution was mixed with 0.15% (v/v) APS, 0.15% (v/v) TEMED, and 0.0015% (v/v) TEMPO for gelation, with APS added last. Retinas were placed in the gelation chamber as described for proExM, and incubated for 2 hours at 37°C. The gelation chamber was carefully disassembled and the small square of tissue/hydrogel hybrid was transferred to a 6 wellplate containing digestion buffer (0.8 M HCl, 50 mM TRIS, 1 mM EDTA, 0.5% (v/v) Triton-X, 8 units/mL Proteinase K) and incubated at 37°C overnight. The retina tissue/hydrogel hybrid was removed from the digestion buffer and placed in a plastic petri dish with DI water to expand. Water was exchanged 4 times every 15 min.

1.2.7 ExR Protocol

ExR protocol is a protocol in which samples are fixed, gelated, homogenized, and then immunolabeled prior to expansion. Briefly, eyes were enucleated, the cornea and lens were removed, and retinas were separated from scleras. The retina cups were then cut in half and transferred to a glass vial for fixation with a mixture

of 4% PFA and acrylamide of varying concentrations (4%, 10%, 15%, and 20% were tested, each at pH 7, 4) for 15-30 min depending on the primary antibodies used. The retina tissues were then washed 3 times for 10 min each with cold 1x PBS.

The retina tissues were then incubated in the same TREx monomer solution (14.22% (w/v) acrylamide, 10.35% (w/v) sodium acrylate, 0.03% (v/v) bisacrylamide, 2 M NaCl, in 1 PBS) for 45 min at 4°C before gelation. I built gelation chambers as described above and made the concentration stocks of APS, TEMED, and TEMPO as in TREx. The TREx monomer solution was mixed with 0.15% (v/v) APS, 0.15% (v/v) TEMED, and 0.0015% (v/v) TEMPO for gelation, with APS added last. Retinas were placed in the gelation chamber as described for proExM, and incubated for 2 hours at 37°C. The gelation chamber was carefully disassembled and the small square of tissue/hydrogel hybrid that was transferred to a 6 wellplate containing homogenization buffer [200 mM sodium dodecyl sulfate (SDS, Sigma-Aldrich, 436143), 200 mM NaCl, 50 mM TRIS at pH 9 in PBS] and incubated at 80°C overnight. The sample/hydrogel hybrids were then washed 6 times every 20 min in PBS with 1% (v/v) Triton X-100 (PBST) at 37°C to remove any trace of SDS. Then the tissues were washed 3 times every 5 min in PBS at room temperature.

Finally, hybrids were transferred to a glass vial for blocking and permeabilization in blocking buffer (10% donkey serum, 0.3% Triton X-100, 0.02% sodium azide in PBS) at 4°C for 4 h on an orbital shaker. Hybrids were incubated with primary antibodies (1:100) in blocking buffer at 4°C for 48 hours, followed by 6 washes for 20 min each with 20% blocking buffer at room temperature. Hybrids were then

incubated with secondary antibodies (1:100) in blocking buffer at 4°C overnight, followed by 3 washes for 15 min each with 1x PBS at room temperature. Then, hybrids were placed in a plastic petri dish with 4 exchanges of DI water for 15 min each.

1.3 Results

1.3.1 Protein Retention ExM (proExM) Protocol to Expand Retina

I first tested the proExM protocol [13, 98] to expand *Thy1*-YFP-H whole-mount mouse retina (Fig. 1.9). The expanded whole-mount retina revealed fine morphological details of YFP-H-expressing neurons, comparable to those observed with the original proExM protocol. To quantify the expansion factor, I imaged the entire retina at low magnification (2.5x) both before and after expansion. The lengths of several biological structures within the retina (e.g. neurites, soma) were measured in both images, and expansion factor was calculated as the ratio of post-expansion to pre-expansion dimensions. While the whole-mount retina expanded successfully, the expansion factor was ∼3.2x, which was lower than the standard 4-fold expansion factor reported for expanded brain tissue using proExM [13, 98] (Fig.1.9 box and whisker plot).

To further characterize the protocol, *Thy1*-YFP-H retinal tissues were immunostained to label YFP-H-expressing RGCs (anti-GFP) and presynaptic terminals with an antibody cocktail including anti-Bassoon, anti-Piccolo, anti-Erc1b/2, and anti-Munc-13. Postsynaptic terminals of inhibitory contacts were labeled with

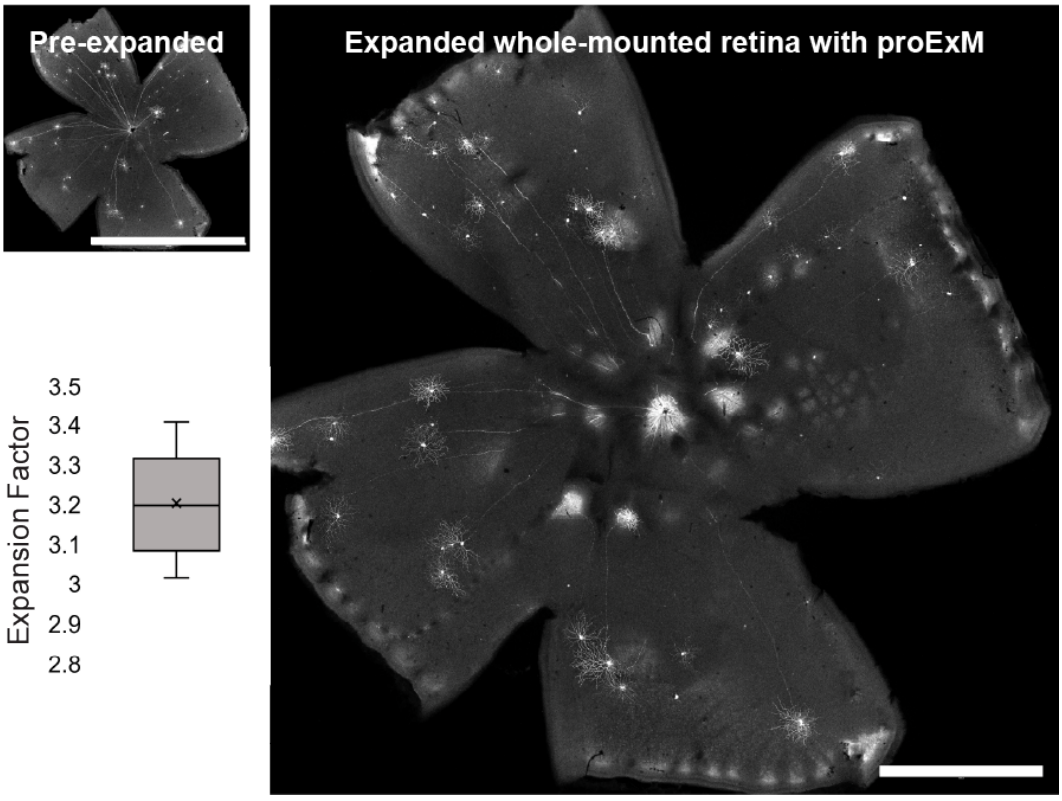

Figure 1.9: Whole-mount retina expanded using proExM. Maximum projection images show *Thy1*-YFP-H retina before and after tissue expansion (Scale bars = 1 mm). Whole-mount retina achieved ∼3x expansion using proExM (N = 10).

anti-Gephyrin antibodies. Primary antibodies were then labeled with custom secondary antibodies and the retinal tissues were treated with MA-NHS before gelation, digestion, and expansion.

While presynaptic and postsynaptic densities of inhibitory synapses were well resolved, some overlap between the signals was consistent with the smaller expansion factor previously measured in pre/post imaging controls. Despite using customized secondary antibodies, the fluorescent signal intensity was weak compared to pre-expanded samples (Fig.1.12). This is consistent with the loss of fluorescence during sample gelation as previously reported [98]. Due to the weaker signal,

higher laser powers were required to detect fluorescence, causing additional fading during imaging. The gel integrity also presented challenges. Retinal tissue expanded using proExM resulted in fragile gels prone to breakage during handling. Nonetheless, I successfully mounted the gel in the imaging chamber and imaged inhibitory synapses along dendrites. These distributed inputs to YFP-H-expressing RGCs could be located throughout the whole cell, including the soma and dendrites. Inhibitory synapses were also observed that do not colocalize with any YFP-H-expressing neurons, consistent with the presence of many non-YFP-H-expressing neurons. Furthermore, the presence of presynaptic signals with no accompanying gephyrin-positive postsynaptic densities suggests they could be excitatory presynaptic terminals (Fig.1.12).

1.3.2 Improving Expansion of Retina Tissue Using TREx and ExR Protocols

To optimize ExM for retina tissue, I aimed to achieve three improvements over the standard proExM protocol: 1) greater expansion factor to distinguish non-overlapping presynaptic and postsynaptic signals, 2) stronger hydrogel that was easier to handle, and 3) higher fluorescence intensity within the expanded retina. I tested two protocols, Ten-fold Robust ExM (TREx) [16, 17], and Expansion Retrieval (ExR) [58, 89], and compared their performance with proExM [13, 98].

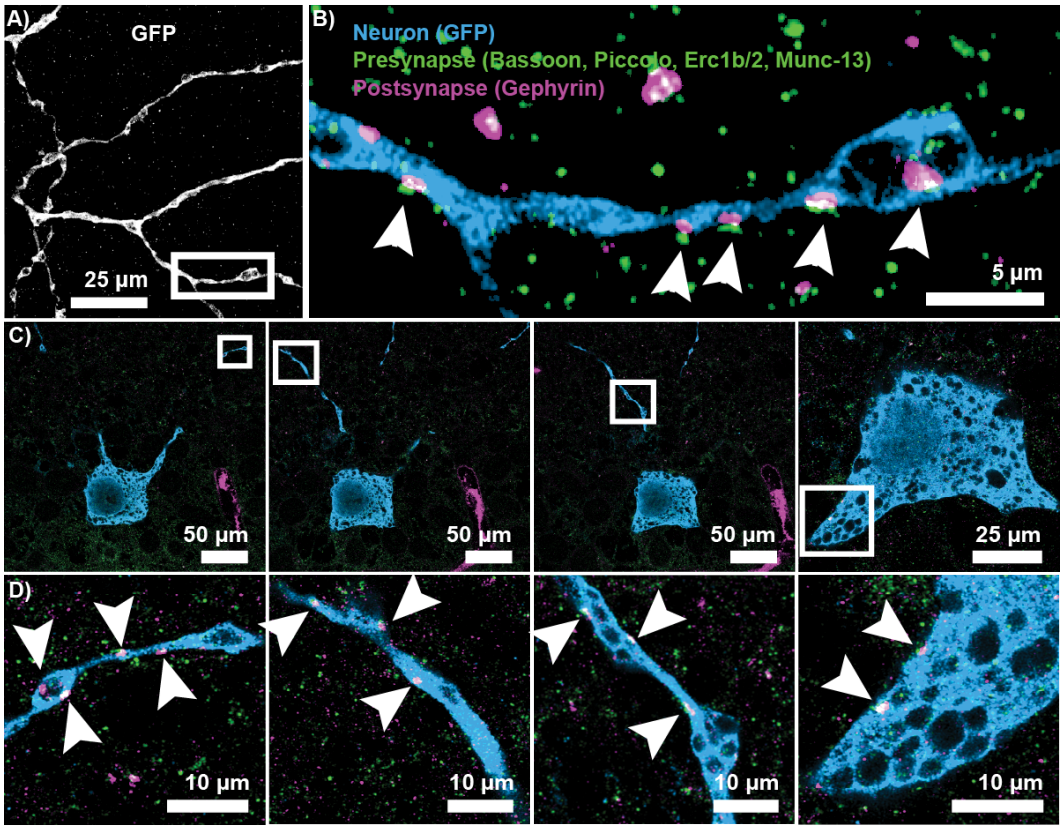

Figure 1.10: proExM super-resolution imaging of synaptic connections within whole-mount mouse retina. (A) Representative maximum intensity projection images of an expanded YFP-H-expressing RGC in a *Thy1*-YFP-H mouse (expanded dimensions: 124.8 x 124.8 x 15.29 µm). (B) Maximum intensity projection image of dendrite zoomed in with inhibitory synapses (arrowheads; presynaptic markers: Bassoon, Piccolo, Erc1b/2, Munc-13; postsynaptic marker: Gephyrin). (C) Single-plane images of a YFP-H-expressing RGC dendrites and soma receiving inhibitory synapses. (D) Zoomed-in single-plane images of inhibitory inputs (arrowheads) to a YFP-expressing RGC dendrites and soma. Scale bars represent post-expansion sizes.

1.3.2.1 TREx Protocol: Increasing Expansion Through Gel Chemistry

To increase the expansion factor while improving gel robustness, I tested the TREx protocol [16, 17], which expands brain samples 10-fold in a single step. TREx uses higher concentrations of sodium acrylate (10.35%) and acrylamide (14.22%)

combined with a lower concentration of the crosslinker bisacrylamide (0.005%). These higher concentrations of sodium acrylate and acrylamide increase the total monomer concentration, providing more polymer chains that can absorb water [16]. Sodium acrylate introduces anionic groups that repel each other during swelling, creating osmotic counter-ion pressure that drives the gel to absorb large amounts of water. Meanwhile, bisacrylamide introduces covalent bridges between polymer chains. By reducing the crosslinker concentration, the polymer network loosens, allowing the chains to stretch farther apart [16] (Fig.1.11 TREx).

Steps	ProExM	TREx	ExR
Fixation	4% Paraformaldehyde	4% Paraformaldehyde	4% Paraformaldehyde 4-30% Acrylamide (tested)
Labeling	Pre-expansion IHC	Pre-expansion IHC	Post-expansion IHC
Anchoring	1 mM MA-NHS	1 mM MA-NHS	N/A
Gelation	8.625% sodium acrylate 2.5% acrylamide 0.15% bis-acrylamide 2 M NaCl 0.01% TEMPO 0.2% TEMED 0.2% APS	10.35% sodium acrylate 14.22% acrylamide 0.03% bis-acrylamide 0.0015% TEMPO 0.15% TEMED 0.15% APS	10.35% sodium acrylate 14.22% acrylamide 0.03% bis-acrylamide 0.0015% TEMPO 0.15% TEMED 0.15% APS
Digestion	0.5% Triton X-100 0.8 M guanidine HCl 8 units/mL Proteinase K 50 mM TRIS 1 mM EDTA	0.5% Triton X-100 0.8 M guanidine HCl 8 units/mL Proteinase K 50 mM TRIS 1 mM EDTA	200 mM SDS 200 mM NaCl 50 mM Tris-HCl pH 9
Expansion Factor	~ 3.5x Expansion	~ 5x Expansion	? Unknown due to gel distortion
Comments	Reduced expansion factor; fragile gels	Increased expansion factor; stable gels	Fluorescent protein bleaching; unstable gels; tissue damage

Figure 1.11: Comparison of three ExM protocols to expand retina tissue. ProExM and TREx are pre-labeling protocols with an anchoring step, while ExR allows post-labeling of expanded samples by fixing proteins with a mixture of PFA and Acrylamide. The hydrogel recipe for ProExM differs from TREx and ExR. proExM and TREx use a digestion buffer that contains proteinase, while ExR uses a homogenization buffer to denature tissue. TREx improves expansion factor and hydrogel integrity. ExR damages retina tissue, bleaches fluorophores and produces unstable hydrogels.

This protocol balances swelling with mechanical integrity of the gel. If bisacry-

lamide concentration is too low, the gel becomes mechanically unstable and breaks easily. If it is too high, expansion is limited [16]. I optimized this trade-off by adjusting the crosslinker concentration. By increasing bisacrylamide concentration six-fold (0.03%), I achieved an expansion factor of ∼5x while improving gel robustness. The anchoring and homogenization steps remained the same as proExM (Fig.1.11 TREx).

1.3.2.2 ExR Protocol: Enhancing Fluorescence Through Post-Labeling

To further enhance fluorescence signal intensity, I tested the Expansion Revealing (ExR) protocol [58, 89] that enables post-expansion staining. Unlike proExM and TREx, which require antibody labeling before expansion, ExR allows labeling of expanded samples by making proteins accessible after tissue expansion.

ExR Chemistry and Mechanism

ExR uses a high acrylamide concentration (30%) mixed with 4% PFA in the fixation step to prevent covalent crosslinking between endogenous proteins while keeping them chemically intact and structurally accessible. During fixation, PFA generates reactive methylol groups on protein amines. The concentration of acrylamide determines whether these methylol groups form protein-protein crosslinks or anchor proteins to the gel. When acrylamide concentration is low, methylol groups react with nearby amines on neighboring proteins, forming methylene bridges within and between proteins. These intra- and inter-protein crosslinks cause proteins to

aggregate, blocking epitopes and hindering antibody binding [58]. However, when acrylamide concentration is high, the methylol groups preferentially react with acrylamide instead of neighboring proteins. This extinguishes protein-protein crosslinking, anchoring individual proteins to the forming hydrogel network [58].

Preliminary experiments using 30% acrylamide in the fixation step resulted in retina tissue damage. Therefore, I tested additional experiments with lower acrylamide concentrations (4% - 20%) (Fig.1.11 ExR). ExR also uses a homogenization buffer that differs from the digestion buffer used in proExM and TREx. Rather than containing proteinase, the ExR homogenization buffer contains strong detergents that solubilize membranes and clear lipids. Combined with heat (95°C) and reducing agents, these detergents denature proteins and dissociate non-covalent interactions between biomolecules. Despite this denaturation, proteins remain covalently anchored to the hydrogel network, preserving their native spatial locations [58, 89] (Fig.1.11 ExR).

1.3.3 Comparing TREx and ExR Performance

I compared the characteristics of the three protocols. The TREx gel was more robust, stable, and easier to handle than proExM. Measuring with a millimeter sheet of graph paper, TREx also achieved greater expansion than proExM. In contrast, the ExR gel did not expand properly, instead curling in on itself, making it difficult to image or measure the expansion factor. When I imaged the gels, the TREx experiment retained the fluorescence of YFP-H-expressing cells, and synaptic markers

were clearly visible. Because the gel expanded more, presynaptic and postsynaptic signals were separated by a clear gap, making individual synaptic structure distinguishable (Fig.1.12 TREx). In the ExR experiment, I tested four different acrylamide concentrations in the fixation step, which resulted in overlapping synaptic markers following expansion. At 4% acrylamide, the gel expanded the least, and signals from pre- and postsynaptic markers occupied the same locations. Increasing the acrylamide concentration to 10%, 15% and 20%, yielded inconclusive results concerning the expansion factor because all gels curled, preventing accurate measurement. Imaging of the synapses revealed increased separation of the synaptic densities with higher acrylamide concentrations. However, even at 20% acrylamide, the separation of synaptic signals was not as clear as in the TREx results (Fig.1.12 ExR).

1.3.4 TREx Expands Retina 5x to Resolve Presynaptic and Postsynaptic densities

Based on the comparison between proExM, TREx and ExR protocols, I concluded that TREx was the optimal choice for expanding retina tissue. To quantify the expansion achieved with TREx, I used the same measurement approach reported in the original expansion microscopy studies: imaging the same biological structures before and after expansion and analyzing them using the software *Elastix* [13, 56]. I measured retina tissue dimensions before and after expansion, specifically comparing the dendrites of YFP-H-expressing cells. This analysis revealed that the

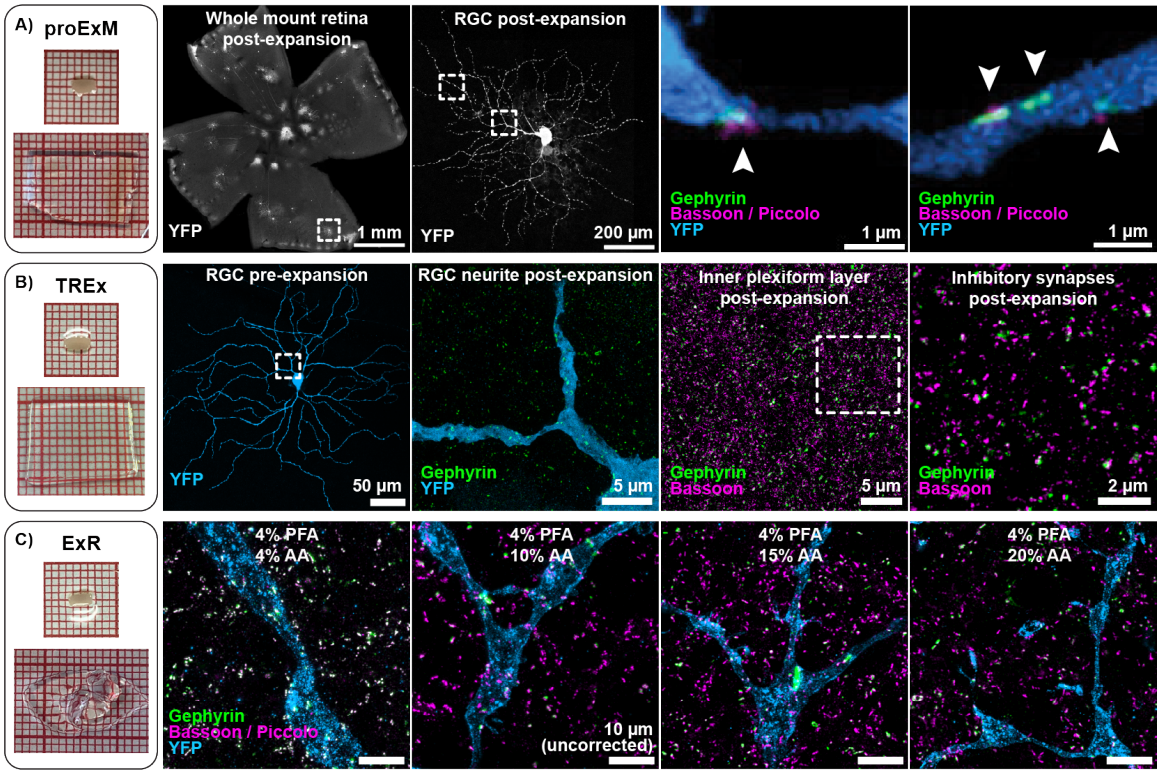

Figure 1.12: Comparison of three ExM protocols: proExM, TREx, and ExR. (A) Retina tissue expanded using proExM produces a reduced gel with an expansion factor of ∼3x. Fluorescence intensity is dim, and presynaptic and postsynaptic densities are colocalized. (B) Retina tissue expanded using TREx produces a larger gel with an expansion factor ∼5x. Fluorescence retention is stronger and presynaptic and postsynaptic densities are non-overlapping. (C) Retina tissue expanded using ExR produces an unstable gel that curls in on itself. While fluorescence signal is brightest with this protocol, synaptic densities are overlapping due to impaired expansion.

retina tissue expanded more than five-fold (Fig.1.13 Expansion Factor plot). This quantification matched the physical gel measurements obtained with graph paper. Next, I calculated the distortion introduced by the expansion using Elastix [56] as described by Chozinski [13]. I found that residual errors were lowest at the smallest spatial scales and peaked around 2µm, which is similar to the range of distortion reported in expanded brain tissue (Fig.1.13 RMSE plot).

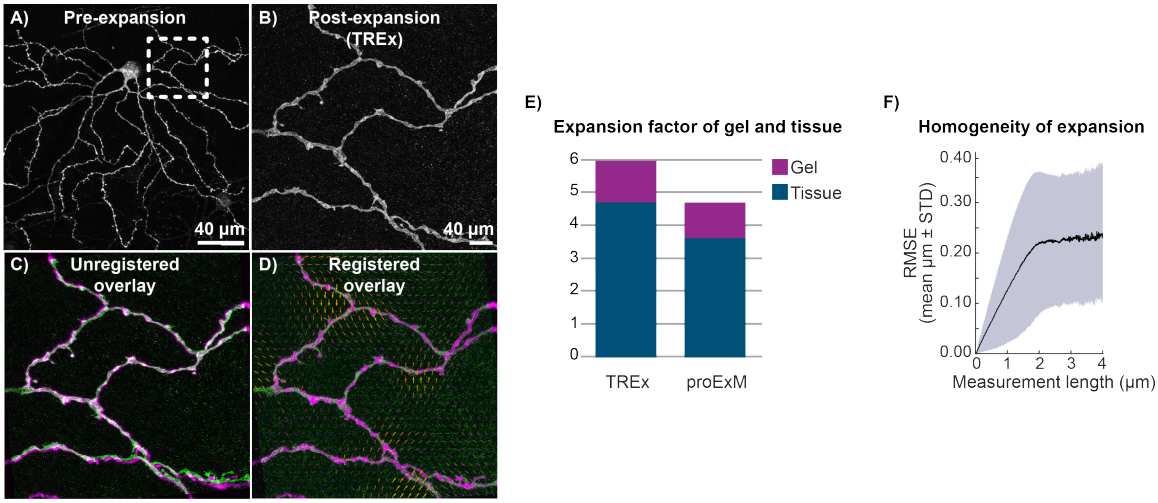

Figure 1.13: Quantification of expansion factors. (A, B) Representative maximum projection images of an RGC before (pre-expansion) and after expansion using TREx, registered by *Elastix*. (C) The unregistered overlay shows the juxtaposition of pre-expansion and post-expansion images, revealing distortions caused by expansion. (D) The registered overlay shows the result of *Elastix* registration. (E) Mean linear expansion factor was 3.5x for proExM and 4.7x for TREx (F) Root mean square error (RMSE) quantifies spatial offsets between aligned pre-expansion and post-expansion images, showing minimal distortion within 2µm.

1.4 Evaluating Mouse Reporter Lines for TREx Analysis of ipRGC Synaptic Connectivity

To investigate the synaptic connectivity of ipRGCs using TREx expansion microscopy, I tested different reporter mouse lines crossed with the $Opn4^{Cre}$ mouse to screen and compare their labeling patterns.

1.4.1 Using MORF Reporter Lines to Study ipRGC Synaptic Connectivity

To visualize ipRGC synaptic connectivity at high resolution, I needed a labeling strategy that would allow me to trace individual cells and their synaptic contacts. Dense labeling of all ipRGCs would result in overlapping dendrites and axons, making it impossible to distinguish the connections of individual neurons. Therefore, I used mouse mononucleotide repeat frameshift (MORF) reporter lines, which provide sparse, stochastic labeling when crossed with Cre driver lines [104].

The MORF system functions as a genetic translation switch. In the presence of Cre recombinase, the system produces fluorescent proteins that label only a subset of Cre-expressing cells, creating sparse labeling patterns ideal for tracing individual cell morphology [104]. This sparse labeling is particularly valuable for expansion microscopy because it allows visualization of complete dendritic arbors and individual synaptic contacts without the confounding overlap of neighboring cells.

1.4.1.1 MORF3 Reporter

I first tested the MORF3 reporter line, which labeled the cellular membrane through expression of a Cre-dependent farnesylated "spaghetti monster fluorescent protein containing many V5 epitope tags. When crossed with $Opn4^{Cre}$ mice, MORF3 produced sparse, stochastic labeling of ipRGCs with strong signal at the

plasma membrane (Fig.1.14 MORF3). However, MORF3 has an important limitation: the fluorescent signal is only detectable after immunostaining with anti-V5 antibody. This means that successful labeling cannot be confirmed until after completing the entire expansion and immunostaining protocol. Without visual feedback during tissue processing, it is difficult to optimize the protocol or troubleshoot problems before reaching the final imaging step.

1.4.1.2 TIGRE-MORF Reporter (Ai166)

To overcome this limitation, I tested the TIGRE-MORF (Ai166) reporter line, which also employs the MORF translation switch but expresses a Cre-dependent tetracycline-activated enhanced green fluorescent protein (EGFP). Like MORF3, crossing TIGRE-MORF with $Opn4^{Cre}$ mice produces sparse, stochastic labeling of ipRGCs (Fig.1.14 TIGRE-MORF). However, TIGRE-MORF offers a crucial advantage: labeled cells are directly visible without requiring additional immunostaining. This immediate visibility allows for quality control throughout the experimental process, from tissue dissection through expansion, making it possible to identify and address problems before investing time in the complete protocol.

1.4.1.3 Ai9(RCL-tdT) Reporter

As an alternative to the MORF reporters, I tested the widely used Ai9 (Rosa-CAGL-LSL-tdTomato-WPRE) reporter line, which has a *loxP*-flanked STOP cassette that prevents transcription of a red fluorescent protein variant (tdTomato)

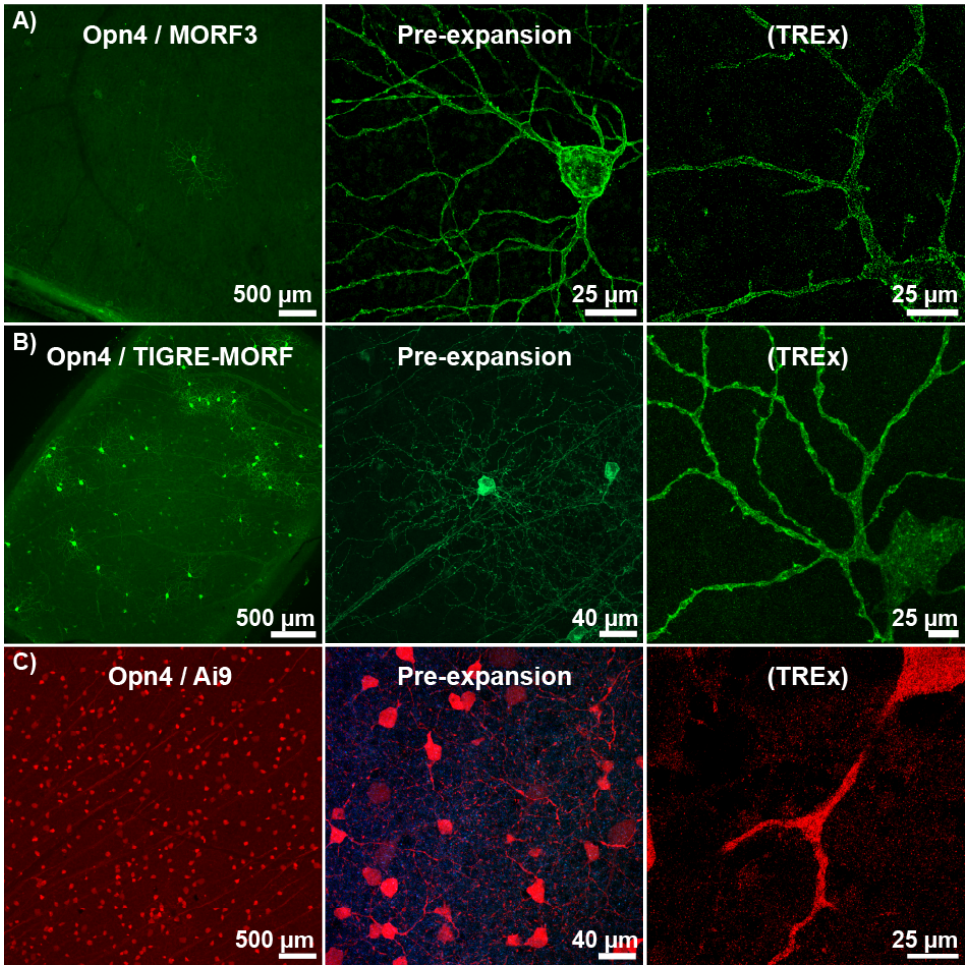

Figure 1.14: Different mouse reporter lines produce different ipRGC labeling density. $Opn4^{Cre}$ mice were crossed with either MORF3, TIGRE-MORF, or Ai9 reporter lines to label ipRGCs. Both (A) MORF3 and (B) TIGRE-MORF produce sparse, stochastic labeling of ipRGCs. MORF3 labels the cellular membrane after immunostaining with anti-V5 antibody. TIGRE-MORF expresses EGFP and ipRGCs are directly visible. (C) Ai9 expresses tdTomato in ipRGCs and many other cells. After retina expansion, MORF reporters maintain strong fluorescent labeling density. The Ai9 reporter shows weaker fluorescence signal. TREx scale bars are uncorrected for expansion factor.

[65]. Upon Cre-mediated recombination, the STOP cassette is excised, allowing constitutive expression of tdTomato. This reporter is popular in the neuroscience field because it provides strong, stable fluorescent labeling without requiring immunostaining. When crossed with $Opn4^{Cre}$ mice, the Ai9 reporter produced visible

tdTomato labeling in ipRGCs (Fig.1.14 Ai9). However, this reporter presented two significant problems for studying synaptic connectivity. First, the Ai9 line exhibited leaky expression, with tdTomato signal appearing in many non-ipRGC cell types. This off-target labeling created substantial background fluorescence that made it difficult to confidently identify and trace bona fide ipRGCs. Second, even in correctly labeled ipRGCs, the tdTomato fluorescence was distributed at relatively low density within individual cells, particularly in fine dendritic processes and potential synaptic sites.

These limitations became particularly apparent after tissue expansion. While MORF reporters maintained strong membrane-localized signal, the Ai9-labeled cells showed weaker, more diffuse fluorescence. This resulted in poorer resolution of fine morphological details, making it challenging to identify individual synapses or trace complete dendritic arbors with confidence. The combination of leaky expression and low labeling density made Ai9 unsuitable for the high-resolution synaptic connectivity analysis required for this study.

1.5 Evaluating an *Opn4*^{Cre} Line to Target ipRGCs

To investigate the synaptic connectivity of ipRGCs to their targets in the brain, I used an *Opn4*^{Cre} knock-in/knockout-out mouse line used by many laboratories in the field (JAX, # 035925) [20, 21, 38]. Due to variable melanopsin expression within each ipRGC type, diverse genetic tools have been developed to target ipRGCs from the *Opn4* locus. These tools vary considerably in their specificity and selectivity

when crossed to different reporter lines. For instance, the $Opn4^{tauLacZ}$ mouse line, which directly transcribes the reporter from the melanopsin locus, mainly labels M1 ipRGCs due to their high melanopsin expression levels [36]. However, the $Opn4^{Cre}$ mouse line that I used here is a more sensitive line that expresses Cre recombinase in all ipRGC types. Crossing this line to the Z/AP reporter ($Opn4^{Cre/+}/Z/AP$) revealed ipRGC morphological diversity and facilitated the study of type-specific and functional roles for ipRGCs [38, 67, 91].

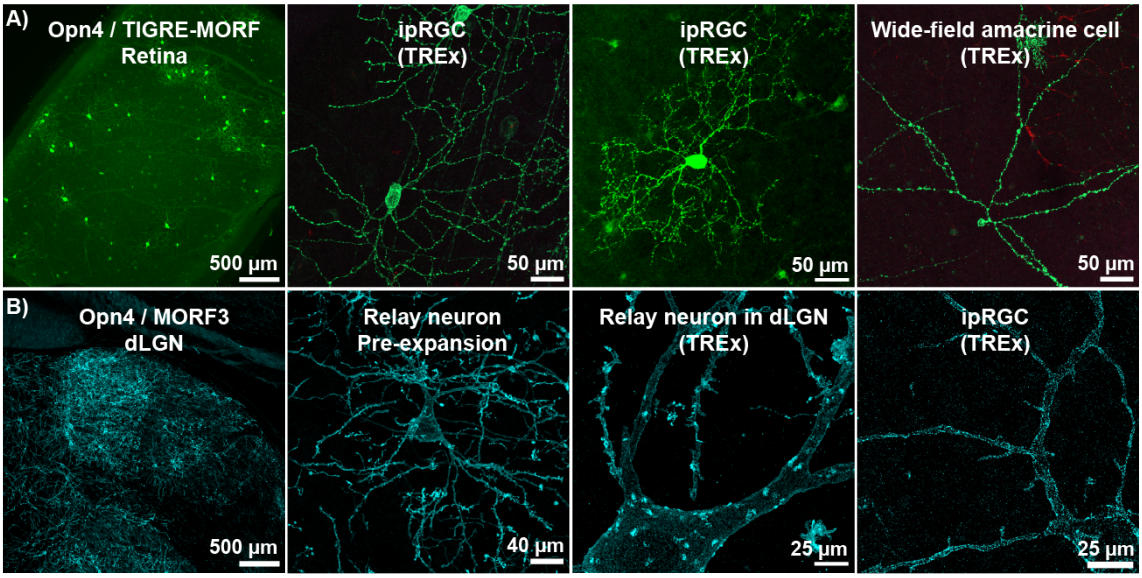

Figure 1.15: *Opn4Cre* mouse line crossed with MORF reporter lines produces off-target labeling. (A) The $Opn4^{Cre/+}$ / $TIGRE\text{-}MORF^{+/-}$ mouse line labels both ipRGC and non-ipRGC (e.g. wide-field amacrine cell) types in the retina. (B) The $Opn4^{Cre/+}$ / $MORF3^{+/-}$ mouse line labels retinal axons and off-target brain cells in the dLGN. TREx scale bars are uncorrected.

When I crossed the $Opn4^{Cre}$ mouse line to the *Cre*-dependent reporters MORF3 and TIGRE-MORF, I found recombination in off-target cells including many non-ipRGC cell types (e.g. wide-field amacrine cells) within the retina as well as neurons in the brain (Fig.1.15). This off-target labeling is well known and has been shown us-

ing different reporter lines (Ai9, Ai14) [20]. It has been suggested that this leakage problem arises due to the design of the $Opn4^{Cre}$ line. In this line, *Cre* recombinase was inserted under the *Opn4* promoter by deleting exon 1-9 of the melanopsin (*Opn4*) gene, and a human beta-globin intron was incorporated upstream of the *Cre* coding sequence [21]. This design was intended to produce robust expression in ipRGC with weak melanopsin expression. However, this additional regulatory element could drive off-target effects [20].

When I crossed *Opn4Cre* mouse line to the *Cre*-dependent reporters MORF3 and TIGRE-MORF produced recombination in off-target cells, labeling different ipRGC types and many non-ipRGC cell types (wide-field amacrine cell) within the retina and across the brain (Fig.1.15). This off-target labeling is well known as has been reported using different reporters lines (Ai9, Ai14) [20]. It has been suggested that this leakage problem could underlie in the design of the *Opn4cre* line. In this line, *Cre* recombinase was inserted under the *Opn4* promoter by deleting exons 19 of the melanopsin (*Opn4*) gene, and a human beta globin intron was incorporated upstream of the *Cre* coding sequence [21]. The reason for this design was to produce robust expression in melanopsin-weakly-expressing ipRGCs. However, this additional regulatory element could drive off-target effects [20].

1.6 Discussion

My goal in this work was to adapt expansion microscopy, a method originally optimized for brain tissue, to the mouse retina to visualize ipRGC synaptic con-

nectivity. Through systematic comparison of four ExM protocols, I identified key parameters that determine success in this fragile, multilayered tissue.

The standard proExM protocol demonstrated that retinal tissue can indeed expand isotropically and reveal subcellular details such as inhibitory synapses. However, protease digestion caused fluorescence loss, inconsistent labeling, and fragile hydrogels that were difficult to handle. The TREx formulation substantially improved gel robustness and fluorescence preservation through optimized monomer concentrations and reduced crosslinking, while maintaining approximately five-fold isotropic expansion. TREx became the practical foundation for ipRGC synaptic analysis.

I also evaluated a post-labeling strategy to enhance signal quality. ExR highlighted an important trade-off between tissue preservation and expansion factor: high acrylamide concentrations during fixation preserved protein epitopes but caused retinal curling that made the tissue difficult to image and measure. Despite producing the brightest fluorescent signals, ExR gels were too unstable for reliable use.

Across all protocols, the main challenges of applying ExM to retina were: (1) balancing fixation strength with tissue stability to prevent curling; (2) minimizing fluorophore quenching during polymerization; and (3) ensuring the gel remains flat and stable during imaging. The optimized TREx protocol successfully addressed these challenges, producing reproducible 4-5x expansion that preserved fine synaptic detail and allowed confocal imaging of individual ipRGCs and their inhibitory synapses.

1.6.1 Advantages and Applications

Compared with conventional immunofluorescence, the optimized ExM method provides a several-fold increase in spatial resolution using standard confocal microscopy. This enables visualization of presynaptic and postsynaptic puncta along ipRGC dendrites, quantification of synapse density and distribution patterns, and correlation of molecular markers within the same cell. The method is compatible with genetic reporter lines and fluorescent proteins, making it versatile for developmental and circuit-level studies. Because expansion is physical, samples remain optically clear and suitable for volumetric reconstruction.

Potential applications extend beyond the retina. The same workflow can be applied to map retinal axonal boutons in visual brain areas such as the SCN and dLGN where synaptic contacts group together within a small dendritic region, forming complex synaptic densities within a single bouton [8, 61]. For retinal research, the method opens possibilities to map inhibitory and excitatory networks, compare wild-type and mutant phenotypes, and quantify structural changes during development or disease.

1.6.2 Limitations

Despite these advantages, several limitations remain. Expansion factor can vary slightly between preparations depending on monomer purity, polymerization conditions, and ambient temperature. Some fluorophores, particularly red-shifted dyes, are quenched during polymerization. Very thick retinal gels are difficult to

image with high-numerical-aperture objectives due to working distance constraints and light scattering in expanded tissue.

Because expanded gels are mostly composed of water, they are mechanically fragile and susceptible to tearing during handling and mounting. Stage drift during long acquisition sessions can compromise image quality, requiring repeated refocusing or specialized mounting chambers. Additionally, while the method preserves overall tissue architecture, the expansion process may subtly alter the relative positions of some subcellular structures, potentially affecting precise spatial measurements at the nanometer scale.

1.6.3 Conclusion

Through systematic evaluation of multiple ExM protocols, I established an optimized expansion microscopy workflow for mouse retina that achieves 4-5 isotropic expansion while preserving synaptic architecture and fluorescent signal. The TREx-based protocol provides sufficient resolution to distinguish presynaptic and postsynaptic densities in ipRGCs using conventional confocal microscopy, transforming it into an effective super-resolution technique for retinal circuit study.

This method fills an important technical gap between conventional confocal microscopy and electron microscopy, providing molecular specificity and genetic accessibility while achieving resolution sufficient for synaptic analysis. The optimized protocol should prove useful for examining ipRGC circuit development and the roles of melanopsin and PACAP in shaping visual system connectivity, topics discussed

in the next chapters. By enabling visualization of synaptic contacts in intact tissue with molecular specificity, expansion microscopy provides a powerful tool for future studies of how ipRGC circuits are assembled during development and how they contribute to visual processing.

Chapter 2: Lack of Melanopsin Disrupts Development of ipRGC Bilateral Innervation to the SCN, and Subtly Impairs Eye-Specific Segregation in the dLGN

2.1 Introduction

Retinal ganglion cells (RGCs) receive visual information from rods and cones via bipolar and amacrine cells and transmit this information to various brain regions. A subset of RGCs express melanopsin, a photopigment encoded by the gene *Opn*4 [33, 36], which makes them intrinsically photosensitive and able to respond directly to light independent of rods and cones [19, 21, 33]. These intrinsically photosensitive RGCs (ipRGCs) convey both rod/cone-dependent and rod/cone-independent light information to non-image-forming brain areas, such as the suprachiasmatic nucleus (SCN), the olivary pretectal nucleus (OPN), and intergeniculate leaflet(IGL), as well as to image-forming brain areas including the dorsal lateral geniculate nucleus (dLGN) and superior colliculus (SC) [4, 33, 36]. Originally, ipRGCs were thought to mediate only non-image-forming visual responses such as circadian rhythms and the pupillary light reflex (PLR) [12]. However, recent work shows that ipRGCs also influence image-forming visual responses, including contrast sensitivity, spatial

pattern vision, and visual processing [21, 91].

2.1.1 ipRGC Diversity and Brain Targeting

ipRGCs are morphologically and functionally diverse. Six subtypes (M1–M6) have been identified based on dendritic arborization, soma size, stratification within the inner plexiform layer (IPL), photosensitivity, and electrophysiological properties [19, 21]. These subtypes form distinct brain circuits conveying light signals to different brain areas to modulate specific visual functions [19, 21]. Among these ipRGC subtypes, M1 ipRGCs show the highest expression of melanopsin and intrinsic light sensitivity [1]. M1 ipRGCs project primarily to the SCN and the OPN, the main non-image-forming brain areas for circadian photoentrainment and PLR, respectively [3, 38]. In contrast, multiple non-M1 ipRGC types (M2–M5) innervate image-forming brain areas such as the dLGN, contributing to spatial visual processing [4, 21]. These anatomical and physiological differences underlie distinct roles in transmitting light information to different brain circuits [4, 36] (Fig. 2.1).

2.1.2 Melanopsin and PACAP in ipRGC Signaling

iPRGCs are intriguing not only due to their melanopsin expression but also because they communicate using a peptidergic transmitter known as pituitary adenylate cyclase-activating polypeptide (PACAP) [30]. ipRGC axonal projections release glutamate, GABA and PACAP to postsynaptic targets in the SCN, OPN and IGL [31, 95]. Glutamate released from ipRGCs drives depolarization and gene expres-

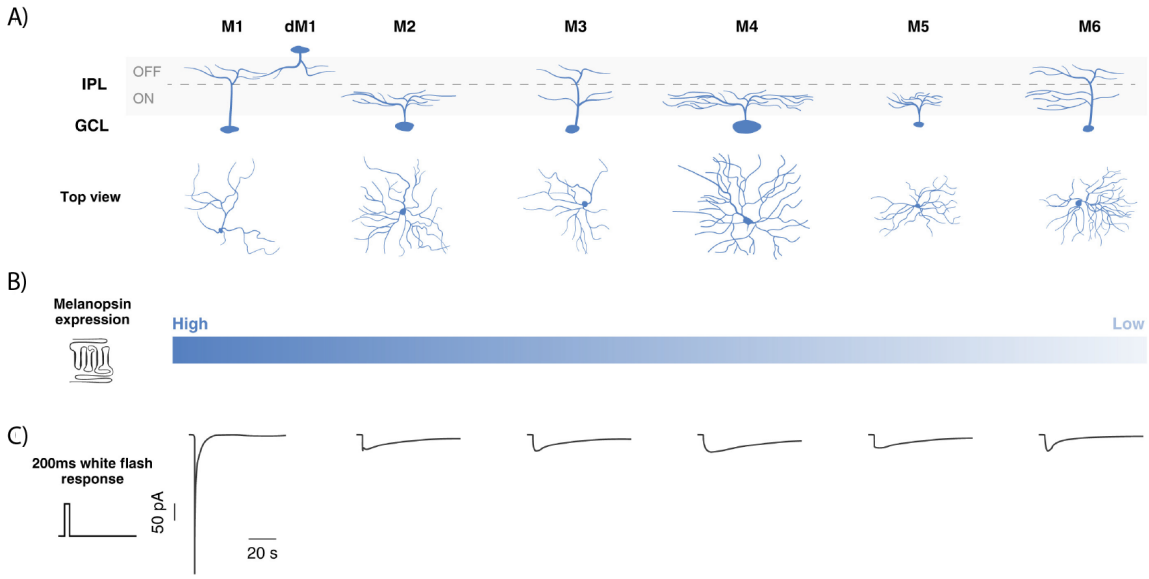

Figure 2.1: Diversity of ipRGCs. (A) M1-M6 ipRGC subtypes exhibit distinct morphologies, with dendrites stratifying in either the ON or OFF sublaminae of the inner plexiform layer. (B) Melanopsin expression levels vary across M1-M6 ipRGC subtypes, with M1 showing the highest expression. (C) Electrophysiological responses to 200ms light flashes differ among ipRGC subtypes, reflecting their functional diversity. The figure was adapted from Shen and Xue [93].

sion in SCN neurons, influencing the establishment of rhythmicity and tuning of circadian circuits [31, 82]. PACAP released from ipRGCs activates PAC1 receptors (PAC1R) that modulate synaptic plasticity and regulate intracellular cyclic adenosine monophosphate (cAMP) and Ca^{+2} signaling pathways responsible for neuronal differentiation and circuit maturation [30]. In this way, ipRGC neuro-transmitter release provides both fast excitatory drive and slower neuromodulatory signals that together may regulate the development of visual brain circuits.

2.1.3 ipRGCs Modulate Eye Development

Melanopsin expression begins around embryonic day 15 in mice, and ipRGCs become light responsive from birth [67]. A prominent characteristic of ipRGCs is that they can respond to light much earlier than rod and cones become functional [21, 92]. This early light sensitivity allows ipRGCs to influence multiple aspects of ocular development.

Melanopsin-dependent ipRGC signaling influences vascular branching in the retina [84] and modulates retinal cell number homeostasis by regulating apoptosis-mediated pruning of rod photoreceptors [20]. Loss of melanopsin also impairs cone organization within the outer nuclear layer through reduced ipRGC-dependent dopamine release from amacrine cells [101]. Beyond the retina itself, ipRGCs contribute to eye growth regulation [62].

ipRGCs also modulate spontaneous retinal activity during development. In $\beta 2$ knockout mice with disrupted stage II cholinergic retinal waves, light stimulation nearly doubled the frequency of retinal waves, indicating that ipRGC activation modulates the dynamics and recovery of spontaneous retinal activity through a light-dependent, melanopsin-mediated mechanism [54]. Moreover, ipRGC activity increases the duration of spike bursts during spontaneous retinal waves, influencing the refinement of retinofugal projections in the dLGN [12, 84, 99]. Early exposure to light can also increase ipRGC survival by suppressing apoptosis [45]. Thus, ipRGCs provide early light-driven signaling that promotes both eye and retinofugal development.

2.1.4 ipRGCs Support Brain Circuit Development

During development, ipRGCs provide the principal source of light information to multiple brain regions via the retinohypothalamic tract (RHT), shaping both visual and non-visual circuit formation [36, 38]. M1 and M2 ipRGC axons innervate the OPN, which mediates the PLR [63]. Multiples ipRGC types also project to the dLGN, where they contribute to the development of eye-specific segregation despite this nucleus receiving input primarily from conventional RGCs that convey rod- and cone-driven visual information [4, 12, 21].

Beyond visual circuits, ipRGCs regulate the development of non-visual brain regions. During early postnatal life, ipRGCs activate hypothalamic oxytocin neurons through direct innervation of the supraoptic nucleus (SON), which in turn promotes synaptogenesis in cortical and hippocampal pyramidal neurons [47]. Conversely, melanopsin-deficient mice show impaired dendritic spine maturation and reduced synaptic activity, resulting in long-term deficits in learning and memory [47]. These results highlight the importance of early light-driven signaling through ipRGCs for proper brain circuit development across multiple systems.

2.1.5 ipRGC Innervation of the SCN During Development

During an initial phase of SCN development prior to eye-opening, ipRGCs provide the only light-dependent input that the SCN receives [30]. While rod and cone photoreceptors are still maturing [54], ipRGCs express melanopsin and are functionally active from birth, exhibiting strong intrinsic calcium responses and

light-evoked action potentials [19, 67, 92].

The timeline of ipRGC innervation to the SCN follows a precise developmental sequence. Although ipRGC terminal axons reach the optic chiasm by E17, they stall transiently before entering the hypothalamus, delaying SCN innervation until birth. This timing overlaps with the late stage of SCN neurogenesis [3, 67]. After birth, initial ipRGC innervation of the contralateral SCN begins in the ventrolateral region at postnatal day 0-1 (P0-P1), while ipsilateral innervation appears in the ventromedial SCN. Bilateral innervation, in which ipsilateral and contralateral projections become intermingled, is established by P7. Adult-like retinal innervation density is reached by P14 [3, 31, 32, 33].

Traditionally, ipRGC projections were thought to target primarily the ventrolateral region or "core" of the SCN, which is populated by vasoactive intestinal peptide (VIP)- and gastrin-releasing peptide (GRP)-expressing neurons. The core is the main retinorecipient region, receiving direct ipRGC input via the RHT, and secondary ipRGC input from the intergeniculate leaflet (IGL) via the geniculohypothalamic tract (GHT), and input from the raphe nucleus [3, 32, 53]. In contrast, the dorsomedial region or "shell of the SCN is populated by arginine vasopressin (AVP) and calretinin-expressing neurons and was thought to receive minimal direct retinal input [8, 25, 32].

During development, ipRGC projections show a progressive expansion from ventrolateral to medial and dorsal regions, culminating in dense, bilateral innervation throughout the SCN [32]. However, recent evidence challenges the core-centric view, demonstrating that ipRGC projections innervate both core and shell regions.

Surprisingly, neurons in the shell receive denser ipRGC input than neurons in the core [8] (Fig. 2.2).

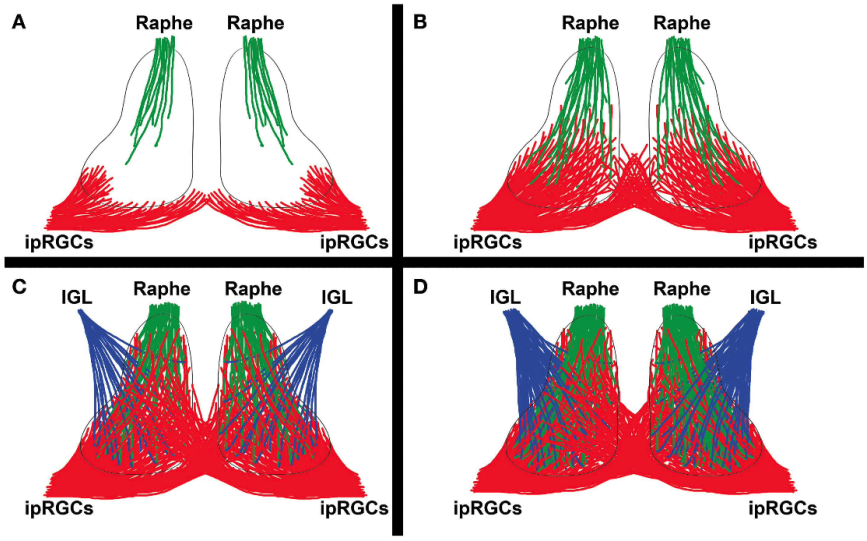

Figure 2.2: Developmental timeline of SCN afferent innervation. Schematic diagram showing the progressive development of SCN innervation from ipRGCs, raphe nuclei, and the IGL. (A) At birth (P0), ipRGCs begin to innervate the ventrolateral SCN contralaterally. (B) During the first postnatal week, ipRGC innervation becomes denser and expands to include the ipsilateral projections to the ventromedial SCN. (C) By approximately one week after birth (P7), contralateral and ipsilateral ipRGC axons intermingle, establishing bilateral innervation. (D) After eye opening (P14), ipRGC innervation of the SCN reaches mature density and distribution patterns. The figure was adapted from Bedont et al., [3].

2.1.6 Synaptic Organization of ipRGC Input to the SCN

SCN neurons extensively connect to each other and project to other hypothalamic and thalamic brain areas [105]. Within the SCN, neurons form a reciprocal synaptic network through dendro-dendritic chemical synapses (DCCS), which are associated with peptidergic neurotransmission [8]. These dendritic networks are complex and receive dense synaptic input from both retinal and non-retinal projections [53]. ipRGC axonal terminals are unmyelinated and form axonal arborizations

with few branches. These terminals primarily form *en passant* boutons that contact distal dendrites of SCN neurons. Each ipRGC axon synapses on multiple SCN neurons, and conversely, each SCN neuron receives input from multiple ipRGC axons, suggesting network synchronization that drives collective excitation [53]. While great progress has been made in understanding retinal input organization in the SCN, whether melanopsin is required for proper development of ipRGC projections to the SCN remains unknown.

2.1.7 Eye-Specific Segregation in the dLGN

In contrast to the SCN, development of retinal projections to the dLGN involves eye-specific segregation, a process by which RGC axons from both eyes that initially project to the same dLGN region and overlap extensively, become refined into distinct, non-overlapping territories. This segregation establishes the anatomical and functional basis for the relay of binocular information to the primary visual cortex [51]. Eye-specific refinement occurs during the first 10 postnatal days, before rod and cone photoreceptors become functional [54]. During this critical period, axons from one eye are weakened and retracted while axons from the other are stabilized and expanded, demonstrating that binocular competition is essential for segregation [51].

This segregation is driven primarily by spontaneous retinal activity in the form of retinal waves. Stage II cholinergic retinal waves, bursts of correlated activity sweeping across the retina, coordinate correlated firing within the same eye

and uncorrelated firing between eyes. These activity patterns provide signals that strengthen synaptic connections from the same eye, allowing the system to distinguish ipsilateral from contralateral inputs [2, 5, 51]. Disruption of retinal waves during the first postnatal week with epibatidine, a cholinergic agonist, prevents segregation. Conversely, suppression of retinal waves in only one eye shrinks its axonal territory in the dLGN while the region innervated by the active eye expands, demonstrating that relative activity levels determine competitive success [51].

2.1.8 ipRGC Contribution to dLGN Development

ipRGCs also project to the dLGN [4, 12, 21, 67]. Both conventional RGCs and ipRGCs begin innervating the dLGN prenatally E17, and both RGC types robustly innervate the dLGN by birth [67]. Non-M1 ipRGCs are the primary ipRGC subtypes that innervate the dLGN, clustering in the ventromedial region or core. ipRGC innervation in the dLGN is organized retinotopically, similar to conventional RGCs, suggesting that ipRGCs may participate in image-forming visual processes [21]. ipRGC axons make *en passant* synapses, forming large boutons with multiple spine intrusions and high mitochondrial content [53]. However, ipRGC boutons are sparse and their number is low relative to conventional RGC boutons, reflecting the sparse overall coverage of ipRGCs in the dLGN [53].

Functionally, ipRGCs influence retinal waves and eye-specific segregation. Light exposure prolongs retinal wave activity in neonatal mice and enhances eye-specific segregation of axons in the dLGN. This enhancement is abolished in *Opn4* knockout

mice [85]. Moreover, early ablation of ipRGCs through diphtheria toxin A (DTA) expression in the melanopsin locus disrupts segregation in the dLGN, suggesting that ipRGC activity is necessary for proper refinement of visual projections [12] (Fig.2.3).

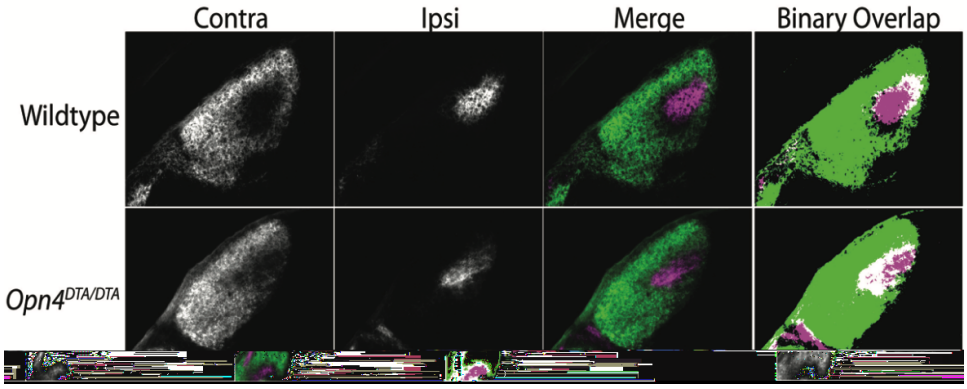

Figure 2.3: ipRGC ablation disrupts eye-specific segregation in the dLGN. Genetic ablation of ipRGCs by Cre-dependent diphtheria toxin A (DTA) expression disrupts eye-specific segregation in the mouse dLGN. The binocular overlap between contralateral and ipsilateral RGC projections reflect the overlay of thresholded and binarized images. This figure was modified from [12].

In summary, while ipRGCs provide the earliest light-dependent signals to the SCN and modulate circadian photoentrainment, whether melanopsin itself is required for proper development of ipRGC projections to SCN remains undetermined. Likewise, although ipRGC activity modulates retinal waves and enhances eye-specific segregation, the direct contribution of melanopsin signaling to the anatomical organization of dLGN innervation remains unresolved. To address these questions, I used tract tracing with eye injections and mesoscale imaging to analyze ipRGC projections to the SCN and dLGN in juvenile melanopsin ($Opn4^{Cre/Cre}$) knockout mice. This approach allows me to determine whether melanopsin expression is necessary for establishing proper ipRGC projection patterns to both

non-image-forming (SCN) and image-forming (dLGN) visual centers.

2.2 Methods

2.2.1 Mice

All mice were housed and treated in accordance with the NIH and IACUC guidelines, following protocols approved by the Institutional Animal Care and Use Committee of the University of Maryland, College Park. We used wild-type C57BL/6J mice (JAX, # 000664) as controls, and homozygous $Opn4^{Cre}$ knock-in/knock-out mice (JAX, # 035925), in which Cre recombinase was inserted under the *Opn4* promoter by deleting exons 19 of the melanopsin (*Opn4*) gene [21]. Therefore, homozygous $Opn4^{Cre/Cre}$ mice (hereafter designated as *Opn4*-KO) are melanopsin knockout animals.

2.2.2 Eye Injections with Cholera Toxin

Seven-day-old mouse pups (P7) were anesthetized with a constant flow of isofluorane. Eyes were injected intravitreally with 1.5 µL of cholera toxin subunit B conjugated with Alexa Fluor 488 (CTB-488) (Invitrogen, C22841) or Alexa Fluor 647 (CTB-647) (Invitrogen, C34778).

2.2.3 Brain Collection and Sectioning

Twenty-four hours after injection (P8), mouse pups were anesthetized by intraperitoneal injection of ketamine/xylazine reconstituted in 0.9% sterile saline.

Once unresponsive, pups were transcardially perfused with 7 mL of 0.9% sterile saline, followed by 7 mL of 4% paraformaldehyde (PFA, Electron Microscopy Sciences, pH 7.4). Brains were dissected and post-fixed in the same fixative at 4°C overnight. After fixation, brains were washed three times for 10 min each in PBS and immersed in 30% sucrose at 4°C for 24 hours for cryoprotection. Subsequently, tissues were embedded in a 2:1 mixture of OCT:30$ sucrose, frozen at −80°C, and cryosectioned coronally at 60 µm. Sections containing the SCN (Bregma -0.46 to -0.58 mm) and dLGN (Bregma -2.18 to -2.30 mm) were collected in PBS-filled well plates and screened under a fluorescence stereoscope. Selected sections were mounted with Vectashield (Vector Laboratories, Ref. H-1000-10). For each injection, the integrity of the retina was verified under the fluorescence stereoscope to ensure there was no injection-related damage. Only brains with intact, uniformly labeled retinas and even projection patterns in both the SCN and dLGN were included in the analysis. Any brain showing uneven or incomplete labeling was excluded.

2.2.4 Imaging

Brain slices were imaged using a Leica Stellaris 8 FALCON laser scanning confocal microscope housed in the Imaging Core Facility of the Department of Cell Biology and Molecular Genetics at the University of Maryland, College Park. Slices containing either the SCN or the dLGN were imaged individually using a Leica 20/0.75 NA objective with a zoom factor of 0.9, acquiring a single optical plane from each brain slice.

2.2.5 Quantification and Statistical Analysis

2.2.5.1 SCN One-Dimensional Profile Analysis

SCN images were pre-processed manually using FIJI (ImageJ) [90]. Briefly, images were individually cropped to remove the optic tracts, and additional cropping was performed to standardize image dimensions across all samples. Some images were flipped horizontally to align right and left eye projections for comparison. Images were converted to RGB format.

A custom MATLAB script was written to quantify one-dimensional projection profiles from each SCN image by extracting intensity profiles along the horizontal (X) and vertical (Y) axes. Knockout (KO) and wild-type (WT) cohorts were compared using two images per brain. Each image was loaded, converted to grayscale, and stored as double-precision arrays. The pixel size was 0.6684 μm per pixel for all spatial measurements.

For each image, an X-axis profile was calculated by averaging pixel intensities per column, and a Y-axis profile was calculated by averaging pixel intensities per row, producing one X-vector and one Y-vector per image. To improve signal-to-noise ratio while preserving anatomical trends, a bin size of 12 pixels was used.

Because slight translational offsets between animals can broaden group dispersion, profiles were aligned within and across cohorts before statistical analysis. All WT and KO profiles for a given axis were pooled to select a single reference profile that minimized the total least-squares alignment error when every other profile was

circularly shifted against it. For direct group comparison of mean profiles, the KO mean was additionally aligned to the WT mean using the same least-squares shift procedure, and the same shift was applied to the KO bootstrap confidence intervals to maintain correspondence.

Statistical comparisons were performed on the aligned profiles using two complementary non-parametric tests designed to probe distributional and median differences without assuming normality. For each axis separately, the aligned WT and KO matrices were vectorized, and a two-sample Kolmogorov-Smirnov test was used as the primary distributional test, supplemented by a Mann-Whitney U (rank-sum) test. To contextualize effect magnitude, we computed a standardized mean-difference effect size (Cohen's d) from the pooled variance of the vectorized data. We also estimated achieved statistical power for the two-sample comparison.

2.2.5.2 SCN Two-Dimensional Profile Analysis

A custom MATLAB script was written to quantify two-dimensional projection patterns from each SCN image. First, the two images from each brain were averaged to yield a single 2D image per biological replicate. All inputs were converted to grayscale, and each image was normalized to 8-bit (0-255) intensity values.

To reduce intra-group anatomical variance, per-animal averages were non-linearly registered within each cohort. This was achieved by iteratively averaging the current registered stack and applying Gaussian smoothing (sigma = 2 pixels). Cohorts were then brought into a common anatomical frame via rigid alignment of the

group means, estimating a KO-to-WT transformation using monomodal registration. The resulting rigid transform (translation and rotation) was applied uniformly to all KO per-animal images, with WT images defining the reference space. Group averages, directional difference maps (WT > KO and KO > WT), and a difference map (WT – KO) were generated.

Statistical comparisons were performed on the rigidly aligned images. Each image was partitioned into non-overlapping 33-pixel regions, and for every region we computed the mean intensity and conducted two-sample *t*-tests (WT vs. KO). Multiple comparisons were controlled using the Benjamini-Hochberg false discovery rate (FDR) procedure applied to the full set of regional *p*-values to obtain *q*-values. Significance masks were defined under dual criteria: uncorrected ($p < 0.05$ and absolute mean difference > 5 intensity units) and FDR-corrected ($q < 0.05$ and absolute mean difference > 5 intensity units). For each region, we also calculated Cohen's d using group means and the pooled standard deviation. Cohort averages, difference maps, and statistical maps were plotted for visualization.

2.2.5.3 Eye-Specific Segregation Analysis

A custom MATLAB script was written to quantify eye-specific segregation in the dLGN from bilateral fluorescence images [99, 100]. For each image, a constant camera background was first removed from each channel using the first intensity percentile of that channel. Residual low-frequency background was then reduced using rolling-ball subtraction with a radius of 100 pixels.

Following background correction, each channel underwent contrast stretching. The dLGN region of interest (ROI) was manually selected on each image to restrict subsequent quantification to anatomically defined dLGN territory. Segregation was quantified using a symmetric index based on the pixel-wise logarithmic intensity ratio: $R = \mathrm{Log}_{10}(F_I/F_C)$, where R is the ratio, F_I is ipsilateral fluorescence, and F_C is contralateral fluorescence. The dominant peak in the left half of the distribution was located and used as a reference to place distributions on a common scale, aligning images despite global intensity offsets.

For visualization, full-field and ROI-masked heat maps were generated using a diverging blue-white-red colormap in which white denotes colocalization, red indicates ipsilateral dominance, and blue indicates contralateral dominance. For each processed image, descriptive statistics including variance and skewness of the shifted ratio distribution were calculated.

Finally, a genotype-level overlay was created to compare segregation between cohorts using the dLGN ROI from each image. Cohort means with standard deviation envelopes were plotted. The variance of the log distributions was quantified from the previously computed ratio maps by extracting variance values for each animal and comparing between groups using Welch's unpaired *t*-test, which accounts for unequal sample variances.

2.3 Results

To investigate the hypothesis that melanopsin plays a role in the development of ipRGC innervation to the SCN, and modulate eye-specific segregation in the dLGN, I analyzed the projection patterns of RGC axonal terminals in melanopsin ($Opn4^{Cre/Cre}$)) knockout mice [21]. I injected fluorescent anterograde tracers CTB-Alexa 488 (CTB-Alexa488) and CTB-Alexa 647 (CTB-Alexa 647) into the left and right eyes, respectively, of homozygous $Opn4^{Cre/Cre}$ and wild type mice at postnatal day 7 (P7) (Fig.2.4A). This developmental timepoint was chosen because cone and rod photoreceptors are not yet functional at P7, and only melanopsin is active, allowing assessment of melanopsin-specific contributions to circuit development.

Brains were harvested at P8, and coronal sections containing the SCN (Bregma -0.46 to -0.58 mm) and dLGN (Bregma -2.18 to -2.30 mm) were imaged to analyze the distribution patterns of the two tracers in both brain regions (Fig.2.4B).

2.3.1 Lack of Melanopsin Disrupts ipRGC Innervation to the SCN

To investigate the development of the innervations of ipRGCs to the SCN, I analyzed bilateral fluorescence intensity patterns in single-lane confocal images of coronal sections from P8 *Opn4*-KO and WT mice previously injected with CTB-Alexa488 in the left eye, and CTB-Alexa647 in the right eye.

While RGC terminals in *Opn4*-KO mice covered a similar spatial extent as in wild-type mice, the distribution pattern appeared different. To quantify these differences in detail, I pre-processed the images using a multi-step pipeline. First,

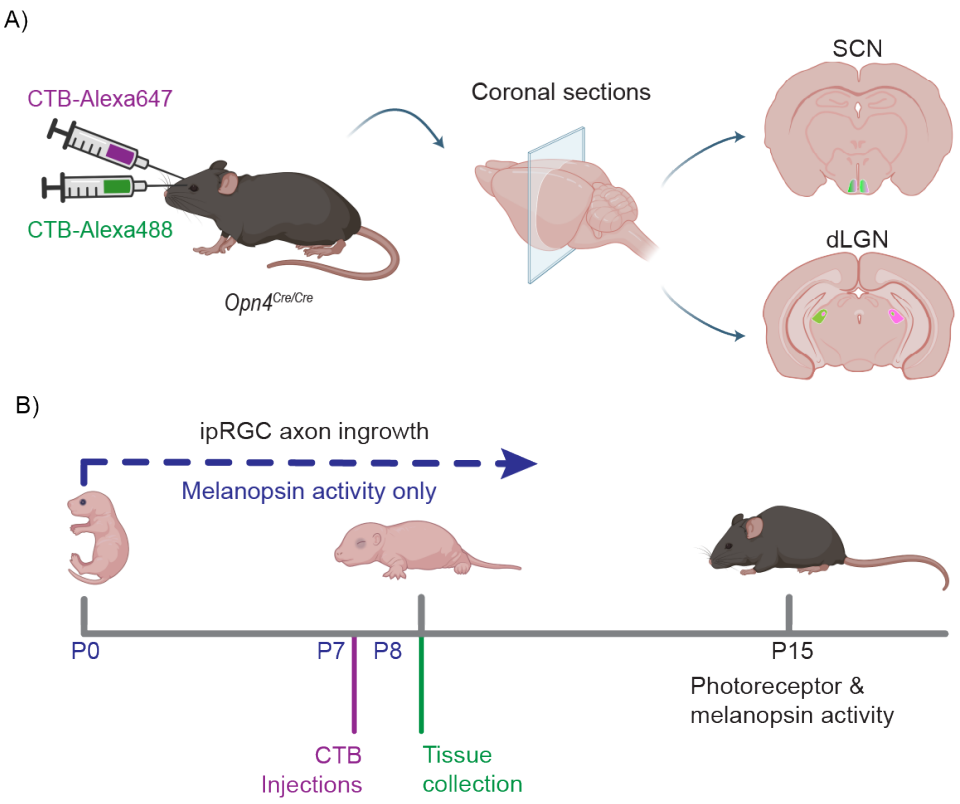

Figure 2.4: Experimental design to study RGC axonal projections. (A) Schematic of bilateral eye injection strategy. Intraocular injections of anterograde tracers CTB conjugated to Alexa Fluor 488 (green) or Alexa Fluor 647 (red) were used to visualize retinal projections from each eye to the SCN and dLGN in wild-type and *Opn4*-KO animals. (B) Developmental timeline showing melanopsin activity and photoreceptor maturation. Melanopsin signaling is active at birth and continues throughout development as ipRGCs form terminal axons in the brain. By day P9-P11, before eye opening, both photoreceptors and ipRGCs are functionally active. CTB injections (P7) and brain dissections (P8) were complete when melanopsin is the only source of visual input.

the bottom of each image was manually cropped to remove the optic tract. Next, all images were standardized to uniform dimensions (Fig.2.5, individual images showing CTB signal from both eyes). Finally, I generated average composite images and analyzed bilateral fluorescence intensity patterns using a custom MATLAB script (Fig.2.5).

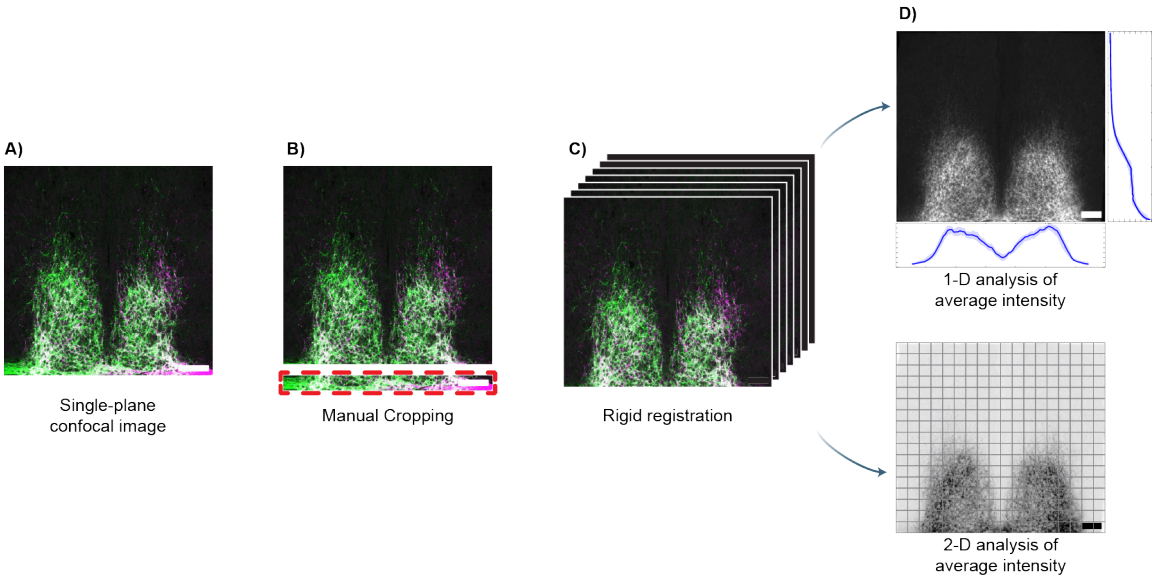

Figure 2.5: Pipeline for the quantitative analysis of retinohypothalamic projections to the SCN. Representative single-plane confocal images illustrating the methodological workflow used to quantify ipRGC projections to the SCN. (A) Raw confocal image depicting bilateral ipRGC innervation of the SCN in P8 mice, with axon terminals labeled using CTBAlexa 488 (green, left eye) and CTBAlexa 647 (magenta, right eye). (B) Pre-processing step in which optic tracts were manually removed by cropping regions containing extraneous axonal bundles (highlighted by red square). (C) Pre-processed images after manual cropping to remove optic tracts (indicated by red squares in left column) and standardization to uniform dimensions. (D) Average composite images of SCN innervation from each genotype after noise reduction and alignment, used for quantitative analysis. Scale bars = 100 μm.

2.3.2 One-Dimensional Analysis Reveals Reduced SCN Innervation in Melanopsin Knockout Mice

To quantify differences in SCN innervation between genotypes, I performed one-dimensional analyses of fluorescence intensity profiles along both horizontal (X-axis) and vertical (Y-axis) dimensions. **X-axis analysis** measuring the average column fluorescence intensity, showed that P8 *Opn4*-KO mice exhibited significantly lower fluorescence intensity comparted to wild type controls, particularly in the me-

dial region of the SCN (*Opn4*-KO = 33.74 95% CI = 13.65, WT = 37.14 95% CI = 12.84) Kolmogorov-Smirnov test = 0.1686, $p < 0.001$; Mann-Whitney U test, $p < 0.001$ (*Opn4*-KO = 7 and WT = 5 mice) (Fig.2.6A). The effect size was small (Cohens d = 0.2556), with achieved statistical power of 0.70 for detecting this difference.

Y-axis analysis, measuring the average row fluorescence intensity, similarly showed significantly lower fluorescence intensity in P8 $Opn4^{Cre/Cre}$ mice compared to wild-type (*Opn4*-KO = 33.16 95% CI = 21.92, WT = 36.60 95% CI = 21.69). Kolmogorov-Smirnov test = 0.2083, $p < 0.001$; Mann-Whitney U test, $p < 0.001$ (Opn4 KO = 7 and WT = 5 mice) (Fig.2.6B). The effect size was very small (Cohens d = 0.1575), with achieved statistical power of 0.65.

2.3.3 Two-Dimensional Analysis Reveals Altered Spatial Distribution of SCN Innervation

To investigate the spatial distribution of these differences, I generated two-dimensional fluorescence intensity maps of the SCN. While P8 wild-type mice developed ipPRGC innervation that extended into the dorsomedial region of the SCN (Fig.2.7A), *Opn4*-KO mice showed ipRGC innervation that remained predominantly in the ventrolateral region of the SCN (Fig.2.7B). Effect size maps, expressed as Cohen's d, provided a standardized measure of the magnitude and spatial distribution of group differences (Fig.2.8A).

To compare the intensity maps between the groups, I ran independent *t*-tests

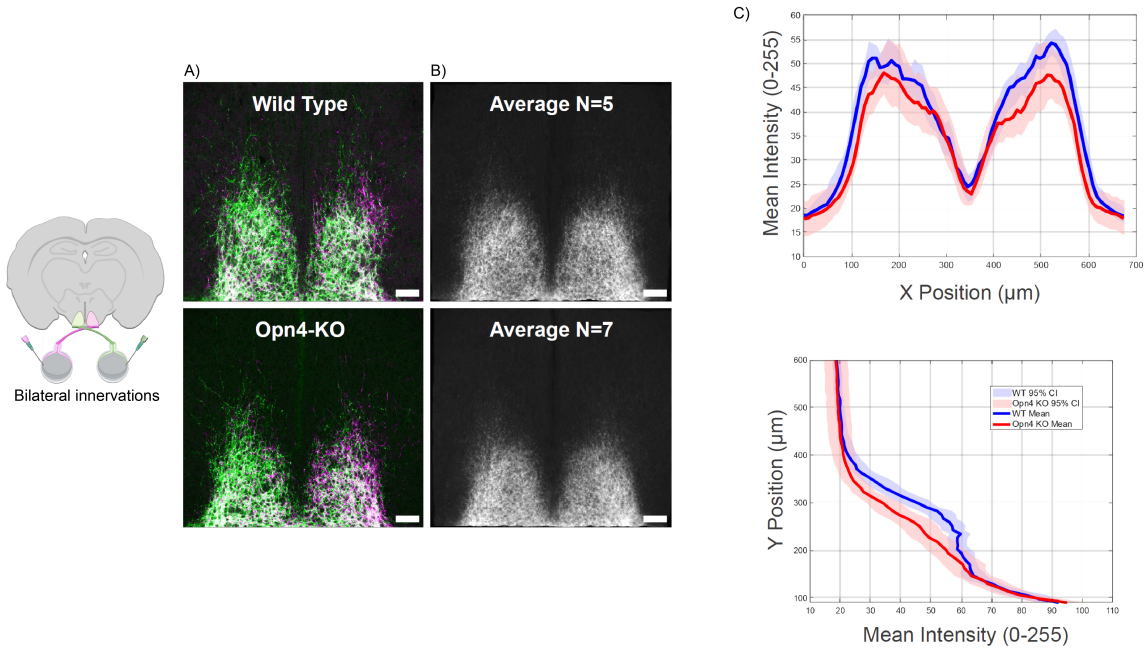

Figure 2.6: One-dimensional intensity analyses reveal that P8 *Opn4*-KO mice exhibit reduced ipRGC innervation in the SCN. (A) Representative single-plane coronal sections showing ipRGC axonal terminals labeled with CTB-Alexa 488 (green, left eye) and CTB-Alexa 647 (red, right eye) projecting bilaterally to the SCN in P8 wild-type and *Opn4*-KO mice. (B) Average composite images of bilateral SCN innervation from each genotype after noise reduction and alignment, used for one-dimensional intensity analyses. Both genotypes show bilateral innervation, though distribution patterns differ. Scale bar 50 μm. (C) Mean fluorescence intensity distributions are plotted along the horizontal X axis and vertical Y axis for bilateral innervations in P8 *Opn4*-KO (red) and wild-type (blue) mice. Shaded regions indicate bootstrap-derived 95% confidence intervals. Statistical comparisons between genotypes revealed significant differences along both axes. X-axis: Kolmogorov-Smirnov test = $p < 0.001$; MannWhitney U test, $p < 0.001$; Y-axis: Kolmogorov-Smirnov test = 0.2083, $p < 0.001$; MannWhitney U test, $p < 0.001$ (*Opn4*-KO N = 7 and WT N = 5 mice).

comparing image intensities between *Opn4*-KO and WT groups using rigidly aligned, mouse-averaged images. Each test compared mean fluorescence intensity across 3 3-pixel regions (2.0 x 2.0 μm), with significance determined by $p < 0.05$ and a minimum regional difference of 5 intensity units. Multiple comparisons were corrected using the Benjamini-Hochberg false discovery rate (FDR) procedure ($q < 0.05$).

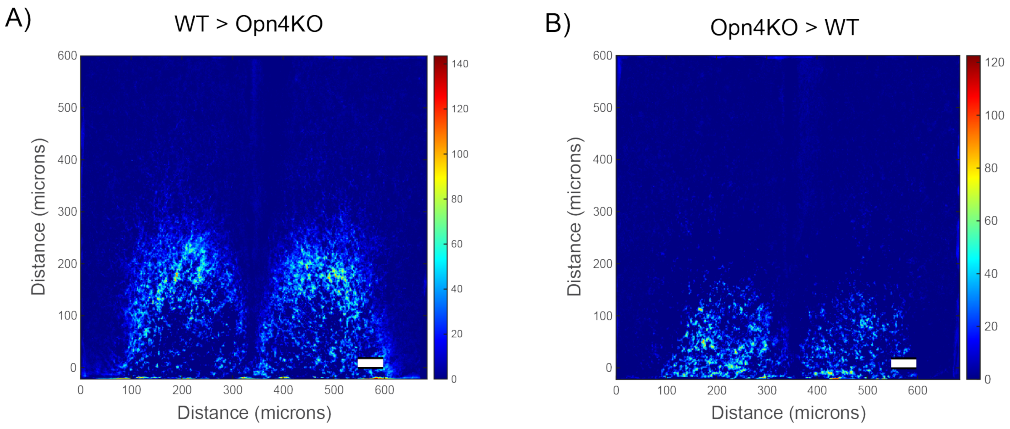

Figure 2.7: Two-dimensional intensity analyses reveal that P8 $Opn4^{Cre/Cre}$ mice exhibit ventrally clustered ipRGC innervation within the SCN. (A) In the WT > Opn4KO heat map, warm red-yellow regions represent pixels where WT intensity exceeds that of Opn4KO mice. (B) In the Opn4KO > WT heat map, warm red-yellow colors represent pixels where *Opn*4 KO intensity exceeds that of WT mice. Scale bar 50µm.

The analysis revealed a maximum positive difference of 143.6 intensity units (WT > KO) and a maximum negative difference of 122.6 intensity units (KO > WT), with a mean absolute difference of 7.76 intensity units across the SCN. Regions where WT signal exceeded KO are shown in red, while regions with greater KO intensity appear in blue; white areas indicate no significant difference after correction. All statistical comparisons were performed on spatially aligned data to minimize potential artifacts arising from registration errors (Fig.2.8B).

To investigate the contribution of each eye to the abnormal development of ipRGC innervation in the SCN of P8 *Opn4*-KO mice, I performed the same fluorescence intensity analysis separately for each eye. In both P8 *Opn4*-KO and wild-type mice, ipRGC axons from each eye innervated the SCN bilaterally, following the same ascending pattern originating from the contralateral ventral SCN. In both groups, innervation density was strongest in the contralateral ventrolateral region of the SCN,

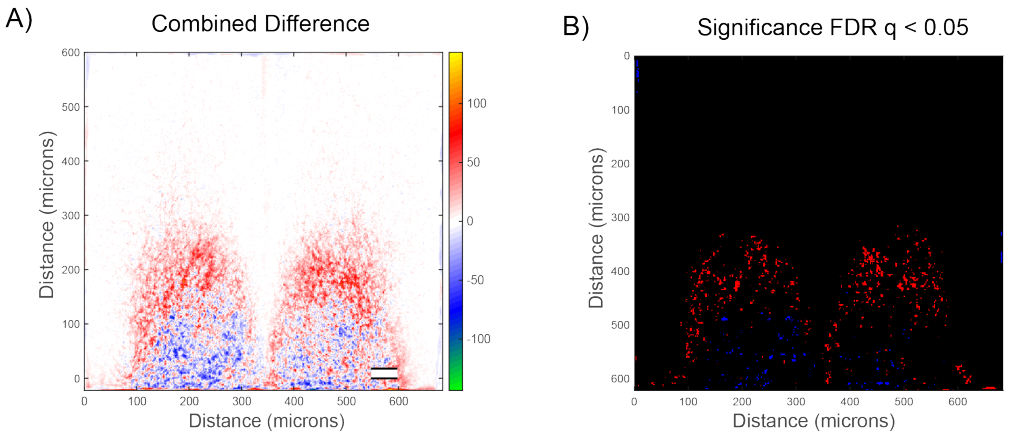

Figure 2.8: P8 *Opn4*-KO mice develop an abnormal ipRGC innervation pattern in the SCN. (A) Two-dimensional fluorescence intensity map of the SCN summarize the combined differences between *Opn4*-KO versus controls. Warm red-yellow regions represent pixels where WT intensity exceeds that of *Opn4*-KO, whereas cold blue-green regions represent pixels where *Opn4*-KO intensity exceeds that of WT. White regions indicate no difference between groups. Scale bar 50 μm. (B) The significance map (FDR $q < 0.05$) shows SCN regions with statistically significant intensity differences. Red regions = WT > *Opn4*-KO, blue regions = *Opn4*-KO > WT. Independent *t*-tests were performed across 2.0 x 2.0 μm regions ($p < 0.05$), followed by Benjamini-Hochberg false discovery rate (FDR) correction ($q < 0.05$).

as shown in the individual eye images (Fig.2.9). However, in P8 *Opn4*-KO, the overall pattern of ipRGC innervation appeared slightly asymmetrical, with higher density on the contralateral side of the SCN. This asymmetry was more apparent in the averaged composite images (Fig.2.9).

2.3.4 X-Dimensional Analyses of Single-Eye Fluorescence Intensity

Analyses of the average fluorescence intensity along the X-axis revealed that P8 *Opn4*-KO mice exhibited fluorescence intensities similar to wild-type mice on the contralateral side, but reduced intensities on the ipsilateral side of the SCN for each eye-specific input. For the left eye, mean fluorescence intensity was lower in *Opn4*-KO mice (39.57, 95% CI = 15.06) compared with wild-type mice (54.66,

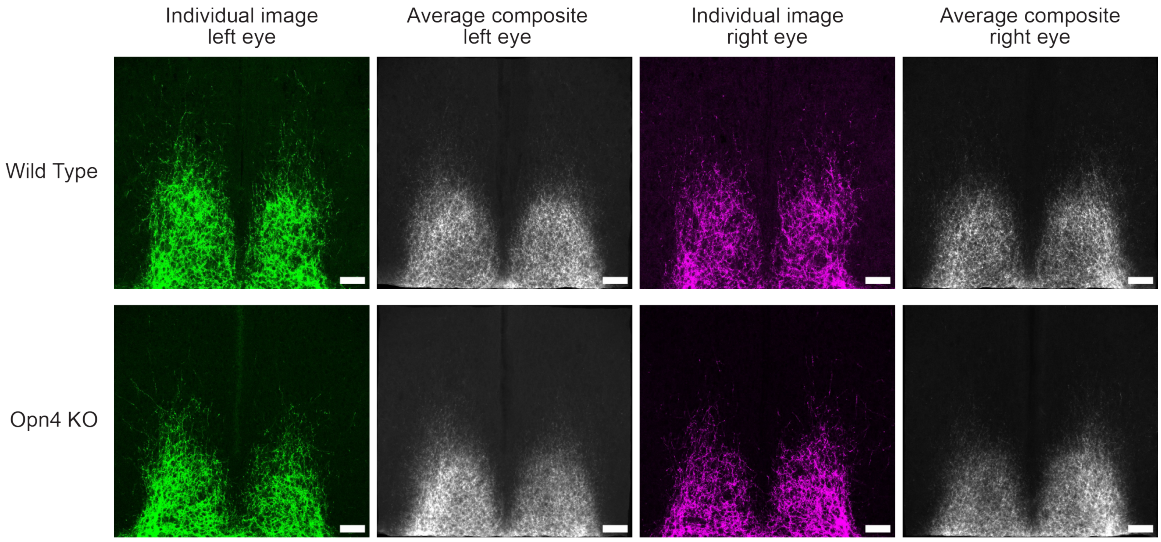

Figure 2.9: Comparison of single-eye ipRGC projections to the SCN. Representative single-plane coronal images of ipRGC axonal terminals in the SCN labeled with CTB-Alexa488 (left eye, green) and CTB-Alexa647 (right eye, magenta) in P8 wild-type mice (top images) and *Opn4*-KO mice (bottom images). *Opn4*-KO mice display an asymmetrical innervation pattern compared with controls. Scale bars = 100 µm.

95% CI = 14.57). Statistical comparisons showed significant differences between groups (Kolmogorov-Smirnov test = 0.1849, $p < 0.001$; Mann-Whitney U test, $p < 0.001$, *Opn4*-KO = 7 and WT = 5 mice). The effect size, measured by Cohens d, was 0.2754, indicating a small size effect. The achieved power to detect the X-axis differences was 0.712. For the right eye, fluorescence intensity was also slightly lower in *Opn4*-KO mice (25.24, 95% CI = 14.36) compared with wild-type controls (27.66, 95% CI = 11.66). Differences between groups were statistically significant (Kolmogorov-Smirnov test = 0.1356, $p < 0.001$; Mann-Whitney U test, $p < 0.001$, *Opn4*-KO = 7 and WT = 5 mice). Again, the effect size was small (Cohens d = 0.1822) and the experiment was underpowered (0.663) (Fig.2.10).

To investigate the spatial location of differences in single-eye innervations be-

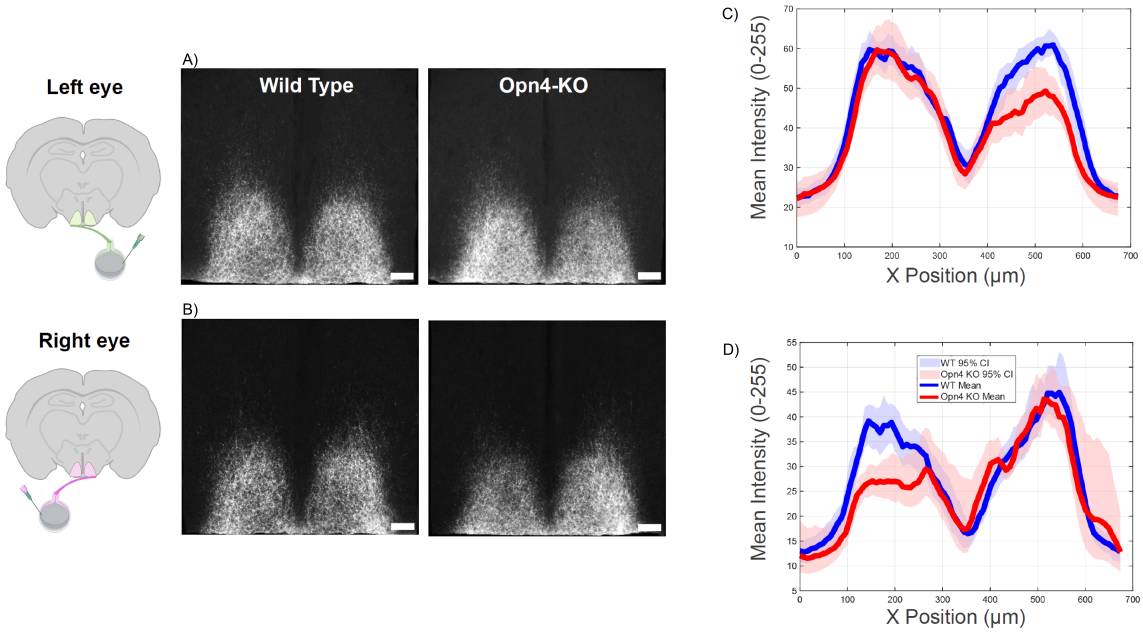

Figure 2.10: X-dimensional intensity analyses of single-eye projections reveal asymmetrical ipRGC innervation in *Opn4*-KO mice. Average composite images of left eye (A) and right eye (B) SCN innervation from each genotype after noise reduction and alignment, used for one-dimensional intensity analyses. Both genotypes show bilateral innervation, though distribution are asymmetrical. Scale bar 50 μm. Mean fluorescence intensity distributions along the horizontal (X-axis) dimension for left eye (C) and right eye (D) inputs separately in P8 wild type (blue) and *Opn4*-KO (red) and mice. Shaded regions represent bootstrap-derived 95% confidence intervals. Statistical comparisons between genotypes revealed significant differences. Kolmogorov-Smirnov test, $p < 0.001$; Mann-Whitney U test, $p < 0.001$. N = 7 *Opn4*-KO and 5 WT mice.

tween genotypes, I generated two-dimensional fluorescence intensity maps highlighting regions where one genotype shows stronger innervation than the other. P8 wild type mice developed ipPRGC innervation that extended across the entire contralateral SCN and sent axons ipsilaterally to the dorsomedial region of the SCN (WT > *Opn4*-KO Fig.2.11). In contrast, *Opn4*-KO mice developed ipRGC inputs that remained in the contralateral ventrolateral region of the SCN, with more sparse ipsilateral projections to the ventrolateral region of the SCN (*Opn4*-KO > WT Fig.2.11).

The combined difference maps (Fig.2.11) summarize these complementary patterns, revealing that wild-type mice show greater dorsomedial and ipsilateral SCN innervation, while *Opn4*-KO mice show relatively greater innervation restricted to the ventrolateral regions bilaterally.

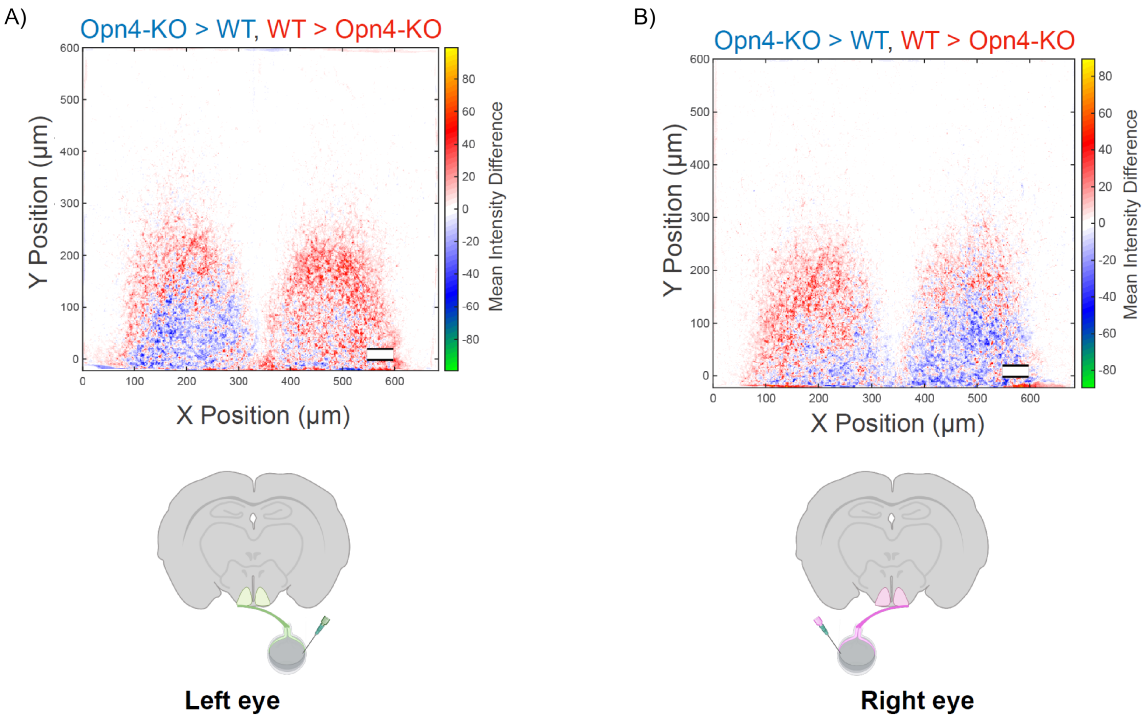

Figure 2.11: *Opn4*-KO mice develop abnormal bilateral ipRGC innervation patterns in the SCN. Two-dimensional fluorescence intensity maps of the SCN summarize the combined differences between *Opn4*-KO versus controls for the left (A) and right (B) eyes. Warm red-yellow regions represent pixels where WT intensity exceeds that of *Opn4*-KO, whereas cold blue-green regions represent pixels where *Opn4*-KO intensity exceeds that of WT. White regions indicate no difference between groups. *Opn4*-KO mice display an asymmetrical innervation pattern compared with controls. Scale bar 50 µm

Using the same statistical approach as the bilateral analysis, I quantified the magnitude of single-eye innervation differences between genotypes. For the left eye, the maximum positive difference was 99.36 intensity units (regions where WT > *Opn4*-KO) and the maximum negative difference was 87.50 intensity units (regions

where *Opn4*-KO > WT), with a mean absolute difference of 4.32 intensity units across the SCN. For the right eye, the maximum positive difference was 89.40 intensity units (WT > *Opn4*-KO) and the maximum negative difference was 73.89 intensity units (*Opn4*-KO > WT), with a mean absolute difference of 3.62 intensity units (Fig.2.12). These findings indicate that melanopsin loss produces spatially heterogeneous effects on SCN innervation, with some regions showing reduced innervation and others showing relatively preserved or compensatory innervation patterns.

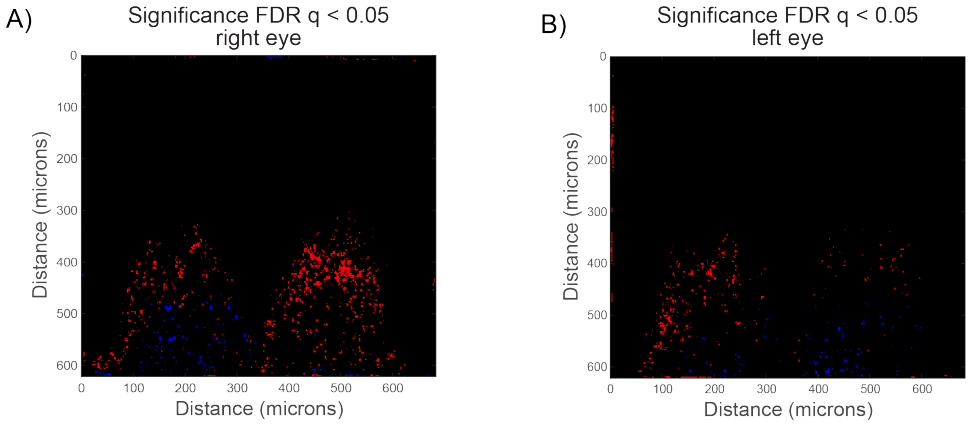

Figure 2.12: *Opn4*-KO mice develop asymmetrical single-eye ipRGC innervation patterns in the SCN. Statistical significance maps showing regions with significant intensity differences between genotypes for left eye and right eye projections separately. Red regions indicate where WT innervation exceeds *Opn4*-KO (WT > *Opn4*-KO), primarily in dorsomedial areas. Blue regions indicate where *Opn4*-KO innervation exceeds WT (*Opn4*-KO > WT), primarily in ventrolateral areas. Statistical analysis used independent t-tests across 33-pixel regions ($\sim$22 µm), with significance determined by Benjamini-Hochberg false discovery rate correction (FDR $q < 0.05$). Scale bar = 50 µm.

2.3.5 Lack of Melanopsin Impairs Eye-Specific Segregation in the dLGN

To investigate the impact of melanopsin on the development of the eye-specific segregation in the dLGN, I analyzed bilateral fluorescence patterns of RGC projections in P8 *Opn4*-KO and wild-type mice using the same CTB intraocular injection strategy described above (Fig.2.4).

2.3.5.1 Quantification of Eye-Specific Segregation

I employed a threshold-independent approach to quantify the degree of segregation based on [99, 100]. This approach calculates the logarithmic ratio of fluorescence intensity from ipsilateral-projecting axons to contralateral-projecting axons for each pixel within a region of interest: $R = Log_{10}(F_I/F_C)$. Higher variance in the R-distribution indicates better segregation, while lower variance indicates greater overlap of ipsilateral and contralateral projections.

I selected coronal brain slices containing the anterior region of the dLGN, between Bregma -2.18 and -2.30 mm. For each animal, two 60µm-thick sections were analyzed, corresponding to the rostral dLGN where ipsilateral and contralateral retinogeniculate projections show maximal segregation in wild-type mice (Fig.2.13).

The R-distribution plots for P8 *Opn4*-KO and wild type mice showed largely overlapping distributions centered near zero, indicating similar overall proportions of ipsilateral and contralateral input. However, closer examination revealed a sub-

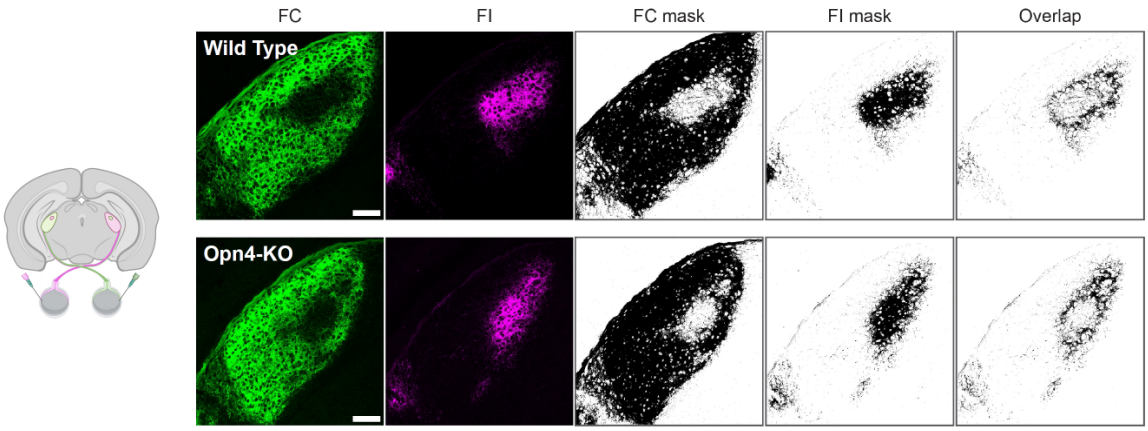

Figure 2.13: Comparison of eye-specific segregation in the dLGN between P8 *Opn4*-KO and wild-type mice. Representative confocal images of coronal dLGN sections showing the analysis pipeline for quantifying eye-specific segregation. (FC, FI) Raw fluorescence images showing RGC axonal projections from the contralateral eye (green, CTB-Alexa 488) and ipsilateral eye (magenta, CTB-Alexa 647). (FC mask, FI mask) Binary masks of contralateral (FC) and ipsilateral (FI) projections after thresholding and background subtraction. (Overlap) Overlap map showing regions with colocalized contralateral and ipsilateral projections (black). Wild-type mice show greater spatial separation of ipsilateral and contralateral territories compared to *Opn4*-KO mice. Scale bar = 100 μm.

tle but consistent difference: wild-type mice exhibited a broader distribution with more pixels at the distribution tail, suggesting greater segregation (Fig.2.14A). To quantify this difference, I calculated the variance of each logarithmic ratio distribution. Greater variance indicates a wider range of intensity ratios, with more pixels showing strong ipsilateral or contralateral dominance, and therefore reflects better eye-specific segregation. Using this metric, P8 WT mice showed significantly greater segregation variance than P8 *Opn4*-KO mice (Welchs t-test $t(28.96) = 3.029$, $^{**}p < 0.01$) (Fig.2.14B). This indicates that melanopsin loss results in subtle but significant impairment of eye-specific segregation in the developing dLGN.

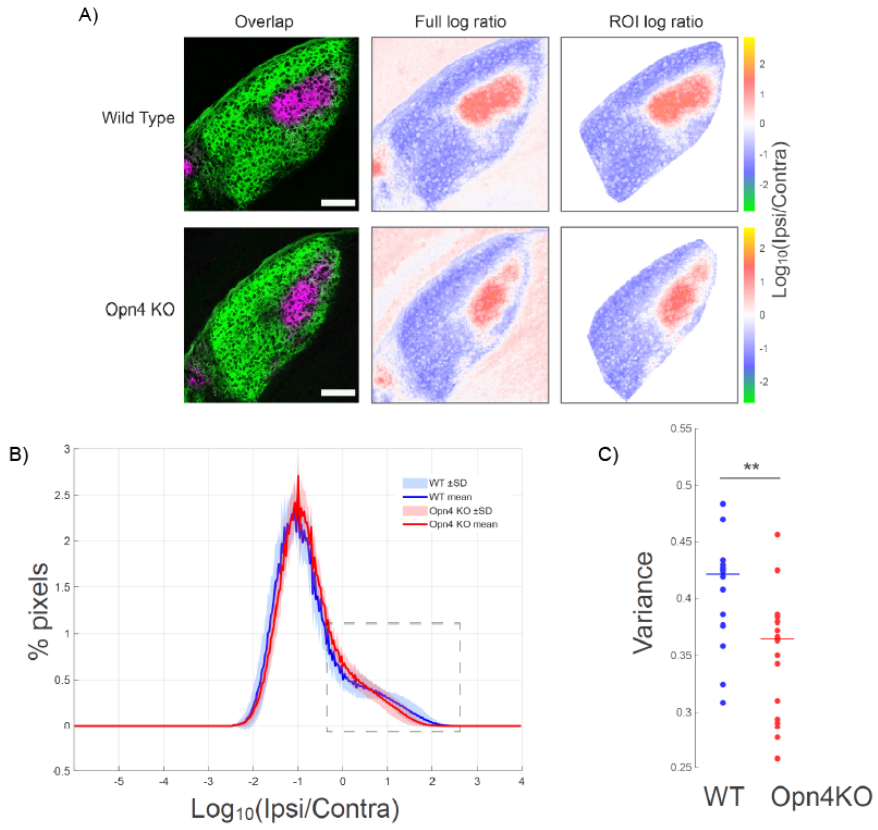

Figure 2.14: *Opn4*-KO mice show reduced eye-specific segregation in the dLGN. (A)(Overlap) Representative dual-color fluorescence overlays showing retinal projections from the contralateral eye (green, CTB-Alexa 488) and ipsilateral eye (magenta, CTB-Alexa 647) from P8 wild-type mice and *Opn4*-KO. (Full log ratio, ROI log ratio) Logarithmic ratio heat maps ($R = Log_{10}(F_{Ipsi}/F_{Contra})$) showing the degree of eye dominance for each pixel. Red indicates ipsilateral dominance (positive R), blue indicates contralateral dominance (negative R), and white indicates equal input ($R \approx 0$). Wild-type mice display a broader range of R values with more distinct eye-dominant regions, while *Opn4*-KO mice show more intermediate values, reflecting reduced segregation. Scale bar = 100 µm. (B) Distribution of logarithmic intensity ratios for all pixels within the dLGN. Positive R values represent pixels with greater ipsilateral fluorescence; negative values represent greater contralateral fluorescence. The distribution for wild-type mice (blue) is broader than that of *Opn4*-KO mice (red), indicating better segregation. Inset highlights the difference in distribution width. (C) Quantification of segregation using variance of the Log_{10} ratio distributions. Wild-type mice show significantly greater variance than *Opn4*-KO mice, indicating better eye-specific segregation (Welch's unpaired *t*-test: $t(28.96) = 3.029$, $^{**}p < 0.01$; n = 17 WT and 16 *Opn4*-KO mice). Error bars represent standard error of the mean.

2.4 Discussion

2.4.1 Melanopsin Regulates ipRGC Projection Development to the SCN

The results of this chapter demonstrate that melanopsin is required for the proper development of ipRGC projections to the SCN in mice. In melanopsin knockout animals, retinal projections to the SCN were reduced in density and abnormally distributed within the nucleus (Fig.2.6 and Fig.2.8). Rather than exhibiting the dorsomedial expansion observed in wild-type mice, melanopsin-deficient projections remained clustered predominantly in the ventrolateral region of the SCN.

Only two studies report normal innervation patterns in $Opn4^{/}$ mice [37, 63]. The first study uses melanopsin knockout mice in which the melanopsin gene is replaced by a tau-LacZ coding sequence in both alelles ($Opn4^{tauLacZ/tauLacZ}$), labeling all ipRGCs [63]. The authors demonstrate that in melanopsin knockout mice, ipRGCs are present, and still innervate the OPN and SCN (shown by X-Gal staining) despite losing their intrinsinc photosensitivity [63]. The second study used triple-knockout mice lacking melanopsin ($Opn4^{/}$), rods [guanine nucleotide-binding proten -transducin 1 ($Gnat1^{/}$)], and cones [cyclid GMP-gated channel A-subunit 3 ($Cnga3^{/}$)] [37]. These mutant mice have impaired pupillary light reflex, impaired circadian entrainment, and absence of any masking responses to light. Despite these deficits, these mice have normal retinal morphology and normal innervation to the SCN, IGL and OPN [37].

In contrast, my results show reduced retinal innervation of the SCN in postnatal day 8 *Opn4*-KO mice (Fig. 2.6). This discrepancy might be due to differences in developmental stage: my experiments use P8 mice, while Lucas et al. [63] and Hattar et al. [37] used 1 to 2 month old mice. Importantly, neither stuy performed detailed quantitative analysis of projection density or spatial distribution within SCN. In my experiments, individual images of wild type and *Opn4*-KO retinal projections to the SCN appear qualitatively similar. The difference between them was only confirmed after quantification using one-dimensional analysis along the X-axis (Fig. 2.6).

My results agree with earlier reports showing that the absence of early light stimulation through ipRGCs impairs neuronal differentiation and decreases neural circuit maturation [47, 54, 86]. The decreased ipRGC innervation of the SCN in *Opn4*-KO mice could be due to a decrease in the glutamatergic drive from ipRGCs due to the absence of melanopsin. Consistent with this interpretation, mice reared in constant darkness show smaller excitatory postsynaptic currents (EPSCs) in SCN neurons when the RHT is stimulated [86]. Moreover, lack of melanopsin also reduces the number of dendritic spines in hippocampal neurons [47], disturbing the development of excitatory circuits. When light-dependent activity is suppressed, as in melanopsin deficiency or dark rearing, neurons do not generate the calcium increments that normally regulate actin remodeling and SNARE-mediated exocytosis [55]. Without this light-dependent activity, axon growth is unstable, branching is reduced and fewer synaptic boutons are formed. My results provide direct evidence that melanopsin activity contributes to retinohypothalamic projection de-

velopment. Nonetheless, independent confirmation of these findings in melanopsin knockout mice from other laboratories would strengthen these conclusions.

2.4.2 Bilateral Innervation and the Role of Melanopsin

The SCN is unique among visual targets in receiving bilateral innervation from single RGC axons. Individual retinal axons elaborate complex bilateral projections throughout the entire SCN, with retinal terminals occupying contralateral and ipsilateral regions in approximately a 6:4 ratio [25]. This means that more than half of contralateral retinal projections send collateral branches across the midline to innervate the ipsilateral SCN [25].

The asymmetry observed in my single-eye analyses suggests that melanopsin may regulate the balance between contralateral and ipsilateral projections (Figs. 2.10 and 2.12). Importantly, both sides of the SCN remain innervated in the absence of melanopsin, indicating that other molecular signals guide axon terminals to the SCN. Rather than controlling initial targeting, melanopsin appears to regulate axonal growth and stabilization once axons have reached their target. The mechanism behind this regulation may involve calcium and cAMP signaling mediated by PACAP [30], both of which enhance axon guidance and synaptic refinement. Thus, lack of melanopsin could impair SCN innervation by reducing PACAP release from ipRGC terminals.

2.4.3 Interpreting the Magnitude of Effects

These effects of melanopsin loss on retinal projections to SCN were relatively small. The overall area covered by the retinal projections was not severely reduced in melanopsin knockout mice, and Cohens d effect sizes were small ($\sim$0.25). Several explanations could account for this modest phenotype. First, compensatory mechanisms may be at play. At the time I did the experiments, P8, rods are cone photoreceptors have begun to mature and may provide some functional compensation. Photoreceptors become electrically functional and photoresponsive prior to eye opening [6, 97]. Additionally, mice were exposed to light during eye injections and perfusions, potentially activating these developing photoreceptors and partially compensating for melanopsin loss. Second, melanopsin may play only a minor modulatory role in SCN projection refinement, with other guidance cues providing the primary signals. However, the consistent ventrolateral clustering of retinal projections across multiple mice suggests a reproducible developmental phenotype rather than experimental variability.

Interestingly, the absence of melanopsin resulted in ventral clustering rather than a gross loss of projections. This result could reflect a developmental delay rather than a permanent deficit, as it is the case in other sensory systems when early activity is reduced [50, 51, 71, 88]. Future experiments examining multiple developmental time points could clarify whether dorsomedial expansion eventually occurs in melanopsin knockout mice or whether the phenotype persists into adulthood.

2.4.4 Potential Mechanisms of Melanopsin-Mediated Segregation

The second major finding of this chapter is that melanopsin plays a role in eye-specific segregation in the dLGN. Segregation in melanopsin knockout mice was significantly reduced (Fig. 2.14), with projections from both eyes showing greater overlap than in wild-type controls. This demonstrates that melanopsin-dependent activity is necessary for the normal refinement of eye-specific territories.

These findings are consistent with previous work showing that early ipRGC activity modulates the temporal pattern of retinal waves that drive eye-specific segregation [85]. They also agreed with the finding that light exposure is necessary for normal segregation [99], and that ipRGCs are required for segregation to occur [12]. My data integrate these results by providing direct evidence that absence of melanopsin signaling alone is sufficient to impair structural plasticity in the dLGN. This corroborates that melanopsin is involved in both spontaneous and light-evoked activity processes required for segregation.

2.4.5 Potential Mechanisms of Melanopsin-Mediated Segregation

How might melanopsin signaling modulate eye-specific segregation? Several non-mutually exclusive mechanisms are possible. First, in newborns, light-evoked responses could synchronize retinal wave timing across the retina, enhancing correlated activity within each eye and thus facilitating synaptic strengthening of eye-specific connections. Second, light-evoked release of PACAP and glutamate from ipRGC terminals may regulate relay neurons directly, triggering synaptic pruning and territory

separation through cAMP- and calcium-dependent mechanisms. Third, melanopsin-evoked activity could modulate the presynaptic retinal terminal compartment rather than the postsynaptic dLGN neurons, influencing neurotransmitter release dynamics or axonal stability. Fourth, melanopsin-evoked activity could act in the retina itself, regulating retinal waves directly or indirectly through modulation of dopamine release from amacrine cells. Fifth, there may be unknown melanopsin-dependent mechanisms that promote segregation through novel signaling pathways yet to be discovered.

2.4.6 Methodological Considerations

Regarding methodological limitations, I used single-plane confocal imaging and mesoscale analysis, which do not capture the complete three-dimensional structure of the SCN or dLGN. Three-dimensional reconstructions have been made to study other visual nuclei [99] and could provide more comprehensive anatomical information.

Slice selection also introduces potential variability. Despite careful screening, it is possible that the sections analyzed may not be perfectly representative of the entire nucleus due to slight variations in slice positioning. Additionally, while cryosections were intended to be cut symmetrically in the coronal plane, achieving perfect reproducibility across animals is challenging. Slight asymmetries in sectioning angle could potentially bias one hemisphere over the other, affecting bilateral innervation measurements.

However, several factors support the validity of my findings. The consistency of results across multiple animals from both genotypes suggests that the observed phenotypes are robust and reproducible rather than artifacts of sample preparation. Furthermore, I analyzed multiple sections per animal and employed rigorous statistical methods including image registration and alignment to minimize the impact of anatomical variability. The significant differences detected between wild-type and melanopsin knockout mice, despite this inherent biological and technical variability, strengthen confidence in the conclusions.

2.4.7 Broader Implications and Conclusions

Together, these results demonstrate that melanopsin-mediated phototransduction is critical for organizing early ipRGC projections to both non-image-forming (SCN) and image-forming (dLGN) visual brain areas. The novelty of this work lies in showing that melanopsin, classically viewed as a photopigment for circadian photoentrainment, also functions as a developmental regulator shaping neural circuit architecture. By combining anatomical tracing with quantitative image analysis during a pre-photoreceptor developmental stage, this study bridges the gap between molecular phototransduction and structural circuit maturation.

In conclusion, I have found that melanopsin regulates the growth and spatial organization of ipRGC axons in the SCN and contributes to eye-specific segregation of retinogeniculate projections in the dLGN. These findings highlight a previously unrecognized developmental role for melanopsin-dependent signaling in establishing

the architecture of both circadian and visual pathways. Understanding this early light-driven modulation is important because it reveals how environmental light can sculpt brain connectivity before conventional vision begins, offering insight into how disruptions of perinatal photic signaling might affect later visual and circadian function.

Chapter 3: Lack of PACAP in ipRGCs Decreases ipRGC Innervation to the SCN, and Impairs Eye-Specific Segregation in the dLGN

3.1 Introduction

3.1.1 PACAP as a Co-transmitter in ipRGCs

ipRGCs not only release glutamate, the principal excitatory neurotransmitter, but also co-release pituitary adenylate cyclase-activating polypeptide (PACAP), a neuropeptide with modulatory and trophic functions [30]. PACAP from ipRGCs contributes to tuning of circadian photoentrainment, the pupillary light reflex, and visual adaptation under continuous illumination [1, 52]. PACAP belongs to the vasoactive intestinal peptide (VIP) / secretin / glucagon family and is present in two isoforms, PACAP38 and PACAP27. PACAP binds preferentially to the PACAP type 1 receptor (PAC1R), with lower affinity to VPAC1R and VPAC2R, all of which belong to the G-protein-coupled receptor (GPCR) family [66]. In general, binding of PACAP to PAC1R stimulates adenylate cyclase (AC), increases intracellular cAMP levels, and triggers downstream signaling pathways including protein kinase A (PKA) and phospholipase C (PLC) activation [14, 66]. These mechanisms al-

low PACAP to control key cellular processes such as motility, migration, secretion, proliferation, growth, survival, differentiation, and gene expression across various neural cell types and developmental stages.

3.1.2 PACAP in Brain Development

Beyond its role in ipRGC signaling, PACAP plays important roles throughout the nervous system in brain development, neural regulation, synaptic homeostasis and neuroprotection [94]. PACAP is widely expressed in the nervous system from early embryonic stages through adulthood [94, 108, 109]. PACAP regulates neural development by coordinating neuronal differentiation and regulating neuronal survival in both peripheral and central nervous systems. While PACAP and PAC1R are highly expressed during mouse embryonic development, PACAP knockout results in premature death of mouse pups [94]. Conversely, PACAP overactivation due to gain-of-function mutations in the PACAP signaling pathway increases cell death and brain malformations [94], highlighting the importance of tightly regulated PACAP signaling during development.

3.1.3 Developmental Stage-Specific Effects of PACAP

PACAP exerts diverse effects during different developmental stages because PAC1R comes in multiple isoforms that trigger distinct cellular signaling pathways, including cAMP / PKA and PLC / PKC signaling cascades, regulating gene expression, as well migration and motility, respectively [66] (Fig.3.1). In developing

spinal root ganglia, PACAP promotes neuronal differentiation through activation of the PAC1R-dependent mitogen-activated protein kinase (MAPK) signaling pathway. Blocking MAPK signaling disrupts normal neuronal differentiation even in the presence of exogenous PACAP stimulation [74], demonstrating that downstream signaling pathways are essential for PACAP's developmental effects. In the developing retina, PACAP-38 transiently increases division of horizontal cells and Müller glia during specific periods of retinal development [18]. This shows that different receptor variants can switch PACAPs function from inhibiting to promoting cell division depending on developmental stage. These results indicate that PACAP serves as a time-sensitive signal that regulates neuronal proliferation and differentiation in a context-dependent manner.

Functional research has shown that PACAP modulates light signaling in the SCN at both molecular and behavioral levels. Electrophysiological recordings reveal that PACAP enhances glutamatergic transmission through both presynaptic and postsynaptic mechanisms. PACAP increasing glutamate release and enhances ionotropic glutamate receptor currents through activation of PAC1R / AC / PKA / ERK signaling pathway [14, 68] (Fig.3.2). These PACAP-dependent synaptic changes amplify excitatory signaling, contributing to long-term potentiation that underlies circadian rhythm phase shifts. PACAP also interacts with NMDA receptors, facilitating calcium influx and activating transcription factors such as CREB. This promotes the expression of immediate early genes like $Per1$ and $Per2$ that are essential for light-induced entrainment [14, 74].

Behavioral studies corroborate these molecular findings. Mice lacking PAC1R

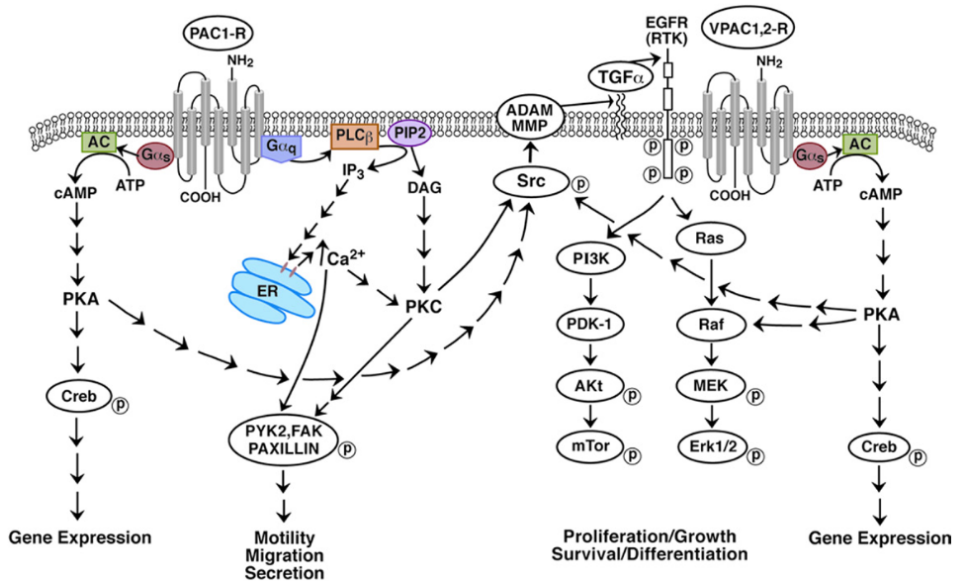

.

Figure 3.1: PACAP signaling pathways activating PAC1R and VPAC1R/VPAC2R. Activated PAC1 or VPAC1R/VPAC2R receptors triggers $G_{\alpha s}$-stimulating adenylyl cyclase (AC) / PKA activation / cAMP response element-binding protein (Creb) phosphorylation, resulting in gene expression. PKC activates MMP and/or ADAM, releasing TGF_{α} causing EGFR tyrosine phosphorylation. The phosphorylated EGFR activates Ras and Raf / phosphorylation of mitogen-activated protein kinase kinase (MEK) and Erk1/2, leading to proliferation. The phosphorylated EGFR phosphorilates phosphatidylinositol 3-kinase (PI3K) / activation of pyruvate dehydrogenase lipoamide kinase isozyme 1 (PDK-1) / Akt / mammalian target of rapamycin (mTor), leading to cellular survival. Activated PAC1 receptor also triggers with $G_{\alpha q}$ / phospholipase C (PLC) / PI turnover. The IP_3 / diacylglycerol (DAG) increase cytosolic Ca^{2+} / PKC activation, respectively. The PKC or Ca^{2+} causes Src tyrosine phosphorylation, leading to phosphorylation of focal adhesion kinase (FAK) / pyruvate kinase 2 (PYK2) / paxillin, affecting cellular motility, secretion and migration. The figure was modified from Moody and Jensen [70]

show reduced phase shifts of the endogenous rhythm at early night and weakened synchronization under dim lighting conditions [33]. These results confirm that PAC1R signaling amplifies light sensitivity for circadian entrainment.

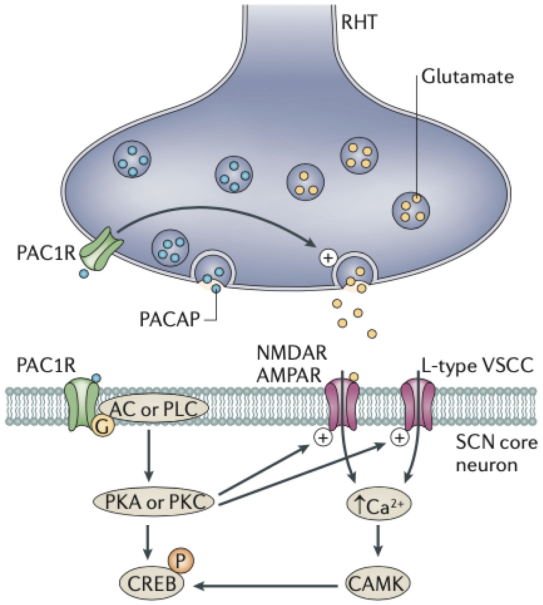

.

Figure 3.2: Synaptic localization of PACAP. PACAP presynaptically increases the release of glutamate, and postsynaptically strengthens AMPA and NMDA currents. The increase of Ca^{2+} activates different signaling pathways increasing cAMP and phosphorylating CREB, which is translocated to the nucleus to initiate transcription. The figure was modified from Colwell [14]

3.1.4 Complementary Roles of PACAP and Glutamate in ipRGC Signaling

PACAP and glutamate act in a complementary manner within ipRGC target regions, where the balance between their signaling determines the strength and duration of light-evoked responses. Studies show that when glutamatergic transmission from ipRGCs is disrupted, as in mice lacking vesicular glutamate transporter 2 (VGLUT2), PACAP signaling alone is insufficient to drive normal light responses but can partially sustain them [82, 106]. These findings demonstrate that glutamate initiates rapid signal transmission, while PACAP stabilizes and prolongs activity in

target neurons, maintaining responsiveness to continuous light. For instance, in the pupillary light reflex, PACAP is critical for the sustained phase of pupil constriction, ensuring that the reflex does not fade during long exposure to light [52]. Conversely, when PACAP is absent, glutamatergic signaling alone can trigger the initial photic response but fails to maintain or amplify postsynaptic excitatory activity over time. This is because PACAP normally enhances both presynaptic glutamate release and postsynaptic AMPA and NMDA receptor currents through the PAC1 / AC / PKA pathway [68, 106]. Together, these results indicate that while glutamate provides the primary excitatory drive, PACAP functions as a critical modulatory signal that fine-tunes and sustains glutamatergic transmission, ensuring stable light responses across different temporal phases of visual processing.

3.1.5 PACAP in the SCN: Modulating Circadian and Non-Image-Forming Functions

In the SCN, PACAP plays a critical modulatory function by enhancing glutamatergic signaling to regulate circadian and non-image-forming visual functions. PACAP cooperates with glutamate to amplify NMDA receptor activation and rhythmic ERK signaling, providing a mechanism for maintaining circadian oscillations even in constant darkness [106]. PACAP also increases both the firing rate and calcium influx in SCN neurons and activates cAMP signaling pathways [14].

PAC1R is expressed both presynaptically and postsynaptically in the SCN. Presynaptic PAC1R activation enhances glutamate release [14], while postsynaptic

PAC1R increases the magnitude of NMDA and AMPA currents [68]. More recently, PACAP was also found to mediate non-canonical visual pathways, such as the ipRGC / SCN / paraventricular thalamus circuit that transmits socially relevant visual signals like contagious itch, where it enhances glutamatergic transmission to gastrin-releasing peptide neurons [29].

These results suggest that PACAP acts as a versatile neuromodulator in the SCN, coupling photic and non-photic inputs through dynamic control of glutamatergic transmission to fine-tune circadian and behavioral responses.

3.1.6 PACAP in Image-Forming Visual Processing

ipRGCs also project to several image-forming visual processing nuclei including the dLGN and superior colliculus [4, 12, 34]. In mice, both ipRGCs and conventional RGCs project to overlapping regions in the dLGN, with ipRGC axon terminals clustering along the medial border, suggesting that ipRGCs are integrated into image-forming visual processing [4]. Moreover, in primates, PACAP-positive nerve fibers are found in the dLGN and have been linked to the processing of visual sensitivity and brightness perception [34]. PACAP-containing ipRGC projections to the dLGN contribute to early visual processing by modulating excitatory and inhibitory balance, which could be relevant during the maturation of retinogeniculate connections [1].

However, while ipRGC projections have been anatomically described, their development and maturation have not been extensively determined. It is still un-

clear whether PACAP regulates eye-specific segregation in the dLGN or synaptic plasticity within the dLGN during development.

3.1.7 PACAP in Retinal Development and Function

In the retina, PACAP and PAC1R are widely expressed and regulate neuronal differentiation, signaling, and neuroprotection. PAC1R has been detected in the somas and dendrites of amacrine and retinal ganglion cells, but not in photoreceptors [73]. In developing chick retina, PACAP promotes the differentiation of dopaminergic neurons through PAC1R-dependent cAMP / PKA signaling, serving as an endogenous signal that drives tyrosine hydroxylase expression during early development [7]. In mammals, PACAP and PAC1 are broadly expressed in retinal neurons and glial cells, where they activate cAMP, MAPK / ERK, and PI3K / Akt pathways to protect against hypoxia, oxidative stress, and neurodegeneration [57, 73]. Conversely, the absence of PACAP accelerates age-related decline and increases retinal cell death, emphasizing its neuroprotective importance [57].

Functionally, ipRGCs provide excitatory input to dopaminergic amacrine cells through reciprocal synapses [83], and some ipRGCs extend axon collaterals into the inner plexiform layer, potentially contributing to dopamine release that modulates gap junction coupling [60, 80]. Together, these observations suggest that PACAP not only contributes to retinal development and neuroprotection but may also influence spontaneous retinal waves by modulating dopaminergic signaling and intercellular coupling during early visual circuit formation.

3.1.8 PACAP Regulates Synaptic Development and Plasticity

PACAP functions as a key regulator of neuronal growth, synaptic development, and plasticity by coordinating multiple signaling pathways that shape neural connectivity. In primary hippocampal neurons, PACAP promotes neurite and axonal outgrowth through the interaction between PAC1R and Tropomyosin receptor kinase B (TrkB) receptors, mimicking the neurotrophic effects of BDNF [76]. PACAP enhances dendritic spine maturation and increases the number of excitatory synapses through ERK-dependent upregulation of miR-132, which suppresses p250GAP and supports synaptic connectivity independently of PKA or PKC signaling [39]. PACAP also activates PLC / PKC / tyrosine kinase signaling pathways, enhancing NMDAR function that facilitates long-term potentiation (LTP) [64]. In contrast, in the dentate gyrus, PACAP deficiency leads to abnormal axonal arborization, reduced dendritic spine number, and impaired LTP, underscoring its essential role in maintaining synaptic integrity and NMDA receptor regulation [39, 66, 107]. Moreover, PACAP signaling regulates NMDA receptor activity to induce BDNF expression and other immediate early genes through the calcineurin-dependent CRTC1 / CREB pathway, reinforcing its role in long-term neuronal growth and survival [28]. These findings highlight PACAP as an important neurotrophic modulator that integrates receptor-mediated and transcriptional mechanisms to promote structural plasticity. Similarly, PACAP-dependent mechanisms could promote structural plasticity in developing visual systems.

3.1.9 PACAP Regulates Excitatory and Inhibitory Balance

PACAP is co-expressed in glutamatergic neurons, enhancing excitatory signaling by increasing VGLUT1 and VGLUT2 expression [22, 109]. PACAP also increases neuronal excitability by acting through PAC1R to elevate cAMP and activate intracellular signaling cascades [109]. Conversely, PACAP modulates glutamate metabolism in astrocytes by inducing expression of the glutamate transporters GLT-1 and GLAST, as well as glutamine synthetase [26]. Interestingly, PACAP is also coexpressed in GABAergic neurons, where it increases inhibitory tone by modulating vesicular GABA transporter (VGAT) expression [108]. The co-expression of PACAP in both excitatory and inhibitory neurons suggests that PACAP may contribute to homeostatic regulation of excitation and inhibition in developing neuronal circuits [108]. Such control of connection structure and transmitter balance provides plausible cellular mechanisms through which PACAP could influence retinal projection development and refinement in brain visual regions.

Despite extensive evidence linking PACAP to neural differentiation, synapse formation and maturation, and modulation of light signaling, major questions remain about whether PACAP regulates the growth or organization of ipRGC axons projecting to the SCN, and whether PACAP play a role eye-specific segregation in the dLGN. To address these questions, I used tract tracing with eye injections and mesoscale imaging to assess ipRGC projections to the SCN and dLGN in juvenile conditional ipRGC-specific PACAP knockout mice.

3.2 Methods

All experimental procedures were performed as described in 2.2 (Chapter 2, Methods), exception that ipRGC-specific conditional PACAP knockout mice were used instead of melanopsin knockout mice. PACAP-cKO mice were generated by crossing *Adcyap1*$^{fl/fl}$ mice (*Adcyap1*, MGI: 105094), in which two *loxP* sites flank exon 2 of the PACAP (*Adcyap1*) locus [87], with *Opn4*$^{Cre/Cre}$ mice expressing Cre recombinase selectively in ipRGCs [21]. The resulting conditional ipRGC-specific PACAP (*Opn4*$^{Cre/+}$/*Adcyap1*$^{fl/fl}$) knockout mice (hereafter designated as PACAP-cKO) developed with no apparent gross behavioral abnormalities. Genotyping was performed by Transnetyx using real-time PCR.

3.3 Results

3.3.1 PACAP is Dispensable for ipRGC Axon Targeting to the SCN

To investigate whether PACAP plays a role in the development of retinal projections to the SCN, I analyzed the fluorescence intensity of bilateral retinal projections to the SCN using single-plane confocal imaging of coronal sections from P8 PACAP-cKO (N = 8) and wild-type mice (N = 5). Mice received intraocular injections of CTB-Alexa488 in the left eye and CTB-Alexa647 in the right eye at P7, and brains were collected at P8 (Fig: 3.3).

Visual inspection of fluorescence images from both eyes revealed that PACAP-cKO mice developed retinal projections to the SCN that appeared qualitatively

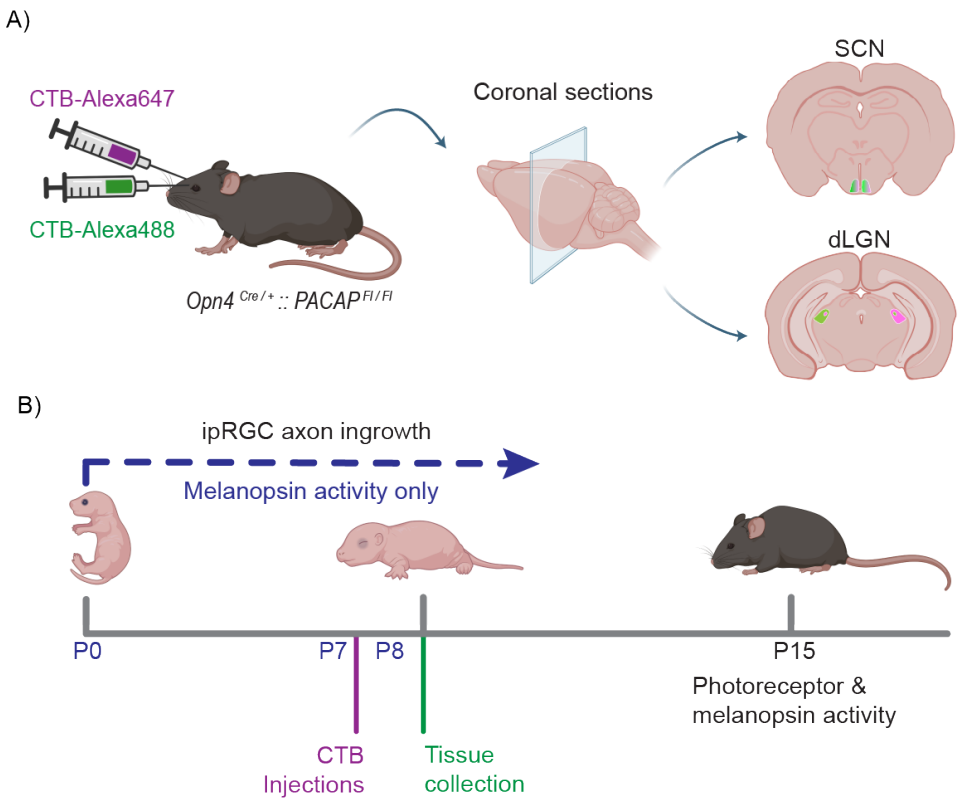

Figure 3.3: Experimental design to study axonal projections to SCN and dLGN of PACAP-lacking ipRGCs. (A) Schematic of the experimental approach used to trace retinofugal projections to the SCN and dLGN in conditional ipRGC-specific PACAP knockout mice. Anterograde tracing was performed by intraocular injection of cholera toxin subunit B (CTB) conjugated to either Alexa Fluor 488 or Alexa Fluor 647. (B) Experimental timeline and design used in this study. CTB injections were performed at P7, and brains were dissected at P8, prior to photoreceptor maturation when the eyes are still closed and photoreceptors remain functionally immature.

normal. The density of retinal projections was uniformly higher in the ventrolateral regions of the SCN, where axons first reach the nucleus from the optic chiasm. Both genotypes showed symmetrical coverage of ipsilateral regions (Fig 3.4), (A): both eyes). Similarly, examination of fluorescence from individual eyes showed uniform projections in both left and right eye projections (Fig 3.4), (B): left eyes; (C): right eyes).

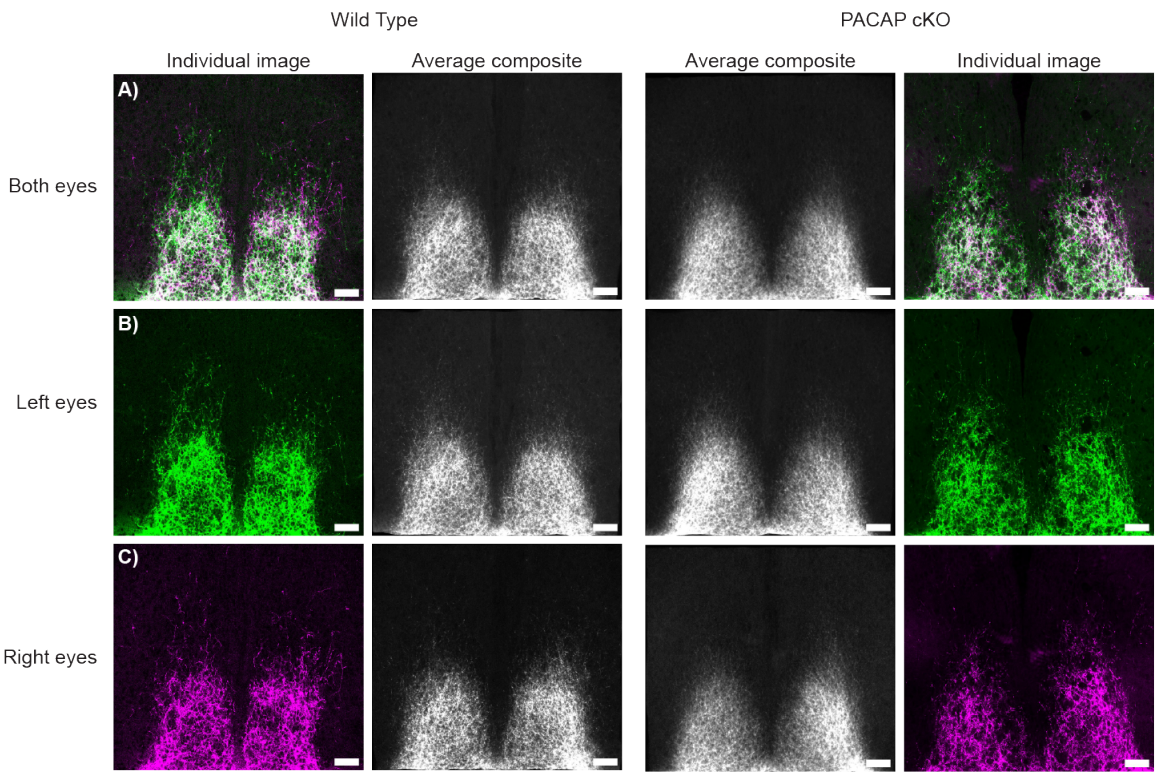

Figure 3.4: Comparison of SCN projections in PACAP-cKO mice. Representative coronal single-plane images show bilateral (A) and unilateral retinal projections from left (B) and right (C) eyes labeled with CTB in P8 conditional ipRGC-specific PACAP-cKO and wild-type mice (n = 8 and n = 5, respectively). Scale bar = 100 µm.

3.3.2 One-Dimensional Analysis of Bilateral Projections

To quantify potential differences in SCN innervation between genotypes, I performed one-dimensional analyses of fluorescence intensity from bilateral projections.

X-axis analysis of the average column fluorescence intensity revealed that the distribution shapes differed significantly between PACAP-cKO and wild-type mice (PACAP-cKO: mean = 13.01, 95% CI = 6.23; WT: mean = 12.76, 95% CI = 5.53; Kolmogorov-Smirnov test = 0.0716, $p < 0.01$). However, the central tendency of the

distributions was similar (Mann-Whitney U test, $p > 0.05$; n = 8 PACAP-cKO and 5 WT mice) (Fig 3.5, X-axis). The effect size was negligible (Cohen's d = −0.04), with achieved statistical power of 0.59.

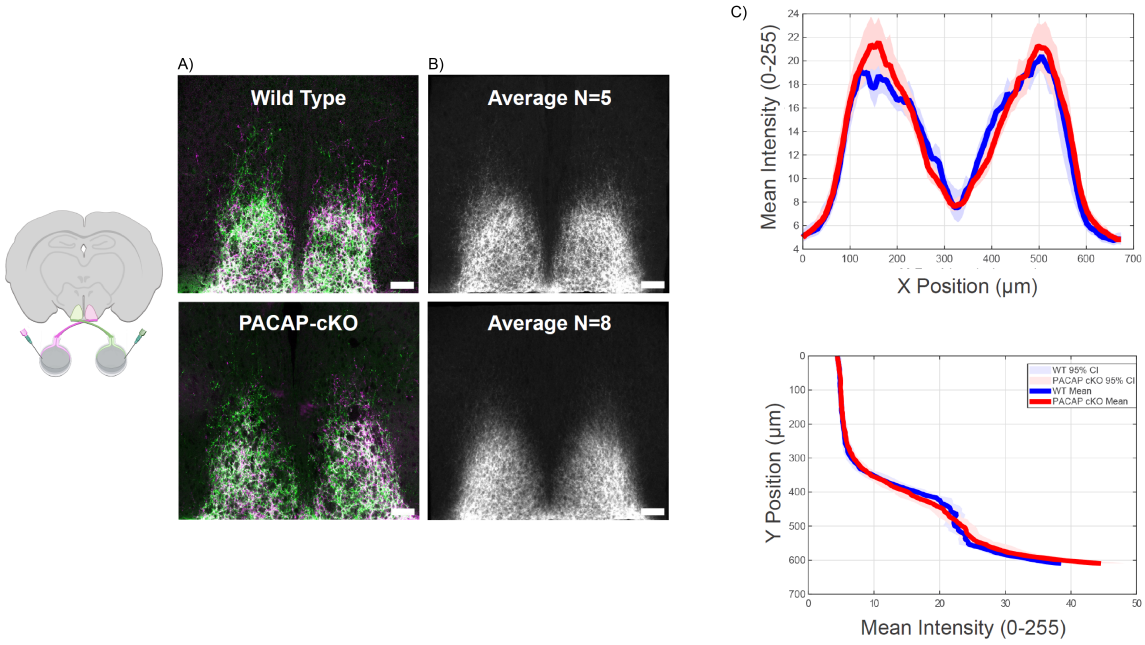

Figure 3.5: One-dimensional intensity analyses reveal that P8 PACAP-cKO mice exhibit similar ipRGC innervation in the SCN. (A) Representative single-plane coronal sections showing ipRGC axonal terminals labeled with CTB-Alexa 488 (green, left eye) and CTB-Alexa 647 (red, right eye) projecting bilaterally to the SCN in P8 wild-type and PACAP-cKO mice. (B) Average composite images of bilateral SCN innervation from each genotype after noise reduction and alignment, used for one-dimensional intensity analyses. Both genotypes show bilateral innervation, though distribution patterns differ. Scale bar 50 µm. (C) Mean fluorescence intensity distributions are plotted along the horizontal X axis and vertical Y axis for bilateral innervations in P8 PACAP-cKO (red) and wild-type (blue) mice. Shaded regions indicate bootstrap-derived 95% confidence intervals. Statistical comparisons between genotypes revealed significant differences along both axes. X-axis: Kolmogorov-Smirnov test = 0.0716, $p < 0.01$), with similar central tendency (MannWhitney U test, $p > 0.05$). The same result for the Y-axis: Kolmogorov-Smirnov test = 0.0740, $p < 0.01$; MannWhitney U test, $p > 0.050$ (PACAP-cKO N = 8 and WT N = 5 mice). Scale bar 50 µm.

Y-axis analysis of the average row fluorescence intensity also showed significantly different distributions between genotypes (PACAP-cKO: mean = 12.86, 95%

CI = 10.40; WT: mean = 12.63, 95% CI = 9.51; Kolmogorov-Smirnov test = 0.0740, $p < 0.010$), but again with similar central tendency (Mann-Whitney U test, $p > 0.05$; n = 8 PACAP-cKO and 5 WT mice) (Fig 3.5, Y-axis). The effect size was negligible (Cohen's d = 0.02), with achieved statistical power of 0.58.

3.3.3 Two-Dimensional Analysis Reveals Altered Spatial Distribution of SCN Innervation

To investigate the spatial distribution of these differences, I generated two-dimensional fluorescence intensity maps of the SCN. While P8 wild-type mice developed ipPRGC innervation distributed throughout the entire SCN, with axonal density highest in the dorsomedial region, PACAP-cKO mice showed ipRGC innervation that concentrated primarily in the ventrolateral region of the SCN (Fig.3.6 PACAP-cKO mice). When comparing the spatial distribution of innervation between PACAP-cKO and *Opn4*-KO mice, PACAP-cKO projections extend into the dorsolateral region of the SCN, whereas *Opn4*-KO projections remain confined to the ventral region. Notably, PACAP-cKO axons do not innervate the medial portion of the nucleus, while *Opn4*-KO innervation is present in this area (Fig.3.6 *Opn4*-KO mice).

To compare the intensity maps between the groups, I ran independent t-tests comparing image intensities between PACAP-cKO and WT groups using rigidly aligned, mouse-averaged images. Each test compared mean fluorescence intensity across 33-pixel regions (2.0x2.0 μm), with significance determined by $p < 0.05$ and

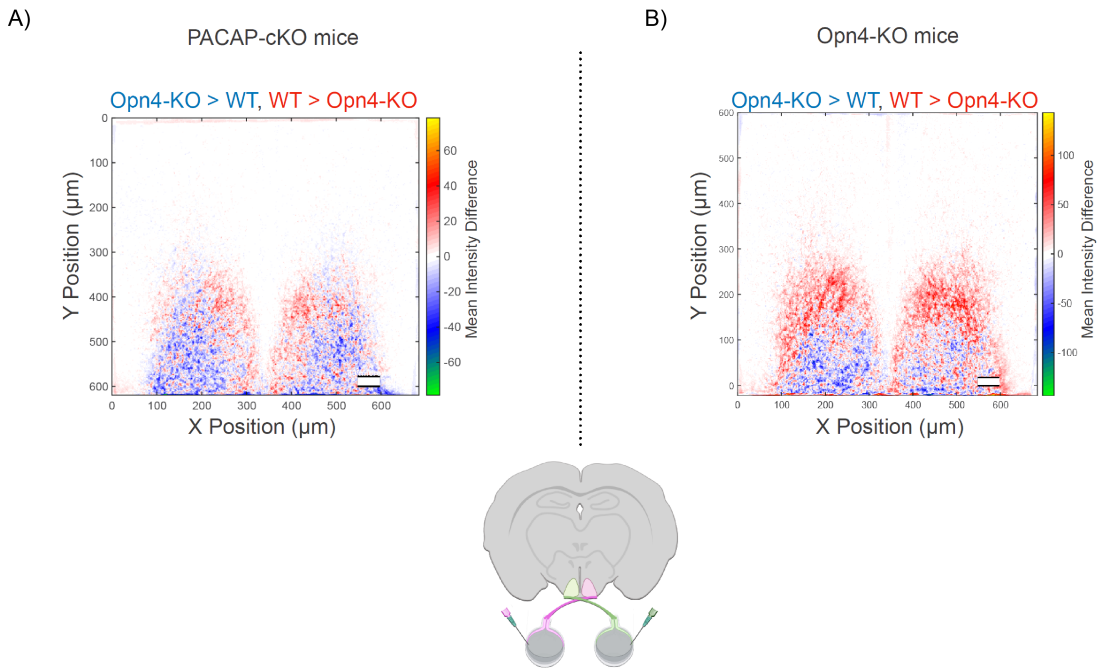

Figure 3.6: Two-dimensional heat map of SCN fluorescence intensity show ipRGC inputs clustering laterally in P8 PACAP-cKO. Map displays combined WT versus PACAP-cKO differences from both eyes. Warm colors (red-yellow): WT > PACAP-cKO; cool colors (blue-green): PACAP-cKO > WT; white: no difference. PACAP-cKO innervations patterns differ qualitatively from *Opn4*-KO mice. Scale bar 50 µm.

a minimum regional difference of 5 intensity units. Multiple comparisons were corrected using the Benjamini-Hochberg false discovery rate (FDR) procedure ($q < 0.05$).

The analysis revealed a maximum positive difference of 71.93 intensity units (WT > PACAP-cKO) and a maximum negative difference of 78.54 intensity units (PACAP-cKO > WT), with a mean absolute difference of 3.35 intensity units across the SCN. Regions where WT signal exceeded PACAP-cKO are shown in red, while regions with greater PACAP-cKO intensity appear in blue; white areas indicate no significant difference after correction. All statistical comparisons were performed on

spatially aligned data to minimize potential artifacts arising from registration errors (Fig.3.7).

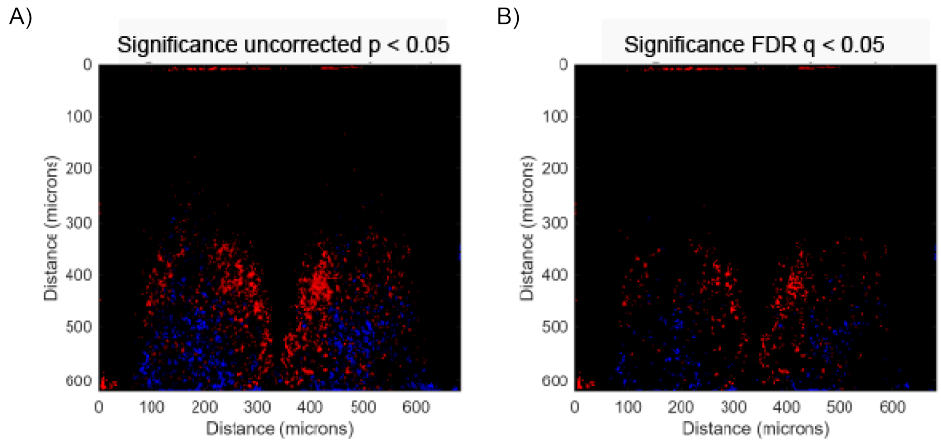

Figure 3.7: P8 PACAP-cKO mice develop abnormal ipRGC innervation pattern in the SCN. Significance maps show SCN regions with statistically different intensity between WT and PACAP-cKO mice, calculated using independent t-tests across 2.0x2.0 µm regions ($p < 0.05$). (A) Uncorrected $p < 0.05$. (B) Benjamini-Hochberg false discovery rate correction, $q < 0.05$. Red: WT > PACAP-cKO; blue: PACAP-cKO > WT.

3.3.4 One-dimensional analysis of single-eye fluorescence intensity

To assess symmetry of individual eye projections, I performed X-axis analyses of fluorescence intensity from left and right eyes separately.

Analyses of the average fluorescence intensity along the X-axis revealed that P8 PACAP-cKO mice showed an asymmetrical distribution compared to the more symmetrical pattern in wild-type mice. For the left eye, mean fluorescence intensity was lower in PACAP-cKO mice (PACAP-cKO: mean = 33.55, 95% CI = 16.28) compared with wild type controls (WT: mean = 37.36, 95% CI = 14.71). Differences between groups were statistically significant (Kolmogorov-Smirnov test =

0.1496, $p < 0.001$; Mann-Whitney U test, $p < 0.05$; n = 8 PACAP-cKO and 5 WT mice) (Fig.3.8, (A) Left eye). The effect size was small (Cohen's d = 0.24), with achieved statistical power of 0.71. For the right eye, fluorescence intensity was also slightly lower in PACAP-cKO mice (34.59, 95% CI = 38.49) compared with wild-type controls (11.23, 95% CI = 17.82). Differences between groups were statistically significant (Kolmogorov-Smirnov test = 0.2315, $p < 0.05$; Mann-Whitney U test, $p < 0.05$, PACAP-cKO = 8 and WT = 5 mice) (Fig.3.8, (B) Right eye). The effect size was medium (Cohens d = -0.58) and the experiment was sufficiently powered (0.840).

To examine the spatial distribution and clustering of single-eye retinal projetions within the SCN, I generated two-dimensional fluorescence intensity maps highlighting regions where one genotype shows stronger innervation than the other. In these maps, regions where WT signal exceeded PACAP-cKO are shown in red, while those with greater PACAP-cKO intensity appear in blue. White areas indicate regions with no significant difference after correction. The intensity map of individual eyes shows that retinal axons in PACAP-cKO genotype predominantly terminated in the lateral region of the contralateral SCN, with a smaller projections crossing to the lateral portion of the ipsilateral SCN (Fig.3.9).

3.3.5 Lack of PACAP Impairs Eye-Specific Segregation in the dLGN

To investigate PACAP's role in eye-specific segregation in the dLGN, I analyzed bilateral RGC projections in P8 PACAP-cKO and wild-type mice using the

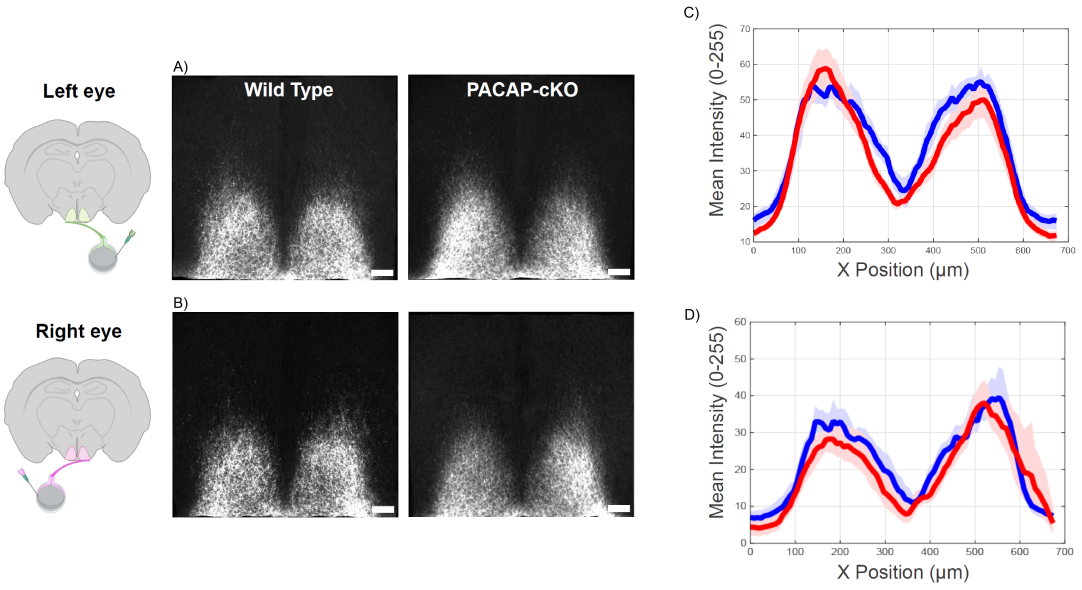

Figure 3.8: One-dimensional intensity analyses of single-eye projections reveals asymmetrical ipRGC innervation in PACAP-cKO mice. Average composite images of left eye (A) and right eye (B) SCN innervation from each genotype after noise reduction and alignment, used for one-dimensional intensity analyses. Both genotypes show bilateral innervation, though distribution are asymmetrical. Scale bar 50 μm. Mean fluorescence intensity distributions along the horizontal (X-axis) dimension for left eye (C) and right eye (D) inputs separately in P8 PACAP-cKO (red) and wild type (blue) mice. Shaded regions represent bootstrap-derived 95% confidence intervals. Statistical comparisons between genotypes revealed significant differences in both axes. Kolmogorov-Smirnov test, $p < 0.05$; Mann-Whitney U test, $p < 0.05$. N = 8 PACAP-cKO and 5 WT mice. Scale bar 50μm.

CTB intraocular injection strategy described above (Fig.3.3).

I quantifed segregation using a threshold-independent approach [99, 100], as described in 2.3.5.1 (Chapter 2, Quantification of Eye-Specific Segregation), comparing conditional ipRGC-specific PACAP knockout mice to wild-type controls.

I selected two 60 μm coronal sections per animal from the anterior dLGN, (Bregma −2.18 and −2.30 mm), corresponding to the rostral region where ipsilateral and contralateral projections show maximal segregation in wild-type mice (Fig.3.10). R-distribution plots showed similar overall proportions of ipsilateral and

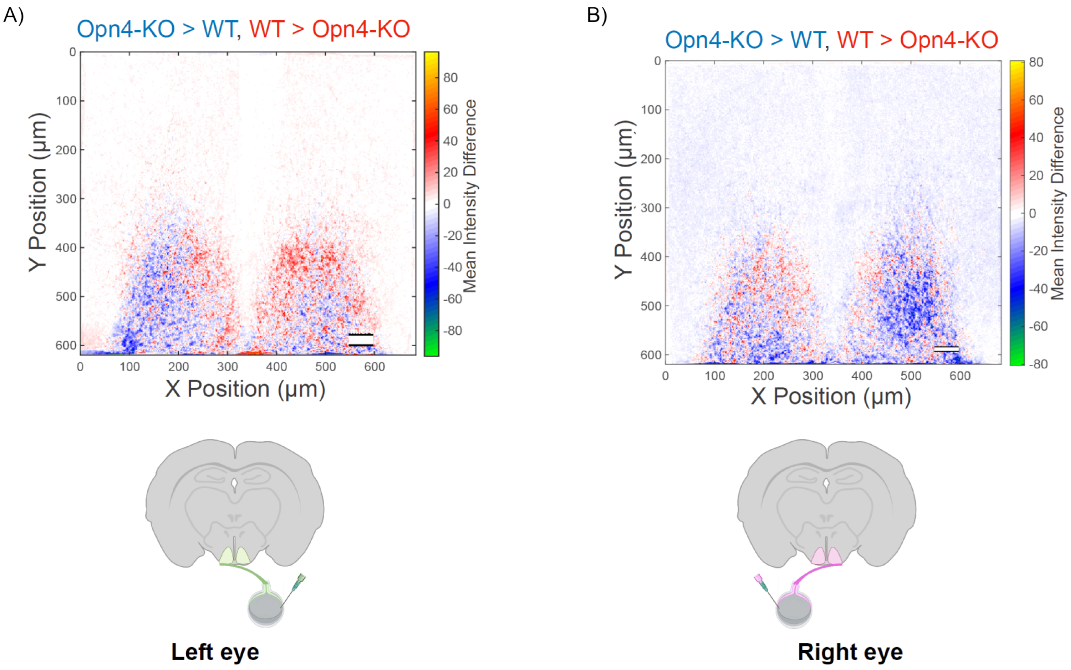

Figure 3.9: Heat maps show altered retinal projections to the SCN in P8 PACAP-cKO mice. Maps compare single-eye projections between genotypes; combined map summarizes bilateral patterns. Warm colors (red-yellow): WT > PACAP-cKO; cool colors (blue-green): PACAP-cKO > WT; white: no difference. WT mice show greater dorsomedial and ipsilateral innervation; PACAP-cKO mice show innervation restricted to ventrolateral SCN bilaterally. Scale bar 50 µm.

contralateral input between genotypes, but PACAP-cKO mice exhibited a narrower distribution with fewer pixels at the distribution tail, suggesting reduced segregation (Fig.3.11). Distribution variance confirmed that P8 WT mice showed significantly greater segregation than P8 PACAP-cKO mice (Welchs t-test $t(9.61) = 4.849$, $^{***}p < 0.001$) (Fig.2.14B). This indicates that PACAP ablation significantly impairs eye-specific segregation in the developing dLGN.

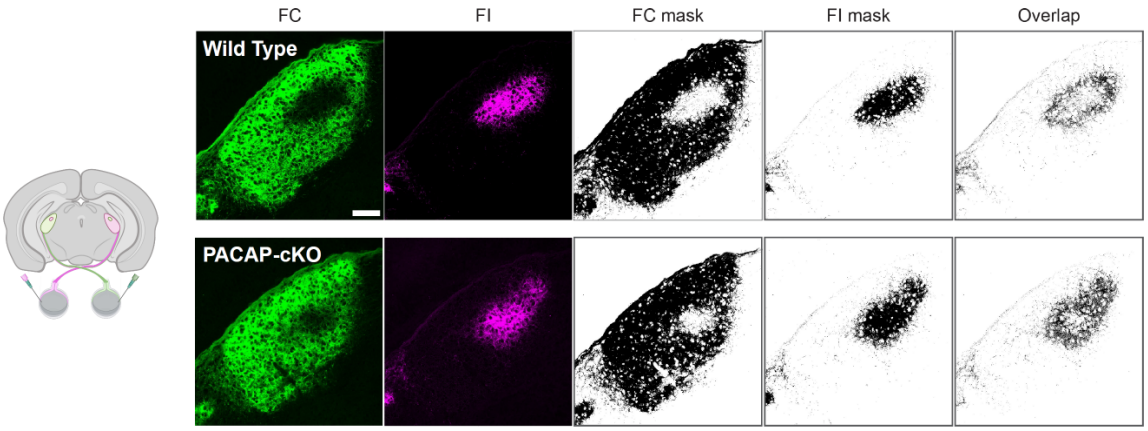

Figure 3.10: Eye-specific segregation in the dLGN of P8 PACAP-cKO and wild-type mice. Representative confocal images of coronal dLGN sections showing the segregation analysis workflow. (FC, FI) Raw fluorescence of contralateral (green, CTB-Alexa 488) and ipsilateral (magenta, CTB-Alexa 647) RGC projections. (FC mask, FI mask) Binary masks after thresholding and background subtraction. (Overlap) Overlap map showing colocalized projections (black). PACAP-cKO mice show greater spatial overlap of ipsilateral and contralateral territories than wild type mice. Scale bar 100 μm.

3.4 Discussion

3.4.1 PACAP Modulates ipRGC Projection Development to the SCN

The results of this chapter show that PACAP in ipRGCs plays a minor modulatory role in retinal projection development to the SCN. In conditional ipRGC-specific PACAP knockout mice, SCN innervation was largely normal, with strongest projections in the ventrolateral region where contralaterally projecting RHT axons enter (Fig. 3.4). However, PACAP-deficient projections grouped in the lateral SCN from ventral to dorsal, but failed to extend medially, though bilateral SCN innervation remained intact. The reduction in density and altered innervation pattern was less severe than in melanopsin knockout mice, suggesting PACAP plays a minor role

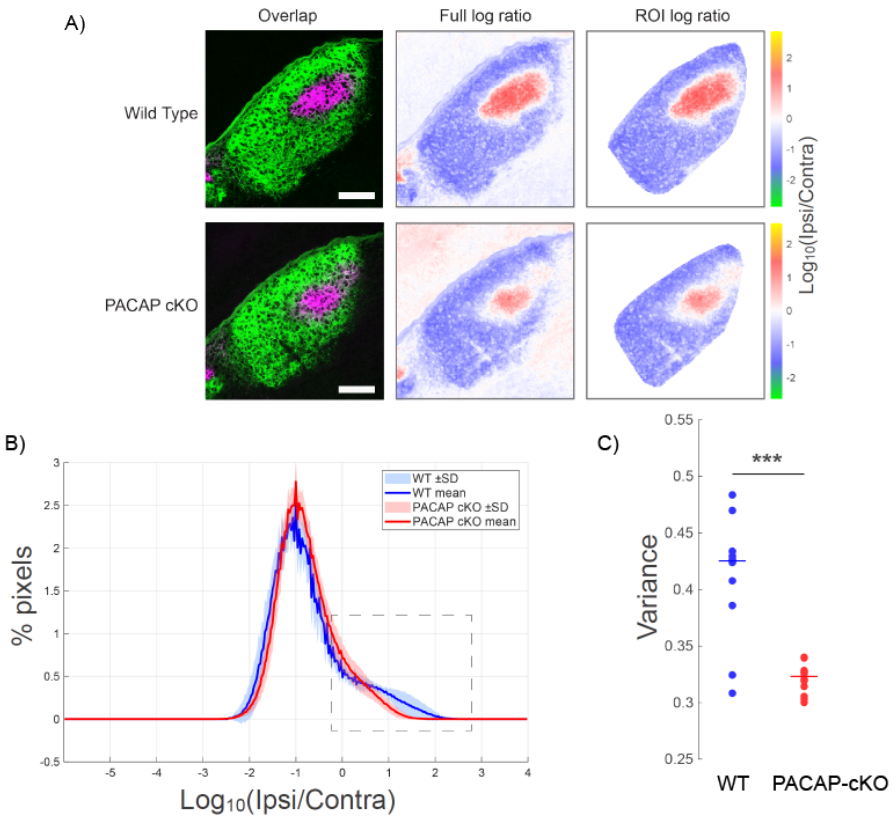

Figure 3.11: PACAP-cKO mice show decreased eye-specific segregation in the dLGN. (A)(Overlap) Representative dual-color fluorescence overlays showing retinal projections from the contralateral eye (green, CTB-Alexa 488) and ipsilateral eye (magenta, CTB-Alexa 647) from P8 wild-type mice and PACAP-cKO mice show decreased eye-specific segregation in the dLGN. (Full log ratio, ROI log ratio) Logarithmic ratio heat maps ($R = \text{Log}_{10}(F_I/F_C)$) showing the degree of eye dominance for each pixel. Red indicates ipsilateral dominance (positive R), blue indicates contralateral dominance (negative R), and white indicates equal input ($R \approx 0$). Wild-type mice display a broader range of R values with more distinct eye-dominant regions, while PACAP-cKO mice show narrower values, reflecting reduced segregation. Scale bar 100 µm. (B) Distribution of logarithmic intensity ratios for all pixels within the dLGN. Positive R values represent pixels with greater ipsilateral fluorescence; negative values represent greater contralateral fluorescence. The distribution for wild-type mice (blue) is broader than that of PACAP-cKO mice (red), indicating better segregation. Inset shows expanded view highlighting the difference in distribution width. (C) Quantification of segregation using variance of the Log_{10} ratio distributions. Wild type mice show significantly greater variance than PACAP-cKO mice, indicating better eye-specific segregation (Welch's unpaired t-test: $t(9.61) = 4.849$, $^{***}p < 0.001$; n = 14 WT and 16 PACAP-cKO mice). Error bars represent standard error of the mean.

in the development of retinal projections to the SCN at this developmental stage. Retinal axons are known to rely on molecular cues such as ephrins, semaphorins and cell adhesion molecules for guidance to their target brain areas, rather than on modulatory signals like PACAP. Previous electrophysiological studies showed that PACAP increases glutamatergic transmission in the SCN [14, 68, 106]. In the absence of PACAP, sustained glutamatergic input may be reduced and could impact molecular cue signaling that promotes axon growth.

3.4.2 Bilateral Innervation and the Role of PACAP

Overall intensity distributions show small magnitude differences between PACAP-cKO and wild-type mice, but the spatial analysis detected an abnormal pattern. Even though the shapes of the intensity distributions are significantly different, the effect sizes are negligible (Fig. 3.5), pointing to a subtle remodeling rather than loss of innervation. In contrast, medial innervation patterns clearly differ between genotypes (Figs. 3.6 and 3.7). In PACAP-cKO, retinal projections innervate both contralateral and ipsilateral SCN, but remain restricted to lateral regions while the medial region is nearly devoid of projections (Fig. 3.6). PACAP thus appears to have a modulatory role, fine-tuning specific aspects of innervation density and laterality after axons reach the SCN, rather than determining overall projection positioning. By comparison, melanopsin loss alters the topography more broadly, underscoring that the absence of PACAP in ipRGCs is less severe than the absence of melanopsin at early postnatal developmental stages (Fig. 3.6).

3.4.3 Interpreting the Magnitude of Effects

The asymmetry in retinal projections from individual eyes in PACAP-cKO mice (Fig. 3.9) suggests that inputs predominantly remain contralateral, and fewer axons cross to the ipsilateral SCN. PACAP may normally facilitate ipsilateral crossing by promoting the release of neurotrophic factors as has been reported in hippocampal neurons, where PACAP-dependent release of BDNF results in TRkB receptor activation, promoting axon growth [76]. Compared with *Opn4*-KO mice, which show exclusive ventral clustering while preserving medial innervation, the PACAP-cKO phenotype appears milder and more spatially selective (Fig. 3.6). This pattern supports the interpretation that melanopsin-dependent activity plays a larger role for the growth of retinal projections across the SCN, while PACAP modulates local arbor density in the medial region of the SCN. PACAP could regulate axon branching in the medial SCN by potentiating synaptic strength through PLC / PKC / tyrosine kinase signaling pathway, thereby stabilizing axon contacts [64].

3.4.4 Potential Mechanisms of PACAP-modulated Segregation

Unexpectedly, the second major finding of this chapter is that PACAP contributes in an important way to the refinement of eye-specific domains in the dLGN at P8. (Fig. 3.10). PACAP-cKO mice exhibited reduced segregation of ipsilateral and contralateral retinal inputs compared to wild-type controls (Fig. 3.11), consistent with PACAP enhancing activity-dependent synaptic refinement mecha-

nisms during early visual circuit development. This impairment fits with established actions of PACAP at glutamatergic synapses, facilitating presynaptic glutamate release and enhancing postsynaptic AMPA/NMDA currents via PAC1R/AC/PKA signaling, which could strengthen correlated inputs and accelerate competitive elimination of mismatched terminals during segregation [14, 68].

PACAP released from ipRGCs may also modulate spontaneous retinal activity to promote dLGN circuit maturation. During early postnatal development, retinal waves are the primary source of neural activity that drives synaptic competition between ipsilateral and contralateral axonal inputs to the dLGN [99, 100]. ipRGCs are active participants in retinal waves, gen-erating intrinsic calcium oscillations and influencing the excitability of surrounding amacrine and bipolar cells through dendrodendritic signaling and gap-junction coupling [60, 80, 83]. PACAP also interacts with dopaminergic amacrine cells, key mod-ulators of retinal excitability and wave propagation, promoting neural differentiation and activity of dopaminergic neurons through PAC1R-dependent cAMP/PKA signaling [7]; ipRGCs also provide direct excitatory input to these amacrine cells [83]. Dopamine, in turn, regulates gap-junction coupling among ganglion and amacrine cells, regulating correlated activity. A reduction of PACAP signaling could decrease dopamine release, reducing the spatial coherence of retinal waves. In addition, PACAP and PAC1R are expressed in bipolar cells and Muller glia, where they regulate ion and neurotransmitter homeostasis, modulating both the amplitude and recovery of wave-associated depolarizations [57, 73]. Taken together, PACAP released from ipRGCs may fine-tune retinal wave dynamics by enhancing excitatory transmission and synchronizing network ac-

tivity during the critical period of retinogeniculate refinement. Thus, PACAP likely contributes to the developmental refinement of the dLGN indirectly, by modulating the amplitude and temporal structure of spontaneous retinal activity that instructs the segregation of retinal inputs.

PACAP may regulate the refinement of retinogeniculate connections by acting directly on postsynaptic neurons in the dLGN, where PAC1R activation modulates excitatory synaptic transmission and postsynaptic excitability. PAC1R-dependent activation enhances the amplitude of NMDA and AMPA receptor currents, promoting long-term synaptic potentiation [14, 68]. In the dLGN, stronger or more correlated inputs stabilize synapses through calcium-dependent mechanisms, while weaker or asynchronous inputs are pruned [99, 100]. PACAP can directly influence these processes by increasing postsynaptic calcium influx and activating calcium-dependent transcription factors such as CREB via cAMP/PKA signaling [14, 68], enhancing the expression of neurotrophic factors, including BDNF, which are known to promote synaptic stabilization and dendritic growth [28, 39].

PAC1R and related VPAC receptors are expressed in both excitatory and inhibitory neurons across the whole thalamus [34, 108]. In GABAergic cells, PACAP can elevate cAMP levels and alter the balance between excitation and inhibition [108, 109]. PACAP could adjust inhibitory tone and network synchrony, controlling the temporal precision of postsynaptic responses to retinal input. Similarly, PACAP acting on astrocytes could regulate glutamate clearance and metabolic coupling through induction of glutamate transporters GLT-1 and GLAST [26]. In contrast, the impaired segregation seen in PACAP-cKO mice (Fig. 3.11) could be due to re-

duced cAMP/PKA signaling resulting in lower NMDA receptor activation, reduced CREB phosphorylation, and decreased expression of plasticity-related genes. Consistent with this, PACAP deficiency in hippocampal and cortical neurons results in fewer den-dritic spines, impaired long-term potentiation, and abnormal axonal arborization [39, 66, 107]. PACAP-mediated signaling in dLGN neurons could modulate eye-specific segregation in the dLGN by enhancing postsynaptic excitability, activating calcium- and cAMP-dependent transcriptional programs, and coordinating excitatory/inhibitory homeostasis.

3.4.5 Methodological Considerations

In my experiments, CTB signal intensity is not equivalent between the two eye-specific channels. Specifically, right-eye CTB-647 in some PACAP-cKO sections is dimmer, which can bias registration and reduce apparent ipsilateral contributions to the abnormalities seen in the SCN and dLGN of PACAP-cKO mice. This reduced signal from the right-eye CTB-647 is more evident in the SCN analysis where there is a strong background and fluorescent intensity (Fig. 3.9) is lower than the left-eye CTB-488 (Fig. 3.8).

Second, the analysis done in this thesis represents a snapshot of the developmental process at P8 only. The developmental stage precedes the maturation of cone and rod photoreceptor synapses [6, 97]. The impairment of segregation in PACAP-cKO could be transient, and may recover after eye-opening and visual experience as has been seen in other models with segregation defects [71, 88]. However PACAP is

essential for proper development of nervous system, and germline PACAP knockout mice do not survive due to irreversible abnormalities in development [94].

Third, mesoscale intensity measures infer axon arbor density and overlap but do not count synapses. The dorsomedial"shell of the SCN is enriched with AVP-expressing, PAC1R-rich neurons [30] that coordinate circadian outputs and was recently discovered to receive abundant retinal input [8, 61]. In PACAP-cKO mice, ipRGC axons reached the ventrolateral of core of SCN, housing VIP- and GRP-expressing neurons, but fail to extend into the shell (Fig. 3.6). However, there is no evidence of PACAP acting as a growth-permissive and synapse-stabilizing cotransmitter in the SCN.

In the dLGN, my results extend prior work that implicated ipRGC activity in the refinement of dLGN projections [12]. While previous studies demonstrated that ablation of ipRGCs disrupts segregation, the present data identify PACAP as one of the signaling molecules mediating this effect. If these findings persist after adding additional biological replicates, this will provide the first direct evidence that a neuropeptide co-released by ipRGCs participates in the structural maturation of image-forming visual pathways. In this context, my results provide the missing mechanistic link between earlier anatomical observations of PACAP-positive fibers in the dLGN [34] and physiological studies of PACAPs synaptic actions in other brain regions.

Some discrepancies with existing literature may reflect developmental differences in different species. For example, PACAP enhances synaptic plasticity and LTP in the SCN and hippocampus [39, 66, 107], whereas PACAP-dependent effects

in the dLGN have not been determined. PACAP-positive fibers have been seen in the dLGN of monkey, but the same has not been determined in mice [34]. This suggests that PACAPs developmental functions could depend on differential evolution of species even though PACAP is widely expressed [94].

3.4.6 Broader Implications and Conclusions

I found that PACAP modulates early targeting of ipRGC projections to the SCN and critically regulates eye-specific segregation in the dLGN at P8. PACAPs minor role in SCN projection development supports a model in which glutamatergic-dependent guidance establishes projection topology, while PACAP tunes local arbor density and laterality (Fig. 3.4, Fig. 3.5, Fig. 3.6). In contrast, PACAP play a critical role in eye-specific refinement in the dLGN evidenced by the impairment seen in PACAP-cKO mice (Fig. 3.11), arguing in favor of PACAP as an enhancer of activity-dependent competition mechanisms.

Together, these findings integrate known roles for PACAP in potentiating glutamatergic transmission and modulating axon growth and structural plasticity. The results of this thesis identify a specific ipRGC co-transmitter as a mechanistic contributor to ipRGC development, positioning PACAP as a modulatory missing link between ipRGC activity and structural maturation.

This work is novel in demonstrating that the absence of PACAP in ipRGCs selectively impairs eye-specific segregation without destabilizing SCN innervation, thereby separating targeting from refinement for a peptidergic co-transmitter. Con-

ceptually, it advances our understanding of neuropeptides as modulators of retinofugal development and motivates new avenues of research to find therapeutic tools for developmental disorders.

Chapter 4: General Discussion

4.1 A General Framework

ipRGCs are intriguing cells that transmit photoreceptor-evoked and melanopsin-driven activity through glutamatergic, GABAergic and peptidergic (PACAP) signaling to the brain [14, 68, 95]. In early postnatal life, melanopsin-driven activity generates Ca^{2+} transients in ipRGC axonal terminals [15], triggering neurotransmitter and PACAP co-release. PACAP acts through PAC1/VPAC receptors to trigger cAMP/PKA and PLC/PKC signaling cascades that potentiate transmission and drive growth-related gene transcription [14, 70], stabilizing axonal arborization and facilitating terminal refinement. My results show that melanopsin and PACAP have distinct but complementary effects on retinohypothalamic tract (RHT) and retinogeniculate development. Melanopsin loss clusters RHT inputs ventrolaterally in the SCN and has a minor impact on eye-specific segregation in the dLGN is disrupted. PACAP loss reduces medial SCN inputs and more severely impacts segregation in the dLGN.

4.2 Candidate Molecular Mechanisms

4.2.1 Presynaptic Cooperation

Melanopsin activation triggers a $G_{q/11}$/PLCβ signaling, generates IP_3 and DAG to elevate intracellular Ca^{2+} through TRPC channels and PKC [15, 95]. This results in long depolarizations that promote synapsin phosphorylation via CaMKII, mobilizing synaptic vesicles from the readily-releasable pool to the active zone and enhancing glutamate release [43]. At the same time, Ca^{2+}-dependent activation of Rac1 and Cdc42 remodels the actin cytoskeleton, promoting exploratory axonal branching and synaptic bouton formation. Through these mechanisms, melanopsin-driven activity provides both the energetic and structural underpinnings for presynaptic maturation and target-specific innervation. PACAP co-release amplifies these melanopsin-dependent processes. By activating PAC1 receptors that couple to G_s and G_q signaling pathways, PACAP increases cAMP and Ca^{2+} levels, recruiting PKA and PKC to phosphorylate synapsin, SNAP-25, and voltage-gated Ca^{2+} channels, mobilizing synaptic vesicles to active zones and enhancing neurotransmission [14, 66, 68]. PACAP-dependent MAPK/ERK signaling promotes transcription of synaptic stability genes and cytoskeletal regulators [74]. Without melanopsin, ipRGCs lack sufficient depolarizing drive for axonal terminal maturation. Without PACAP, axon terminals lack biochemical support for bouton stabilization and axonal arbor branching. Together, these two signaling systems may establish a cooperative mechanism in which melanopsin generates presynaptic activation and

PACAP stabilizes it, providing robust, long-lasting synaptic connectivity between ipRGCs and their central visual targets.

4.2.2 Postsynaptic Amplification

Melanopsin driven glutamate release produces rhythmic depolarizations and Ca^{2+} influx through NMDA receptors and voltage-gated calcium channels [77]. This Ca^{2+} influx activates CaMKII and CREB to increases PSD95 and Homer scaffolding proteins expression, clutstering AMPA receptors and strengthening synapses. This Ca^{2+}-dependent signaling synchronizes gene expression with light cycles and promotes structural plasticity of dendritic spines.

PACAP enhances these effects via PAC1 receptors expressed in SCN and dLGN neurons. PAC1R-triggered adenylyl cyclase and PLC pathways increase cAMP and intracellular Ca^{2+}, activating PKA, PKC, and ERK to drive CREB/MAPK-dependent transcription of BDNF, synapsin, and cytoskeletal regulators. PACAP also enhances glutamate responses by phosphorylating and clustering AMPA/NMDA receptors. Thus, melanopsin provides the frequent electrical input that shapes circuit specificity, and PACAP may trigger transcriptional programs stabilizing postsynaptic connectivity.

4.2.3 Activity-Dependent Local Translation

To respond in an effective way to guidance cues during development, axons do not rely on protein machinery that is slowly trnasported from the soma. Instead,

axons make use of local protein synthesis to produce fast structural changes [44]. Axons contain all the machinery necessary (e.g. mRNAs, ribosomes) to make axonal cone and terminals grow as a result of activity-dependent synthesis of proteins such as beta-actin that guide cone growth and promote branching. Moreover, the axons locally produce hundreds of nascent proteins in response to extracellular cues allowing them to translate proteins in their axons themselves to rapidly meet developmental programs such as axonal branching and target innervation [44]. Since ipRGCs are responsible for light-evoked activity at eatly postnatal age to guide development,reduced activity in *Opn4*-KO and PACAP-cKO could reduce activity-dependent local translation and synthesis of signaling proteins required for axonal cone growth, and axonal branching, limiting the stabilization and development of innervation within the SCN. The abonormal development of ipRGC projections in the SCN boserved in *Opn4*-KO and PACAP-cKO mice could arise from a decrease in cellular activity impairing local translational programs that normally support axon growth, branching, and synapse formation in developing retinohypothalamic projections. Thus, loss of melanopsin- or PACAP-dependent activity in ipRGCs could impair the local axonal translation machinery required for normal growth and branching of retinohypothalamic projections.

4.2.4 Retinal Waves Modulation

Melanopsin and PACAP may have coordinated effects on retinal waves by connecting melanopsin-dependent activity of ipRGCs to neuromodulatory control

of the retinal network. Light exposure prolongs retinal wave activity in neonatal mice [85] and melanopsin-driven ipRGC activity affects wave timing, propagation patterns, and burst duration, introducing light sensitivity into an otherwise spontaneous network. Light-activated ipRGCs increase dopamine release, and this signaling adjusts wave frequency by via dopamine D1/D2 receptor-mediated control of Cx36 phosphorylation [54], synchronizing inter-eye wave phases to refine correlated firing essential for establishing retinotopic and eye-specific mapping. PACAP may complement and modulate this process by fine-tuning the amplitude and propagation dynamics of retinal waves. Through PAC1 receptors on dopaminergic amacrine cells [83], PACAP promotes the differentiation dopaminergic amacrine cells during development [7]. PACAP also increases neurogenesis of horizontal cells that could participate in sporadic retinal activity [18]. Together, melanopsin and PACAP represent a dual mechanism in which light-dependent excitation and peptide modulation act in concert to sculpt the temporal and spatial properties of retinal waves that guide the formation of precise binocular projections in the developing visual system.

4.2.5 Contralateral Dominance in the SCN

The graded effects of melanopsin loss producing stronger disruption than PACAP loss, suggest complementary roles: melanopsin drives activity-dependent mechanisms that sustain exploratory growth, whereas PACAP consolidates terminal stabilization and synaptic maturation once axons have reached their targets. Without melanopsin, ipRGC growth cones may lose motility and fail to respond ap-

propriately to molecular cues such as ephrin-A or semaphorin gradients. Likewise, loss of PACAP signaling may reduce cAMP/MAPK-mediated cytoskeletal regulation, preventing terminals from expanding into the medial SCN. Thus, diminished PACAP activity may impair the full stabilization of ipRGC axonal arbors in the lateral SCN, providing a plausible explanation for the incomplete innervation observed in both *Opn4*-KO and PACAP-cKO.

The persistence of predominantly contralateral innervation may further reflect combined deficits in activity-dependent competition, interhemispheric balance, and retrograde feedback. A population of ipRGCs may extend their axons bilaterally in the SCN which could be maintained by patterned activity or neurotrophic factors such as BDNF. In *Opn4*-KO mice, diminished light-driven excitation could weaken this reinforcement, leading to retraction or prevention of crossing collaterals. In PACAP-cKO mice, light responses remain intact, but reduced PAC1R signaling in SCN neurons could impair neuronal differentiation by interfering with neurotrophic-dependent development, limiting medial and bilateral arborization.

4.2.6 dLGN Segregation Impairment

PACAP loss produces stronger disruption of eye-specific segregation than the loss of melanopsin, suggesting PACAP may transform melanopsin-initiated signals into lasting structural changes. Several mechanisms could be possible including presynaptic enhancement of vesicle release and bouton stability through cAMP/PKA/PKC [66], postsynaptic increases in receptor trafficking, cytoskeletal

reorganization, and BDNF expression [28, 39, 74, 76], and/or modulation of retinal wave correlations before projections reach their targets. Together, these effects could explain why PACAP loss produces larger effects on segregation than melanopsin loss: melanopsin initiates the competitive signal, but PACAP transforms that signal into lasting structural and functional asymmetry. Additionally, PACAPs neuroprotective properties block apoptosis and reduce Ca^{2+} overload [46]. These effects may regulate dLGN cell survival during development, with effects on competition and pruning that sharpen segregation.

4.3 Future Directions

Several critical questions remain regarding the mechanisms underlying ipRGC projection development. First, the temporal dynamics and permanence of observed deficits are unclear. Longitudinal studies tracking SCN innervation and dLGN segregation from before eye opening through adulthood would distinguish transient developmental delays from irreversible wiring defects. Second, establishing causal relationships requires targeted manipulations: conditional ablation of PAC1 receptors in SCN/dLGN during critical periods (P5-P10) would confirm whether PACAP acts through its cognate receptor, while rescue experiments restoring PACAP expression could demonstrate sufficiency. Third, the cellular and synaptic locus of these effects remains unresolved. Whether PACAP primarily affects presynaptic release probability at ipRGC terminals, postsynaptic receptivity in target neurons, or both could be determined through electrophysiological recordings paired with optogenetic

stimulation. Additionally, the upstream retinal mechanisms warrant investigation, particularly whether altered spontaneous wave activity in melanopsin-deficient retinas drives the observed projection abnormalities.

A deeper understanding also requires improved anatomical resolution and cell-type specificity. Single-axon reconstructions using sparse genetic labeling would enable precise quantification of branch complexity, bouton density, and synapse distribution across SCN subregions and dLGN domains, moving beyond population-level intensity measurements. Furthermore, identifying which SCN neuronal subtypes (VIP, GRP, AVP, or Calretinin populations) receive ipRGC input through monosynaptic tracing would reveal whether PACAP loss preferentially disrupts specific circadian circuits. Finally, manipulating postsynaptic excitability independently of retinal drive could dissect whether target neuron activity serves as a permissive signal for arbor stabilization. Together, these experiments would transform correlative observations into mechanistic insights linking melanopsin signaling, PACAP release, and the developmental refinement of retinofugal projections.

Bibliography

[1] Aranda M., and Schmidt, T. (2021). Diversity of intrinsically photosensitive retinal ganglion cells: circuits and functions. *Cellular and molecular life sciences*, 78, 889-907

[2] Arroyo, D. A., and Feller, M. B. (2016). Spatiotemporal Features of Retinal Waves Instruct the Wiring of the Visual Circuitry. *Frontiers in Neural Circuits*, 10(JUL2016), 54.

[3] Bedont, J., and Blackshaw, S. (2015). Constructing the suprachiasmatic nucleus: a watchmaker's perspective on the central clockworks. *Frontiers in systems neuroscience*, 9, 74

[4] Beier, C., Zhang, Z., Yurgel M., and Hattar S. (2020). Projections of ipRGCs and conventional RGCs to retinorecipient brain nuclei. *Journal of Comparative Neurology*, 529, 1863:1875

[5] Blankenship, A., and Feller, M. (2010). Mechanisms underlying spontaneous patterned activity in developing neural circuits. *Nature Reviews Neuroscience*, 11(1), 1829

[6] Bonezzi, P. J., Tarchick, M. J., Moore, B. D., and Renna, J. M. (2023). Light drives the developmental progression of outer retinal function. *The Journal of general physiology*, 155(9), e202213262

[7] Borba, J., Henze, I., Silveira, M., Kubrusly, R., Gardino, P., de Mello, M., Hoko, J., and de Mello, F. (2005). Pituitary adenylate cyclase-activating polypeptide (PACAP) can act as determinant of the tyrosine hydroxylase phenotype of dopaminergic cells during retina development. *Brain research. Developmental brain research*, 156(2), 193201

[8] Calligaro, H., Shoghi, A., Chen, X., Kim, K. Y., Yu, H. L., Khov, B., Finander, B., Le, H., Ellisman, M. H., and Panda, S. (2023). Ultrastructure of Synaptic Connectivity within Subregions of the Suprachiasmatic Nucleus Revealed by a Genetically Encoded Tag and Serial Blockface Electron Microscopy. *eNeuro*, 10(8), ENEURO.0227-23.2023

[9] Chang, J., Chen, F., Yoon, Y., Jung, E., Babcock, H., Kang, J., Asano, S., Suk, H., Pak, N., Tillberg, P., Wassie, A., Cai, D., and Boyden, E. (2017). Iterative expansion microscopy. *Nature methods*, 14(6), 593599

[10] Chen, F., Tillberg, P., and Boyden, E. (2015). Expansion microscopy. *Science*, 347(6221), 543-548

[11] Chen, F., Wassie, A., Cote, A., Sinha, A., Alon, S., Asano, S., Daugharthy, E., Chang, J., Marblestone, A., Church, G., Raj, A., and Boyden, E. (2016). Nanoscale imaging of RNA with expansion microscopy. *Nat Methods*, 13, 67984

[12] Chew, K., Renna, J., McNeill, D., Fernandez, D., Keenan, W., Thomsen, M., Ecker, J., Loevinsohn, C., Vicarel, D., Tufford, A., Weng, S., Gray, P., Cayouette. M., Herzog, E., Zhao, H., Berson, D., and Hattar, S. (2017). A subset of ipRCSs regulates both maturation of the clock and segregation of retinogeniculate projections in mice. *eLIFE*, 6:e22861

[13] Chozinski, T., Halpern, A., Okawa, H., Kim, H., Tremel, G., Wong, R., and Vaughan, J. (2016). Expansion microscopy with conventional antibodies and fluorescent proteins. *Nature Methods*, 13, 485488

[14] Colwell, C. (2011). Linking neural activity and molecular oscillations in the SCN. *Nature Reviews*, 12, 553-569

[15] Contreras, E., Bhoi, J., Sonoda, T., Birnbaumer, L., and Schmidt T. (2023). Melanopsin activates divergent phototransduction pathways in intrinsically photosensitive retinal ganglion cell subtypes. *eLife*, 12:e80749

[16] Damstra, H., Mohar, B., Eddison, M., Akhmanova, A., Kapitein, L., and Tillberg, P. (2022). Visualizing cellular and tissue ultrastructure using Ten-fold Robust Expansion Microscopy (TREx). *eLife*, 11, e73775

[17] Damstra, H., Passmore, J., Serweta, A., Koutlas, I., Burute, M., Meye, F., Akhmanova, A., and Kapitein, L. (2023). GelMap: intrinsic calibration and deformation mapping for expansion microscopy. *Nat Methods*, 20, 15731580

[18] Denes, V., Hideg, O., Nyisztor, Z., Lakk, M., Godri, Z., Berta, G., Geck, P., and Gabriel, R. (2019). The Neuroprotective Peptide PACAP1-38 Contributes to Horizontal Cell Development in Postnatal Rat Retina. *Investigative ophthalmology and visual science*, 60(2), 770778

[19] Do, M. (2019). Melanopsin and the intrinsically photosensitive retinal ganglion cells: biophysics to behavior. *Neuron*, 104, 205-226

[20] D'Souza, S. P., Upton, B. A., Eldred, K. C., Glass, I., Nayak, G., Grover, K., Ahmed, A., Nguyen, M. T., Hu, Y. C., Gamlin, P., and Lang, R. A. (2024). Developmental control of rod number via a light-dependent retrograde pathway from intrinsically photosensitive retinal ganglion cells. *Developmental cell*, 59(21), 28972911.e6

[21] Ecker, J., Dumitrescu, O., Wong, K., Alam, N., Chen, S., LeGates, T., Renna, J., Prusky, G.,Berson, D., and Hattar, S. (2010) Melanopsin-expressing retinal ganglion-cell photoreceptors: cellular diversity and role in pattern vision. *Neuron*, 67, 4960

[22] Engelund, A., Fahrenkrug, J., Harrison, A., and Hannibal, J. (2010). Vesicular glutamate transporter 2 (VGLUT2) is co-stored with PACAP in projections from the rat melanopsin-containing retinal ganglion cells. *Cell and tissue research*, 340(2), 243255

[23] Esquiva, G., and Hannibal, J. (2019). Melanopsin-expressing retinal ganglion cells in aging and disease. *Histology Histopathology*, 34(12), 1299-1311

[24] Feigl, B., Dumpala, S., Kerr, G., Zele, A. (2020). Melanopsin cell dysfunction is involved in sleep disruption in Parkinson's disease. *Journal of Parkinsons Disease*, 10, 14671476

[25] Fernandez, D., Chang, Y., Hattar, S., and Chen, S. (2016). Architecture of retinal projections to the central circadian pacemaker. *Proc Natl Acad Sci*, 113, 60476052

[26] Figiel M, and Engele J. (2000). Pituitary adenylate cyclase-activating polypeptide (PACAP), a neuron-derived peptide regulating glial glutamate transport and metabolism. *Journal of Neuroscience*, 20(10), 3596-3605

[27] Fleury, G., Masís-Vargas, A., and Kalsbeek, A. (2020). Metabolic Implications of Exposure to Light at Night: Lessons from Animal and Human Studies. *Obesity*, 28, Suppl 1, S18-S28

[28] Fukuchi, M., Tabuchi, A., Kuwana, Y., Watanabe, S., Inoue, M., Takasaki, I., Izumi, H., Tanaka, A., Inoue, R., Mori, H., Komatsu, H., Takemori, H., Okuno, H., Bito, H., and Tsuda, M. (2015). Neuromodulatory effect of Gs- or Gq-coupled G-protein-coupled receptor on NMDA receptor selectively activates the NMDA receptor/Ca2+/calcineurin/cAMP response element-binding protein-regulated transcriptional coactivator 1 pathway to effectively induce brain-derived neurotrophic factor expression in neurons. *The Journal of neuroscience : the official journal of the Society for Neuroscience*, 35(14), 56065624

[29] Gao, F., Ma, J., Yu, Y., Gao, X., Bai, Y., Sun, Y., Liu, J., Liu, X., Barry, D., Wilhelm, S., Piccinni-Ash, T., Wang, N., Liu, D., Ross, R., Hao, Y., Huang, X., Jia, J., Yang, Q., Zheng, H., van Nispen, J., Chen, J., Li, H., Zhang, J., Li, Y., and Chen, Z. (2022). A non-canonical retina-ipRGCs-SCN-PVT visual pathway for mediating contagious itch behavior. *Cell Reports*, 41, 111444

[30] Hannibal, J., Hindersson, P., Knudsen, S., Georg, B., and Fahrenkrug, J. (2002). The photopigment melanopsin is exclusively present in pituitary adenylate cyclase-activating polypeptide-containing retinal ganglion cells of the retinohypothalamic tract. *The Journal of Neuroscience*. 22, RC191, 1-7

[31] Hannibal, J., and Fahrenkrug, J. (2004). Target areas innervated by PACAP-immunoreactive retinal ganglion cells. *Cell and Tissue Research*, 316, 99-113

[32] Hannibal, J., and Fahrenkrug, J. (2006). Neuronal input pathways to the brain's biological clock and their functional significance. *Advances in anatomy, embryology*, and cell biology, 182, 171.

[33] Hannibal, J., Brabet, P., and Fahrenkrug, J. (2008). Mice lacking the PACAP type I receptor have impaired photic entrainment and negative masking. *American journal of physiology. Regulatory*, integrative and comparative physiology, 295(6), R2050R2058

[34] Hannibal, J., Kankipati, L., Strang, C. E., Peterson, B. B., Dacey, D., and Gamlin, P. D. (2014). Central projections of intrinsically photosensitive retinal ganglion cells in the macaque monkey. *The Journal of comparative neurology*, 522(10), 22312248

[35] Hashimoto, H., Hashimoto, R., Shintani, N., Tanaka, K., Yamamoto, A., Hatanaka, M., Guo, X., Morita, Y., Tanida, M., Nagai, K., Takeda, M., and Baba, A. (2009). Depression-like behavior in the forced swimming test in PACAP-deficient mice: amelioration by the atypical antipsychotic risperidone. *Journal of Neurochemistry*, 110, 595602

[36] Hattar, S., Liao, H. W., Takao, M., Berson, D. M., and Yau, K. W. (2002). Melanopsin-containing retinal ganglion cells: architecture, projections, and intrinsic photosensitivity. *Science*, 295(5557), 10651070

[37] Hattar, S., Lucas, R. J., Mrosovsky, N., Thompson, S., Douglas, R. H., Hankins, M. W., Lem, J., Biel, M., Hofmann, F., Foster, R. G., and Yau, K. W. (2003). Melanopsin and rod-cone photoreceptive systems account for all major accessory visual functions in mice. *Nature*, 424(6944), 7681

[38] Hattar, S., Kumar, M., Park, A., Tong, P., Tung, J., Yau, K., and Berson, D. (2006). Central projections of melanopsin-expressing retinal ganglion cells in the mouse. *The journal of comparative cells in the mouse*, 497, 326-349

[39] Hayata-Takano, A., Kamo, T., Kijima, H., Seiriki, K., Ogata, K., Ago, Y., Nakazawa, T., Shintani, Y., Higashino, K., Nagayasu, K., Shintani, N., Kasai, A., Waschek, J., and Hashimoto, H. (2019). Pituitary Adenylate Cyclase-Activating Polypeptide Modulates Dendritic Spine Maturation and Morphogenesis via MicroRNA-132 Upregulation. *The Journal of neuroscience*, 39(22), 42084220

[40] Hawke, Z., Ivanov, T., Bechtold, D., Dhillon, H., Lowell, B., and Luckman, S. (2009). PACAP neurons in the hypothalamic ventromedial nucleus are targets of central leptin signaling. *Journal of Neuroscience*, 29, 1482814835

[41] Hell S. (2007). Far-Field Optical Nanoscopy.*Science*, 316,1153-1158

[42] Hermawati, D., Rahmadi, F., Sumekar, T., Winarni, T. (2018). Early electronic screen exposure and autistic-like symptoms. *Intractable and Rare Diseases Research*, 7(1), 69-71

[43] Hinds, H. L., Goussakov, I., Nakazawa, K., Tonegawa, S., and Bolshakov, V. Y. (2003). Essential function of alpha-calcium/calmodulin-dependent protein kinase II in neurotransmitter release at a glutamatergic central synapse. *Proceedings of the National Academy of Sciences of the United States of America*, 100(7), 42754280

[44] Holt, C. E., Martin, K. C., and Schuman, E. M. (2019). Local translation in neurons: visualization and function. *Nature structural and molecular biology*, 26(7), 557566

[45] Hong, J., Zeng, Q., Wang, H., Kuo, D. S., Baldridge, W. H., and Wang, N. (2013). Controlling the number of melanopsin-containing retinal ganglion cells by early light exposure. *Experimental eye research*, 111, 1726

[46] Horvath, G., Reglodi, D., Fabian, E., and Opper, B. (2022). Effects of Pituitary Adenylate Cyclase Activating Polypeptide on Cell Death. *International journal of molecular sciences*, 23(9), 4953

[47] Hu, J., Shi, Y., Zhang, J., Huang, X., Wang, Q., Zhao, H., Shen, J., Chen, Z., Song, W., Zheng, P., Zhan, S., Sun, Y., Cai, P., An, K., Ouyang, C., Zhao, B., Zhou, Q., Xu, L., Xiong, W., Zhang, Z., Meng, J., Chen, J., Ma, Y., Zhao, H., Zhang, M., Qu, K., Hu, J., Luo, M., Xu, F., Chen, X., Xiong, Y., Bao, J., Xue, T. (2022). Melanopsin retinal ganglion cells mediate light-promoted brain development. *Cell*, 185(17), 3124-3137.e15

[48] Huang, B., Babcock, H., Zhuang, X. (2010). Breaking the diffraction barrier: super-resolution imaging of cells. *Cell*, 143(7), 1047-58

[49] Huang, L., Xi, Y., Peng, Y., Yang, Y., Huang, X., Fu, Y., Tao, Q., Xiao, J., Yuan, T., An, K., Zhao, H., Pu, M., Xu, F., Xue, T., Luo, M., So, K., and Ren, C. (2019). A visual circuit related to habenula underlies the antidepressive effects of light therapy. *Neuron*, 102, 128142.e8.

[50] Huberman, A. D., Stellwagen, D., and Chapman, B. (2002). Decoupling eye-specific segregation from lamination in the lateral geniculate nucleus. *The Journal of neuroscience: the official journal of the Society for Neuroscience*, 22(21), 94199429

[51] Huberman, A., Feller, M., and Chapman, B. (2008). Mechanisms underlying development of visual maps and receptive fields. *Annual Review Neuroscience*, 31, 479509

[52] Keenan, W., Rupp, A., Ross, R., Somasundaram, P., Hiriyanna, S., Wu, Z., Badea, T., Robinson, P., Lowell, B., and Hattar, S. (2016). A visual circuit uses

complementary mechanisms to support transient and sustained pupil constriction. *eLife*, 5, e15392

[53] Kim, K. Y., Rios, L. C., Le, H., Perez, A. J., Phan, S., Bushong, E. A., Deerinck, T. J., Liu, Y. H., Ellisman, M. A., Lev-Ram, V., Ju, S., Panda, S. A., Yoon, S., Hirayama, M., Mure, L. S., Hatori, M., Ellisman, M. H., and Panda, S. (2019). Synaptic Specializations of Melanopsin-Retinal Ganglion Cells in Multiple Brain Regions Revealed by Genetic Label for Light and Electron Microscopy. *Cell reports*, 29(3), 628644.e6

[54] Kirkby, L., and Feller, M. (2013). Intrinsically photosensitive ganglion cells contribute to plasticity in retinal wave circuits. *PNAS*, 110(29), 1209012095

[55] Kiyoshi, C., and Tedeschi, A. (2020). Axon growth and synaptic function: A balancing act for axonal regeneration and neuronal circuit formation in CNS trauma and disease. *Developmental neurobiology*, 80(7-8), 277301

[56] Klein, S., Staring, M., Murphy, K., Viergever, M., and Pluim, J. (2010). Elastix: a toolbox for intensity based medical image registration. *IEEE Transactions on Medical Imaging*, 29, 1, 196-205

[57] Kovács-Valasek, A., Szabadfi, K., Dénes, V., Szalontai, B., Tamás, A., Kiss, P., Szabó, A., Setalo, G., Jr, Reglödi, D., and Gábriel, R. (2017). Accelerated retinal aging in PACAP knock-out mice. *Neuroscience*, 348, 110

[58] Ku, T., Swaney, J., Park, J. Y., Albanese, A., Murray, E., Cho, J. H., Park, Y. G., Mangena, V., Chen, J., and Chung, K. (2016). Multiplexed and scalable super-resolution imaging of three-dimensional protein localization in size-adjustable tissues. *Nature biotechnology*, 34(9), 973981

[59] La Morgia, C., Ross-Cisneros, F., Koronyo, Y., Hannibal, J., Gallassi, R., Cantalupo, G., Sambati, L., Pan, B., Tozer, K., Barboni, P., Provini, F., Avanzini, P., Carbonelli, M., Pelosi, A., Chui, H., Liguori, R., Baruzzi, A., Koronyo-Hamaoui, M., Sadun, A., and Carelli, V. (2016). Melanopsin retinal ganglion cell loss in Alzheimer disease. *Annals of Neurology*, 79, 90109

[60] Li, H., Zhang, Z., Blackburn, M., Wang, S., Ribelayga, C., and O'Brien, J. (2013). Adenosine and dopamine receptors coregulate photoreceptor coupling via gap junction phosphorylation in mouse retina. *The Journal of neuroscience*, 33(7), 31353150

[61] Lim, J. H., Stafford, B. K., Nguyen, P. L., Lien, B. V., Wang, C., Zukor, K., He, Z., and Huberman, A. D. (2016). Neural activity promotes long-distance, target-specific regeneration of adult retinal axons. *Nature neuroscience*, 19(8), 10731084

[62] Liu, A. L., Liu, Y. F., Wang, G., Shao, Y. Q., Yu, C. X., Yang, Z., Zhou, Z. R., Han, X., Gong, X., Qian, K. W., Wang, L. Q., Ma, Y. Y., Zhong, Y. M.,

Weng, S. J., and Yang, X. L. (2022). The role of ipRGCs in ocular growth and myopia development. *Science advances*, 8(23), eabm9027

[63] Lucas, R., Hattar, S., Takao, M., Berson, D. M., Foster, R. G., and Yau, K. (2003). Diminished pupillary light reflex at high irradiances in melanopsin-knockout mice. *Science*, 299(5604), 245247

[64] MacDonald, J., Jackson, M., and Beazely, M. (2007). G protein-coupled receptors control NMDARs and metaplasticity in the hippocampus. *Biochimica et biophysica acta*, 1768(4), 941951

[65] Madisen, L., Zwingman, T. A., Sunkin, S. M., Oh, S. W., Zariwala, H. A., Gu, H., Ng, L. L., Palmiter, R. D., Hawrylycz, M. J., Jones, A. R., Lein, E. S., and Zeng, H. (2010). A robust and high-throughput Cre reporting and characterization system for the whole mouse brain. *Nature neuroscience—*, 13(1), 133140

[66] Matsuyama, S., Matsumoto, A., Hashimoto, H., Shintani, N., and Baba, A. (2003). Impaired long-term potentiation in vivo in the dentate gyrus of pituitary adenylate cyclase-activating polypeptide (PACAP) or PACAP type 1 receptor-mutant mice. *Neuroreport*, 14(16), 20952098

[67] McNeill, D., Sheely, C., Ecker, J., Badea, T., Morhardt, D., Guido, W., and Hattar, S. (2011). Development of melanopsin-based irradiance detecting circuitry. *Neural development*, **6**, 8

[68] Michel, S., Itri, J., Han, J., Gniotczynski, K., and Colwell, C. (2006). Regulation of glutamatergic signalling by PACAP in the mammalian suprachiasmatic nucleus. *BMC neuroscience*, 7, 15

[69] Milosavljevic, N., Cehajic-Kapetanovic, J., Procyk, C., and Lucas, R. (2016). Chemogenetic activation of melanopsin retinal ganglion cells induces signatures of arousal and/or anxiety in mice. *Current Biology*, 26, 2358-2363

[70] Moody, T. W., and Jensen, R. T. (2013). Bombesin peptides (cancer). In A. J. Kastin (Ed.), *Handbook of biologically active peptides* 2nd ed., pp. 11881196. Elsevier

[71] Muir-Robinson, G., Hwang, B. J., and Feller, M. B. (2002). Retinogeniculate axons undergo eye-specific segregation in the absence of eye-specific layers. *The Journal of neuroscience: the official journal of the Society for Neuroscience*, 22(13), 52595264

[72] Mustafa, T. (2013). Pituitary adenylate cyclase-activating polypeptide (PACAP): a master regulator in central and peripheral stress responses. *Advances in Pharmacology*, 68, 445457

[73] Nakamachi, T., Matkovits, A., Seki, T., and Shioda, S. (2012). Distribution and protective function of pituitary adenylate cyclase-activating polypeptide in the retina. *Frontiers in endocrinology*, 3, 145

[74] Nielsen, K., Chaverra, M., Hapner, S., Nelson, B., Todd, V., Zigmond, R., and Lefcort, F. (2004). PACAP promotes sensory neuron differentiation: blockade by neurotrophic factors. *Molecular and cellular neurosciences*, 25(4), 629641

[75] Obara, E., Hannibal, J., Heegaard, S., and Fahrenkrug, J. (2016). Loss of melanopsin-expressing retinal ganglion cells in severely staged glaucoma patients. *Investigative Ophthalmology and Visual Science*, 57, 46614667

[76] Ogata, K., Shintani, N., Hayata-Takano, A., Kamo, T., Higashi, S., Seiriki, K., Momosaki, H., Vaudry, D., Vaudry, H., Galas, L., Kasai, A., Nagayasu, K., Nakazawa, T., Hashimoto, R., Ago, Y., Matsuda, T., Baba, A., and Hashimoto, H. (2015). PACAP enhances axon outgrowth in cultured hippocampal neurons to a comparable extent as BDNF. *PloS one*, 10(3), e0120526

[77] Pan, D., Wang, Z., Chen, Y., and Cao, J. (2023). Melanopsin-mediated optical entrainment regulates circadian rhythms in vertebrates. eem Communications biology, 6(1), 1054

[78] Peirson, S., and Foster, R. G. (2006). Melanopsin: another way of signaling light. *Neuron*, 49(3), 331339

[79] Pilorz, V., Tam, S., Hughes, S., Pothecary, C., Jagannath, A., Hankins, M., Bannerman, D., Lightman, S., Vyazovskiy, V., Nolan, P., Foster, R., and Peirson, S. (2016). Melanopsin Regulates Both Sleep-Promoting and Arousal-Promoting Responses to Light. *PLoS biology*, 14(6), e1002482

[80] Prigge, C., Yeh, P., Liou, N., Lee, C., You, S., Liu, L., McNeill, D., Chew, K., Hattar, S., Chen, S., and Zhang, D. (2016). M1 ipRGCs Influence Visual Function through Retrograde Signaling in the Retina. *The Journal of neuroscience*, 36(27), 71847197

[81] Pugh, P. C., and Margiotta, J. F. (2006). PACAP support of neuronal survival requires MAPK- and activity-generated signals. *Molecular and cellular neurosciences*, 31(3), 586595

[82] Purrier, N., Engeland, W., Kofuji, P. (2014). Mice Deficient of Glutamatergic Signaling from Intrinsically Photosensitive Retinal Ganglion Cells Exhibit Abnormal Circadian Photoentrainment. *PLOS ONE*, 9(10): e111449

[83] Raja, S., Milosavljevic, N., Allen, A., and Cameron, M. (2023). Burning the candle at both ends: Intraretinal signaling of intrinsically photosensitive retinal ganglion cells. *Frontiers in cellular neuroscience*, 16, 1095787

[84] Rao, S., Chun, C., Fan, J., Kofron, J., Yang, M., Hegde, R., Ferrara, N., Copenhagen, D., and Lang, R. (2013). A direct and melanopsin-dependent fetal light response regulates mouse eye development. *Nature*, 494(7436), 243246

[85] Renna, J., Weng, S., and Berson, D. (2011). Light acts through melanopsin to alter retinal waves and segregation of retinogeniculate afferents. *Nature Neuroscience*, 14, 827829

[86] Reyes-Méndez, M.E., HerreraZamora, J., OsunaLópez, F., Navarro-Polanco, R.A., Mendoza-Muoz, N., Góngora-Alfaro, J., Moreno-Galindo, E.G., and Alamilla, J. (2021). Light stimulation during postnatal development is not determinant for glutamatergic neurotransmission from the retinohypothalamic tract to the suprachiasmatic nucleus in rats. *European Journal of Neuroscience*, 54, 4497 - 4513

[87] Ross, R., Leon, S., Madara, J., Schafer, D., Fergani, C., Maguire, C. Verstegen, A., Brengle, E., Kong, D., Herbison, A., Kaiser, U., Lowell, B., and Navarro, V. (2018). PACAP neurons in the ventral premammillary nucleus regulate reproductive function in the female mouse. *eLIFE*, 7:e35960

[88] Rossi, F. M., Pizzorusso, T., Porciatti, V., Marubio, L. M., Maffei, L., and Changeux, J. P. (2001). Requirement of the nicotinic acetylcholine receptor beta 2 subunit for the anatomical and functional development of the visual system. *Proceedings of the National Academy of Sciences of the United States of America*, 98(11), 64536458

[89] Sarkar, D., Kang, J., Wassie, A., Schroeder, M., Peng, Z., Tarr, T., Tang, A., Niederst, E., Young, J., Su, H., Park, D., Yin, P., Tsai, L., Blanpied, T., and Boyden, E. (2022). Revealing nanostructures in brain tissue via protein decrowding by iterative expansion microscopy. *Nature biomedical engineering*, 6(9), 10571073

[90] Schindelin, J., Arganda-Carreras, I., Frise, E., Kaynig, V., Longair, M., Pietzsch, T., Preibisch, S., Rueden, C., Saalfeld, S., Schmid, B., Tinevez, J. Y., White, D. J., Hartenstein, V., Eliceiri, K., Tomancak, P., and Cardona, A. (2012). Fiji: an open-source platform for biological-image analysis. *Nature methods*, 9(7), 676682

[91] Schmidt, T., Chen, S., and Hattar, S. (2011) Intrinsically photosensitive retinal ganglion cells: many subtypes, diverse functions. *Trends in Neuroscience*, $bf34$, 11

[92] Sekaran, S., Lupi, D., Jones, S. L., Sheely, C. J., Hattar, S., Yau, K. W., Lucas, R. J., Foster, R. G., and Hankins, M. W. (2005). Melanopsin-dependent photoreception provides earliest light detection in the mammalian retina. *Current biology*, 15(12), 10991107

[93] Shen, J., and Xue, T. (2025). Neural-circuit architecture underlying non-image-forming visual functions. em Current opinion in neurobiology, 93, 103052

[94] Shen, S., Gehlert, D., and Collier, D. (2013). PACAP and PAC1 receptor in brain development and behavior. *Neuropeptides*, 47(6), 421-430

[95] Sonoda, T., Li, J. Y., Hayes, N. W., Chan, J. C., Okabe, Y., Belin, S., Nawabi, H., and Schmidt, T. M. (2020). A noncanonical inhibitory circuit dampens behavioral sensitivity to light. *Science*, 368(6490), 527531

[96] Tajiri, M., Hayata-Takano, A., Seiriki, K., Ogata, K., Hazama, K., Shintani, N., Baba, A., and Hashimoto, H. (2012). Serotonin 5-HT(7) receptor blockade reverses behavioral abnormalities in PACAP-deficient mice and receptor activation promotes neurite extension in primary embryonic hippocampal neurons: therapeutic implications for psychiatric disorders. *Journal of Molecular Neuroscience*, 48, 473481

[97] Tarchick, M. J., Beight, C., Bonezzi, P. B., Peachey, N. S., and Renna, J. M. (2024). Photoreceptor deficits appear at eye opening in Rs1 mutant mouse models of X-linked retinoschisis. *Experimental eye research*, 242, 109872

[98] Tillberg, P., Chen, F., Piatkevich, K., Zhao, Y., Yu C., English, B., Gao, L., Martorell, A., Suk, H., Yoshida, F., DeGennaro, E., Roossien, D., Gong, G., Seneviratne, U., Tannenbaum, S., Desimone, R., Cai, D., and Boyden E. (2016). Protein-retention expansion microscopy of cells and tissues labeled using standard fluorescent proteins and antibodies. *Nature Biotechnology*, 34(9), 987-992.

[99] Tiriac, A., Smith, B., and Feller, M. (2018). Light Prior to Eye Opening Promotes Retinal Waves and Eye-Specific Segregation. *Neuron*, 100(5), 10591065.e4

[100] Torborg, C., and Feller, M. (2004). Unbiased analysis of bulk axonal segregation patterns. *Journal of neuroscience methods*, 135(1-2), 1726

[101] Tufford, A., Onyak, J., Sondereker, K., Lucas, J., Earley, A., Mattar, P., Hattar, S., Schmidt, T., Renna, J., and Cayouette, M. (2018). Melanopsin Retinal Ganglion Cells Regulate Cone Photoreceptor Lamination in the Mouse Retina. *Cell reports*, 23(8), 24162428

[102] Vandewalle, G., Maquet, P., and Dijk, D. (2009). Light as a modulator of cognitive brain function. *Trends in cognitive sciences*. 13(10), 429-438

[103] Vatan, T., Minehart, J. A., Zhang, C., Agarwal, V., Yang, J., and Speer, C. M. (2021). Volumetric super-resolution imaging by serial ultrasectioning and stochastic optical reconstruction microscopy in mouse neural tissue. *STAR protocols*, 2(4), 100971

[104] Veldman, M., Park, C., Eyermann, C., Zhang, J., Zuniga-Sanchez, E., Hirano, A., Daigle, T., Foster, N., Zhu, M., Langfelder, P., Lopez, I., Brecha, N., Zipursky, S., Zeng, H., Dong, H., and Yang, X. (2020). Brainwide Genetic Sparse Cell Labeling to Illuminate the Morphology of Neurons and Glia with Cre-Dependent MORF Mice. *Neuron*, 108(1), 111127.e6

[105] Welsh, D. K., Takahashi, J. S., and Kay, S. A. (2010). Suprachiasmatic nucleus: cell autonomy and network properties. *Annual review of physiology*, 72, 551577

[106] Webb, I. C., Coolen, L. M., and Lehman, M. N. (2013). NMDA and PACAP receptor signaling interact to mediate retinal-induced scn cellular rhythmicity in the absence of light. PloS one, 8(10), e76365

[107] Yamada, K., Matsuzaki, S., Hattori, T., Kuwahara, R., Taniguchi, M., Hashimoto, H., Shintani, N., Baba, A., Kumamoto, N., Yamada, K., Yoshikawa, T., Katayama, T., Tohyama, M. (2010). Increased stathmin1 expression in the dentate gyrus of mice causes abnormal axonal arborizations. *PLoS One*, 5(1), e8596

[108] Zhang, L., Hernandez, V., Gerfen, C., Jiang, S., Zavala, L., Barrio, R., and Eiden, L. (2021). Behavioral role of PACAP signaling reflects its selective distribution in glutamatergic and GABAergic neuronal subpopulations. *eLife*, 10, e61718

[109] Zhou, C. J., Shioda, S., Yada, T., Inagaki, N., Pleasure, S. J., and Kikuyama, S. (2002). PACAP and its receptors exert pleiotropic effects in the nervous system by activating multiple signaling pathways. *Current protein and peptide science*, 3(4), 423439